Title	Functionalization of Cellulose-Based Monolithic Materials for Adsorption and Separation of Biologically Relevant Molecules
Author(s)	Wang, Guan
Citation	大阪大学, 2025, 博士論文
Version Type	VoR
URL	https://doi.org/10.18910/103203
rights	
Note	

Doctoral Dissertation

Functionalization of Cellulose-Based Monolithic Materials for Adsorption and Separation of Biologically Relevant Molecules
(生体関連分子の吸着・分離への応用のための
セルロースを基盤としたモノリス材料の機能化)

WANG GUAN

July 2025

Graduate School of Engineering
The University of Osaka

Content

General Introduction

Adsorption and Separation of Biological and Environmental Targets

The selective isolation and analysis of biomolecules are fundamental not only to biological research but also to practical applications in healthcare, industry, and the environment. In nature, the behaviors and functions of living organisms, including animals, plants, and microorganisms, are primarily governed by biomolecules such as nucleic acids, proteins, peptides, lipids, and carbohydrates. With the rapid advancements in materials science, analytical instrumentation, nanotechnology, and biotechnology, the structures, functions, and mechanisms of action of these biomolecules are gradually being elucidated.[1,2] This progress contributes to uncovering the mysteries of life and enables the development of intelligent biomimetic systems.[3] Moreover, as shown in **Fig. 1**, the abnormal expression of specific certain biomolecules in the body serves as an indicator of pathological changes, making their detection highly important for clinical diagnostics.[4] This is particularly important in the context of drug discovery, where biomolecules not only serve as disease markers but also as potential therapeutic agents. Biomolecules with therapeutic potential have become a major source of drug development.[5] Therefore, the adsorption and separation of biologically relevant molecules play a crucial role in numerous fields, including biotechnology, environmental science, and pharmaceutical development. Efficient separation techniques are essential for the purification of biomolecules such as peptides, pharmaceutical intermediates, and environmental contaminants, which are often present in complex mixtures. These processes are essential not only to enhance the accuracy

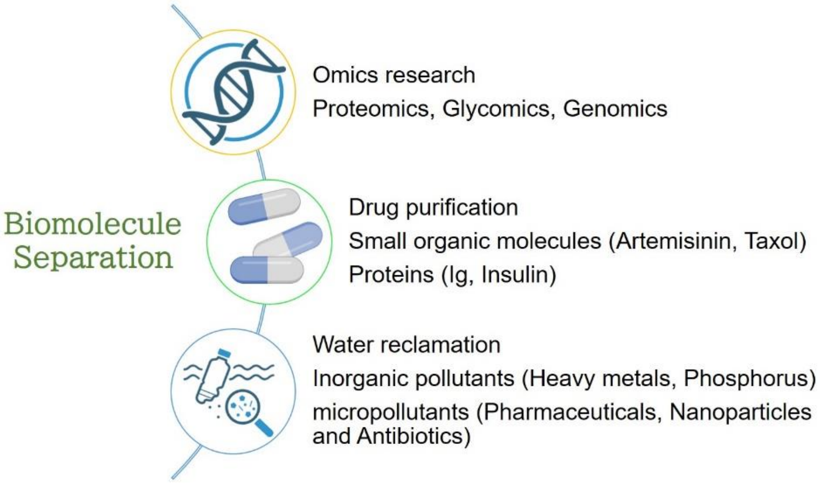

Fig. 1. Application fields of biomolecule separation.[3]

and reliability of analytical methods but also to enable the development of high-purity bioproducts required for therapeutic and diagnostic applications.[6]

Fundamental research in the field of omics is underpinned by a comprehensive workflow that encompasses the separation, characterization, and databasing of biomolecules. This integrated approach is essential for advancing studies in genomics[7,8], proteomics[9,10], and glycomics[11,12]. This high-resolution molecular understanding is not only valuable for basic science but also lays the groundwork for biopharmaceutical production. In parallel, the development of high-purity pharmaceuticals from complex biological matrices generally necessitates multistep purification strategies employing various separation methodologies. This challenge arises from the typically low abundance of target biomolecules amidst a complex mixture of coexisting substances. Notable examples include the isolation of insulin from pancreatic extracts or its biosynthesis using recombinant DNA techniques for diabetes management[13], the purification of artemisinin from Artemisia annua for antimalarial applications[14], and the extraction of paclitaxel from Taxus species for cancer chemotherapy[15]. While therapeutic applications represent one major focus, molecular separation also plays a pivotal role in environmental systems. For example, certain organic fertilizers, livestock manure, and crop residues release high concentrations of nutrients such as nitrogen and phosphorus into aquatic ecosystems.[16] Among these phosphorus readily accumulates and contributes to eutrophication,[17] resulting in algal blooms, oxygen depletion, and severe degradation of water quality.[18] These ecological disruptions highlight the need for effective nutrient removal strategies. In this context, advanced adsorbent materials capable of selectively capturing phosphate and other nutrients are essential for restoring environmental balance and supporting sustainable water resource management. Therefore, to meet diverse separation needs—ranging from the isolation of therapeutic biomolecules to the mitigation of environmental pollutants; novel materials and tailored separation approaches are indispensable.

In addition, selective adsorption materials enable targeted removal or recovery of specific biomolecules, facilitating advances in bioseparation technology and promoting sustainable and cost-effective production processes. In this context, novel adsorbent materials and separation strategies are critical for addressing separation challenges in both biological and chemical industries, enabling the realization of high-purity products, efficient resource utilization, and

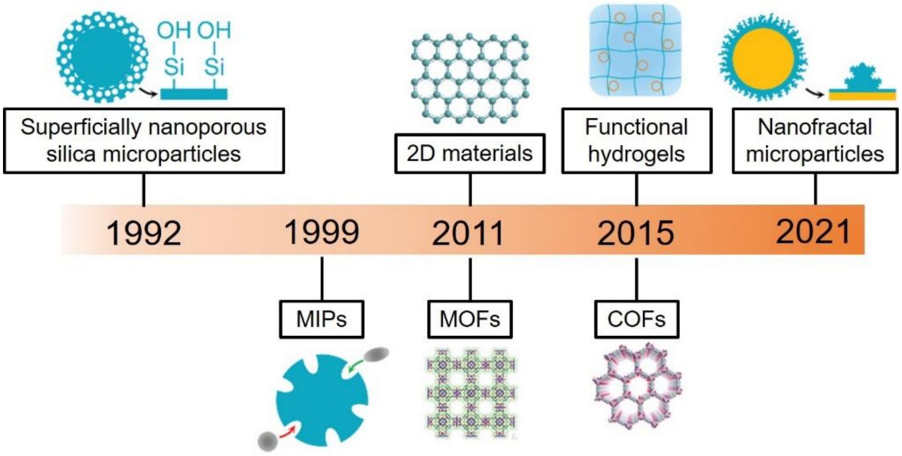

Fig. 2. Timeline of materials for biomolecule separation.[3]

reduced environmental impact.[19] In the past decade, with the rapid advancement of materials science, numerous emerging nanoporous materials have been explored for biomolecular separation applications. These include surface-nanostructured porous silica microparticles[20], molecularly imprinted polymers (MIPs)[21], two-dimensional (2D) materials[22], metal-organic frameworks (MOFs)[23,24], covalent organic frameworks (COFs)[25], functional hydrogels[26], and nanofractal particles[27] (**Fig. 2**). While conventional adsorbent materials offer valuable properties, they also have limitations such as poor performance with complex mixtures, sensitivity to physicochemical conditions, mass transfer resistance, membrane fouling, and unsustainable synthesis. These issues have motivated the development of advanced architectures to improve separation efficiency.[28,29,30] Therefore, advanced adsorbent systems that can reliably capture biomolecules at ultra-low concentrations, sustain high throughput while minimizing membrane fouling, operate under low pressure drops, produce minimal waste, and enable efficient recovery are urgently required. Over the past few years, research has primarily focused on designing innovative adsorbent architectures to overcome the limitations of conventional materials while maximizing overall performance.

Monoliths

Monoliths, characterized by their hierarchical, continuous, and porous three-dimensional (3D) structures, have gained considerable attention due to their simple preparation and uniform architecture. These structures offer several advantages over particulate materials, including ease of separation, reduced pressure drop, enhanced mass transfer, superior mechanical stability, and customizable geometric designs. In 1992, Noel *et al.* first introduced the term monolith to describe a mechanically stable macroporous polymer used in the fabrication of artificial sponges for protein separation.[31] Since then, monoliths have been widely employed to denote single-piece bulk materials featuring three-dimensionally interconnected porous networks or channels. Monoliths that possess continuous macroporous frameworks and mesopore-derived high surface areas are increasingly being explored for a wide range of applications, including protein immobilization, adsorption, ion exchange, catalysis, and sensing.[32] Monoliths offer advantages over particulate materials, such as ease of separation, reduced back pressure, improved mass transfer, superior mechanical stability, and customizable geometric configurations.[33] Their interconnected porous structures facilitate efficient fluid flow with lower energy consumption, while their customizable geometries allow for elevated loading capacity and seamless integration into various systems, particularly in catalytic and separation applications.[34] In addition, their straightforward and scalable manufacturing processes further enhance their practical utility.[35,36] Various strategies for fabricating such monoliths and tailoring their pore architecture have been reported. A significant portion of these studies has focused on inorganic materials such as carbon, silica, and titanium dioxide.[37] In contrast, synthetic polymer-based monolithic materials have recently gained attention due to their favorable biocompatibility, robust chemical resistance, and facile functionalization. Common fabrication approaches for monoliths include free radical polymerization[38], high internal phase emulsion templating[39], and thin-film membrane formation[40]. During the preparation process, the permeability and pore size of the resulting monoliths can be finely tuned by adjusting the pre-polymerization composition and reaction conditions, such as the ratio of porogenic solvents, precursor concentrations, and reaction temperature.[41] Moreover, a wide variety of monomers are available for synthesizing organic monoliths. Different functional monomers can be selected based on the specific requirements of the intended application. Additionally, the surface of the monolithic matrix can be further functionalized to impart desired properties. However, such modifications often involve complex procedures and extended processing times.[42]

Hierarchically porous structures are ubiquitous in nature, ranging from simple unicellular organisms to complex human tissues.[43] These distinctive structural features have garnered growing interest from researchers, leading to the development of a wide variety of

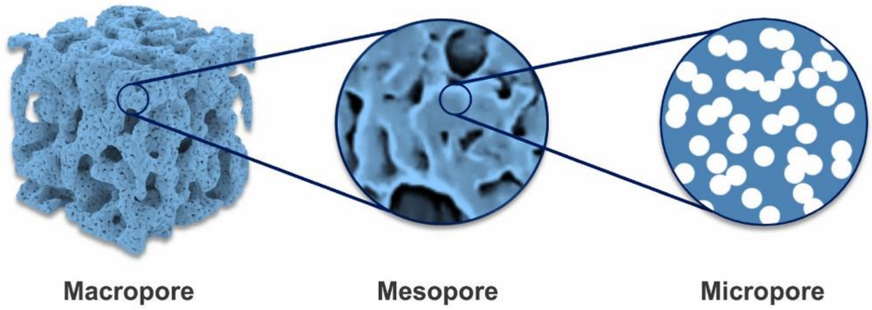

Fig. 3. Schematic structures of hierarchically porous materials.[44]

hierarchically porous materials. Among them, hierarchically porous monoliths have emerged as advanced materials characterized by the integration of two or more levels of porosity, including micropores (<2 nm), mesopores (2 – 50 nm), and macropores (>50 nm) (**Fig. 3**). The presence of micro- and mesopores contributes significantly to the enhancement of surface area and pore volume, offering advantages such as molecular size and shape selectivity as well as increased interfacial contact.[44] In parallel, macropores alleviate diffusion constraints and promote efficient mass transport to active sites. Notably, these monoliths possess a three-dimensionally interconnected pore network, allowing continuous fluid flow through the structure, thereby overcoming limitations associated with particulate or thin-film formats. Owing to their facile fabrication, high mass transfer efficiency, and excellent diffusion properties, hierarchically porous monoliths hold great potential for applications in adsorption, separation, catalysis, and analyte enrichment. For example, Sun *et al.* reported a facile strategy that was used in high-efficiency uranium adsorption of hierarchically porous amidoxime cellulose monolith as an adsorbent.[45] This study showed that the hierarchically porous structure improved properties over the single-mode porous component, with the macroporous framework ensuring mechanical stability and good mass transport properties, while the smaller pores enhanced surface interaction for uranium adsorption.

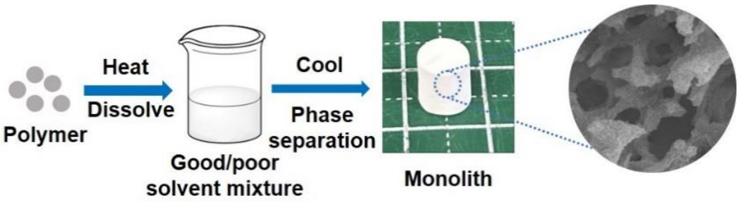

Fig. 4. Monolith preparation process via thermally induced phase separation (TIPS).

In addition to the template-assisted, emulsion, and foaming techniques, phase separation represents one of the most widely employed strategies for fabricating hierarchically porous monoliths.[46] This process involves a transformation from a miscible to an immiscible state. By modulating the system conditions, the solubility of a specific component is reduced, leading to its aggregation and the formation of a new phase. Upon subsequent solvent removal, a porous network can be established. Commonly utilized phase separation methods include thermally induced phase separation (TIPS) and chemically induced phase separation (CIPS). In TIPS, a polymer is initially dissolved in a porogenic solvent at an elevated temperature exceeding the critical solution temperature, resulting in a homogeneous solution. Upon cooling below this critical temperature, phase separation is triggered, yielding a biphasic system.[47] In contrast, CIPS begins with the dissolution of monomers, a cross-linking agent, and an initiator in a porogenic solvent to form a uniform solution.[48] As polymerization progresses, the polymer's molecular weight increases continuously, which reduces its solubility in the solvent-monomer medium, thereby promoting phase separation. This leads to the development of two distinct phases: a polymer-rich (solute) phase and a solvent-rich phase, both of which continue to evolve during the phase separation process.[49] Once gelation occurs, the polymer-rich phase forms the solid framework, while the solvent-occupied regions result in mesopores and macropores. Subsequent solvent exchange at the monolith's surface using a suitable solvent can further induce the formation of surface micropores.[50]

Recently, my research group has developed a straightforward strategy for fabricating hierarchically porous monoliths from polymer solutions via TIPS (**Fig. 4**). Monoliths derived from a range of polymers, including cellulose[42], chitosan, polyacetylene, poly(vinyl alcohol), poly(ethylene-*co*-vinyl alcohol), and poly(γ-glutamic acid), have been fabricated using appropriate binary solvent systems.[51] Some of these monolithic structures have exhibited uniform mesopores alongside submicron- to micron-sized macropores. The fabrication involves a simple procedure: dissolving the polymer in a mixture of good and poor solvents at elevated temperatures, followed by cooling, leading to phase separation and monolith formation. This preparation method is both facile and environmentally benign, yielding monoliths with high porosity and excellent permeability. Through a variety of post-synthetic modifications, these monoliths have been functionalized to exhibit diverse properties, enabling their effective application in areas such as adsorption and catalysis.

The conditions under which phase separation occurs significantly influence the resulting pore architecture of the monolith. For example, the nature of the porogenic solvent determines polymer solubility, which in turn dictates both the onset of phase separation and the coarsening behavior of the polymer-rich domains in the later stages. Typically, a higher proportion of good solvent leads to a more compact pore network with smaller pore sizes, whereas a poor solvent produces a more open structure with larger pores. Therefore, by adjusting the composition of porogenic solvents, various pore morphologies can be tailored.[42] Moreover, in TIPS, the temperature at which phase separation occurs has a substantial influence on the resulting pore architecture of the monolith. When phase separation is induced at relatively higher temperatures, the demixing process between the polymer and the solvent proceeds more gradually, allowing for finer structural control. This typically results in a more uniform and smaller pore network. In contrast, inducing phase separation at lower temperatures accelerates the demixing process, often leading to rapid domain growth and the formation of larger pores with increased structural variability. By carefully selecting the temperature at which the solution is cooled, it is possible to regulate the phase separation kinetics and tailor the hierarchical pore structure. The ability to modulate pore morphology through temperature control is critical for optimizing the performance of monoliths prepared via the TIPS method.[52]

Cellulose

Cellulose is the most abundant natural polymer on Earth and offers an environmentally benign, renewable resource for producing sustainable and biocompatible materials (**Fig. 5**).[53] The molecular formula of cellulose is represented as $(C_6H_{10}O_5)_n$, where n denotes the degree of polymerization, indicating the number of anhydroglucose units (AGUs), which can vary widely from several hundred to tens of thousands.[54] Consequently, cellulose is a high-molecular-weight,

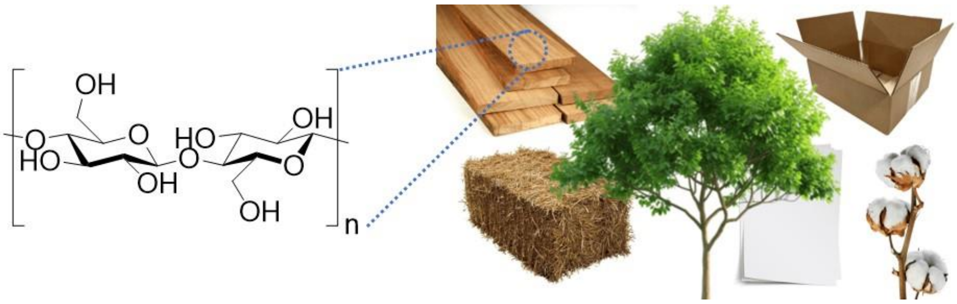

Fig. 5. Basic chemical structure of cellulose, illustrating the cellobiose repeat unit.

linear polysaccharide rich in hydroxyl groups (three per AGU), composed of β-D-glucopyranose residues linked via β-1-4-glycosidic linkages, and adopting the thermodynamically favored $^4C_1$ chair conformation.[55,56] These hydroxyl groups play a crucial role in establishing extensive hydrogen-bonding networks, which in turn influence both the crystallinity and the physicochemical properties of cellulose.[57] The fundamental structural entity of cellulose is the microfibril, which arises during biosynthesis. Cellulose is biosynthetically assembled into fibrillar structures, wherein elongated molecular chains are laterally stabilized through intermolecular hydrogen bonding.[58] These microfibrils consist of highly ordered crystalline domains interspersed with amorphous regions, such as local twists or kinks, aligned along the fibrillar axis.[59,60] Depending on the biological origin and post-processing treatments, cellulose fibers can adopt various polymorphic crystalline arrangements.

The unique molecular architecture of cellulose endows it with distinctive characteristics such as hydrophilicity, chirality, biodegradability, and extensive chemical versatility, primarily attributed to the hydrogen bond-donating capacity of its hydroxyl groups. In light of increasing environmental awareness, cellulose microfibrils have garnered considerable attention as reinforcing agents in polymer-based composites.[61] These microfibrils are recognized for their environmental compatibility and remarkable mechanical performance, with reported Young's moduli ranging from 78 to 114 GPa.[62,63] The propensity of cellulose to form extensive hydrogen-bonded networks contributes to its diverse partially crystalline fiber morphologies. Consequently, cellulose has been widely utilized as a reinforcing phase in composites with controlled structural features, including cellulose monoliths, bacterial cellulose nanofiber networks, and cellulose nanocrystals.

The cellulose monolith (CM) is a promising alternative among cellulose-based materials owing to its facile modifiability, biocompatibility, simple preparation process, and chemical and physical stability. Xin et al reported a TIPS technique as a novel route for preparing CM, using cellulose acetate as the starting material. In contrast to crystalline cellulose, cellulose acetate predominantly leads to the formation of an amorphous structure in resulting CM. Despite this amorphous nature, the monoliths exhibit high mechanical and chemical stability, which can be attributed to the intrinsic properties of the cellulose backbone, particularly the contribution of intermolecular hydrogen bonding to structural reinforcement. Since the fabrication process involves TIPS, the porous structure of CM can be finely adjusted by tuning parameters such as the ratio of good and poor solvents and the phase separation temperature. These variables critically influence the phase separation behavior and allow control over pore size, connectivity, and overall morphology. Solvent systems such as *N,N*-dimethylformamide (DMF) with 1-hexanol and dimethyl sulfoxide (DMSO) with water have been demonstrated to effectively induce phase separation and generating stable, interconnected macroporous structures. The resulting monoliths exhibit continuous macropores with rough, hydrophilic surfaces, which are highly amenable to further chemical modification. In addition, the hydrophilic and nonionic nature of cellulose tends to suppress nonspecific adsorption, which is advantageous for applications such as bioseparation and sensing. These features make CM a versatile and robust platform for various applications requiring porous materials with tunable properties and reliable performance.

Design of functionalization of cellulose monolith in this dissertation

In this thesis, three distinct cellulose-based monolithic materials were prepared for the adsorption and separation of biologically relevant molecules. In chapter 1, a monolithic stationary phase for hydrophilic interaction liquid chromatography (HILIC) was developed using CM as the base material, targeting glycopeptide enrichment. Citric-acid-modified cellulose monolith (CCM) exhibited a distinctive coral-like skeletal structure with continuous pores and a rough surface. The efficacy of CCM as a HILIC medium for the efficient enrichment of glycopeptides was demonstrated, even in the presence of non-glycopeptides and other interfering substances. In chapter 2, a selective recognition strategy was established by combining CM with surface molecular imprinting for the separation of shikimic acid (SA). A co-continuous porous structure was constructed via surface modification of the CM with a molecularly imprinted layer, making it suitable for flow-based separation systems. The boronic acid-modified imprinting layer provided selective adsorption sites and size-specific pores for efficient separation of SA. In chapter 3, a hierarchically porous titanium dioxide–modified cellulose monolith (TiO_2-CM) was developed and evaluated for phosphate adsorption in water treatment. CM was modified with TiO_2 via a sol–gel process using titanium isopropoxide, yielding a rough, interconnected porous structure favorable for adsorption. The TiO_2-CM exhibited high efficiency in the removal of phosphate ions and good reusability under continuous flow conditions.

Outline of this dissertation

In this thesis, cellulose-based monoliths were designed for the adsorption and separation of biologically relevant molecules. By modifying the surface of the CM with citric acid, a molecularly imprinted layer, or TiO_2, these materials demonstrated strong application potential for the enrichment of glycopeptides, the selective recognition of shikimic acid, and the adsorption of phosphate.

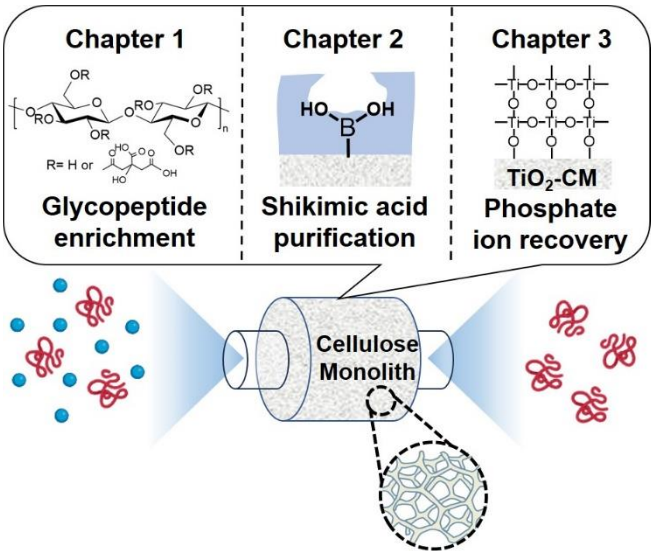

Fig. 6. Schematic illustration of the functional design of the monoliths presented in this dissertation.

Chapter 1

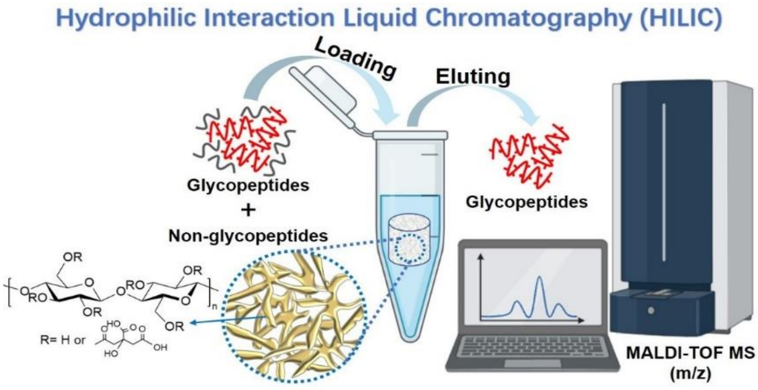

Fig. 7. Schematic illustration of enriching glycopeptides using CCM.

In this chapter, the development of an environmentally friendly CCM is described for the selective enrichment of low-abundance glycopeptides prior to mass spectrometry (MS) analysis, which is essential for the identification of protein glycosylation. The CCM was prepared using a TIPS method, resulting in a coral-like porous structure with a high density of hydrophilic groups. Biomass-derived cellulose and citric acid were used as sustainable starting material. The resulting CCM demonstrated excellent performance as a stationary phase for HILIC (**Fig. 7**). It showed remarkable selectivity in enriching glycopeptides from trypsin-digested immunoglobulin G (IgG), serving as a model protein, even in the presence of a significant amount of non-glycopeptide contaminants from bovine serum albumin (BSA) at a BSA/IgG ratio of 1000:1. Furthermore, the CCM achieved a low detection limit (0.25 fmol μL^{-1}) and exhibited excellent reusability, successfully enriching 35 glycopeptides from IgG. Moreover, analysis of 900 μg of human hepatocellular carcinoma tissue in triplicate led to the identification of 698 unique glycopeptides corresponding to 641 N-glycosylation sites across 393 glycoproteins. These results underscore the strong potential of CCM as a sustainable and effective HILIC stationary phase for glycopeptide enrichment.

Chapter 2

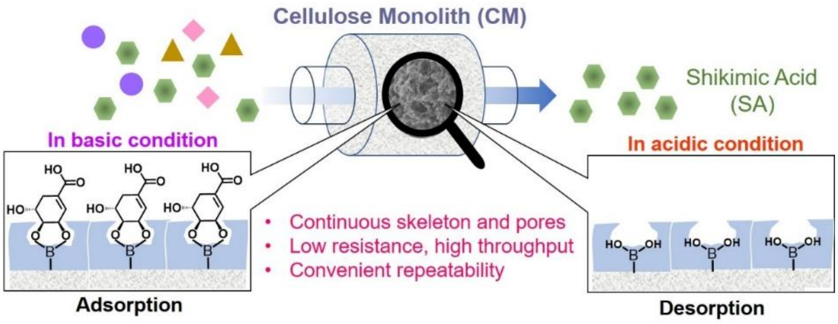

Fig. 8. Schematic illustration of MIPs-CM for the separation of SA.

In this chapter, an efficient recognition method is introduced by combining an environmentally friendly CM with a surface molecular imprinting strategy for the selective recognition and separation of the drug molecule shikimic acid (SA) (**Fig. 8**). A molecularly imprinted cellulose monolith (MIPs-CM) was prepared by forming an imprinted polymer layer functionalized with boronic acid groups on the porous backbone, through the polymerization of vinylphenylboronic acid and a cross-linker in the presence of the SA template molecule. The morphology, elemental composition, and pore structure of MIPs-CM were characterized using Fourier transform infrared spectroscopy (FT-IR), scanning electron microscopy (SEM), X-ray photoelectron spectroscopy (XPS), and nitrogen adsorption–desorption measurements. The resulting MIPs-CM featured a uniform and abundant imprinted layer with a high specific surface area. Adsorption experiments demonstrated that MIPs-CM exhibited fast adsorption kinetics, excellent recognition ability, and a maximum adsorption capacity of 65.4 mg g^{-1} approximately twice that of the non-imprinted monolith (NIPs-CM). The adsorption behavior followed the Langmuir isothermal model, and the adsorption capacity retained 85% of its initial value after five cycles. Experimental results confirmed that MIPs-CM offers high selectivity and strong recoverability for SA separation. These findings confirm that MIPs-CM offers high selectivity and strong reusability for SA separation. This high-performance MIPs-CM, functionalized with boronic acid groups, demonstrates strong potential as a platform for isolating and purifying other *cis*-diol-containing drug molecules from environmental samples.

Chapter 3

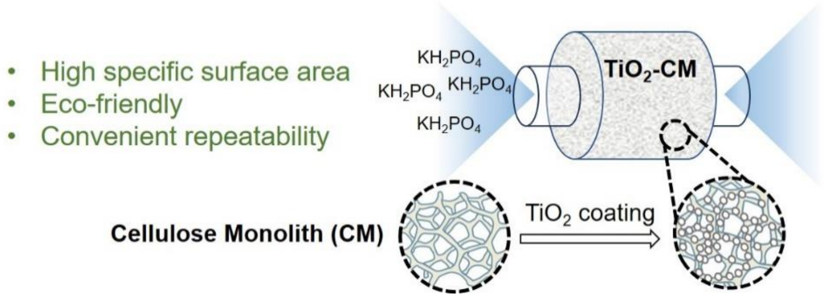

Fig. 9. Schematic illustration of the TiO_2-CM for adsorption of phosphate ions.

In this chapter, the development of an effective adsorbent for phosphate removal is presented, addressing the need to mitigate eutrophication and facilitate the recovery of elemental phosphorus from water sources. Although phosphate adsorption is a key strategy, achieving high adsorption efficiency, reusability, and low secondary pollution using a single material remains challenging. To this end, a hierarchically porous titanium dioxide-modified cellulose monolith (TiO_2-CM) was evaluated for its performance in continuous flow systems (**Fig. 9**). TiO_2 was deposited onto the surface of the CM backbone through a sol–gel reaction using titanium isopropoxide as the precursor. The resulting TiO_2-CM exhibited a rough, interconnected pore network with hierarchical porosity, enabling high surface area and low flow resistance. These features are essential for efficient continuous flow adsorption. The TiO_2-CM demonstrated high phosphate removal efficiency and good reusability, underscoring its promise as a practical adsorbent for water treatment applications.

References

(1) Burns, A.; Olszowy, P.; Ciborowski, P. Biomolecules. In *Proteomic Profiling and Analytical Chemistry*, **2016**, 7–24.

(2) Mendes, B. B.; Conniot, J.; Avital, A.; Yao, D.; Jiang, X.; Zhou, X.; Sharf-Pauker, N.; Xiao, Y.; Adir, O.; Liang, H.; Shi, J.; Schroeder, A.; Conde, J. Nanodelivery of Nucleic Acids. *Nat. Rev. Methods Primers* **2022**, *2* (1), 24.

(3) Song, Y.; Bao, H.; Shen, X.; Li, X.; Liang, X.; Wang, S. Emerging Nanoporous Materials for Biomolecule Separation. *Adv. Funct. Mater.* **2022**, *32* (20), 2113153.

(4) Barnes, D. M.; Gillett, C. E.; Bobrow, L. G.; Hanby, A. M.; Mohammed, S.; Hodgson, S.; Leigh, I. M.; Purkis, T.; MacGeoch, C.; Spurr, N. K.; Bartek, J.; Vojtesek, B.; Picksley, S. M.; Lane, D. P. Abnormal Expression of Wild Type P53 Protein in Normal Cells of a Cancer Family Patient. *Lancet* **1992**, *340* (8814), 259–263.

(5) Zimmermann, B.; Hahnefeld, C.; Herberg, F. W. Applications of Biomolecular Interaction Analysis in Drug Development. *TARGETS* **2002**, *1* (2), 66–73.

(6) Sun, N.; Yu, H.; Wu, H.; Shen, X.; Deng, C. Advanced Nanomaterials as Sample Technique for Bio-Analysis. *Trends Anal. Chem.* **2021**, *135*, 116168.

(7) Bustamante, C. D.; De La Vega, F. M.; Burchard, E. G. Genomics for the World. *Nature* **2011**, *475* (7355), 163–165.

(8) Lander, E. S. The New Genomics: Global Views of Biology. *Science* **1996**, *274* (5287), 536–539.

(9) Tyers, M.; Mann, M. From Genomics to Proteomics. *Nature* **2003**, *422* (6928), 193–197.

(10) Mallick, P.; Kuster, B. Proteomics: A Pragmatic Perspective. *Nat. Biotechnol.* **2010**, *28* (7), 695–709.

(11) Hart, G. W.; Copeland, R. J. Glycomics Hits the Big Time. *Cell* **2010**, *143* (5), 672–676.

(12) Cummings, R. D.; Pierce, J. M. The Challenge and Promise of Glycomics. *Chem. Biol.* **2014**, *21* (1), 1–15.

(13) Johnson, I. S. Human Insulin from Recombinant DNA Technology. *Science* **1983**, *219*

(4585), 632–637.

(14) Tu, Y. Artemisinin—A Gift from Traditional Chinese Medicine to the World (Nobel Lecture). *Angew. Chem. Int. Ed.* **2016**, *55* (35), 10210–10226.

(15) Nicolaou, K. C.; Dai, W.; Guy, R. K. Chemistry and Biology of Taxol. *Angew. Chem. Int. Ed. Engl.* **1994**, *33* (1), 15–44.

(16) Darch, T.; Blackwell, M. S. A.; Hawkins, J. M. B.; Haygarth, P. M.; Chadwick, D. A Meta-Analysis of Organic and Inorganic Phosphorus in Organic Fertilizers, Soils, and Water: Implications for Water Quality. *Crit. Rev. Environ. Sci. Technol.* **2014**, *44* (19), 2172–2202.

(17) Jupp, A. R.; Beijer, S.; Narain, G. C.; Schipper, W.; Slootweg, J. C. Phosphorus Recovery and Recycling – Closing the Loop. *Chem. Soc. Rev.* **2021**, *50* (1), 87–101.

(18) de-Bashan, L. E.; Bashan, Y. Recent Advances in Removing Phosphorus from Wastewater and Its Future Use as Fertilizer (1997–2003). *Water Res.* **2004**, *38* (19), 4222–4246.

(19) Zhou, D.-D.; Zhang, J.-P. On the Role of Flexibility for Adsorptive Separation. *Acc. Chem. Res.* **2022**, *55* (20), 2966–2977.

(20) Jin, B.; He, J. Self-Templated Fabrication of Robust Moth-Eye-Like Nanostructures with Broadband and Quasi-Omnidirectional Antireflection Properties. *ACS Photonics* **2017**, *4* (1), 188–196.

(21) BelBruno, J. J. Molecularly Imprinted Polymers. *Chem. Rev.* **2019**, *119* (1), 94–119.

(22) Dubertret, B.; Heine, T.; Terrones, M. The Rise of Two-Dimensional Materials. *Acc. Chem. Res.* **2015**, *48* (1), 1–2.

(23) Yang, X.; Ji, Y.; Jian, M.; Meng, N.; Zhu, Y.; Tan, C.; Li, H. Fabrication of Metal-organic Frameworks Macro-Structures for Adsorption Applications in Water Treatment: A Review. *Sep. Purif. Technol.* **2025**, *354*, 129376.

(24) Chui, S. S.-Y.; Lo, S. M.-F.; Charmant, J. P. H.; Orpen, A. G.; Williams, I. D. A Chemically Functionalizable Nanoporous Material $[Cu_3(TMA)_2(H_2O)_3]_n$. *Science* **1999**, *283* (5405), 1148–1150.

(25) Yang, C.-X.; Liu, C.; Cao, Y.-M.; Yan, X.-P. Facile Room-Temperature Solution-Phase Synthesis of a Spherical Covalent Organic Framework for High-Resolution

Chromatographic Separation. *Chem. Commun.* **2015**, *51* (61), 12254–12257.

(26) Hua, R.; Li, Z. Sulfhydryl Functionalized Hydrogel with Magnetism: Synthesis, Characterization, and Adsorption Behavior Study for Heavy Metal Removal. *Chem. Eng. J.* **2014**, *249*, 189–200.

(27) Song, Y.; Dong, X.; Shang, D.; Zhang, X.; Li, X.; Liang, X.; Wang, S. Unusual Nanofractal Microparticles for Rapid Protein Capture and Release. *Small* **2021**, *17* (36), 2102802.

(28) Qing, G.; Yan, J.; He, X.; Li, X.; Liang, X. Recent Advances in Hydrophilic Interaction Liquid Interaction Chromatography Materials for Glycopeptide Enrichment and Glycan Separation. *Trends Anal. Chem.* **2020**, *124*, 115570.

(29) Du, M.; Zhang, Y.; Wang, Z.; Lv, M.; Tang, A.; Yu, Y.; Qu, X.; Chen, Z.; Wen, Q.; Li, A. Insight into the Synthesis and Adsorption Mechanism of Adsorbents for Efficient Phosphate Removal: Exploration from Synthesis to Modification. *Chem. Eng. J.* **2022**, *442*, 136147.

(30) Bacelo, H.; Pintor, A. M. A.; Santos, S. C. R.; Boaventura, R. A. R.; Botelho, C. M. S. Performance and Prospects of Different Adsorbents for Phosphorus Uptake and Recovery from Water. *Chem. Eng. J.* **2020**, *381*, 122566.

(31) Noel, R.; Sanderson, A.; Spark, L. A Monolithic Ion-Exchange Material Suitable for Downstream Processing of Bioproducts. *Ion Exch. Adv.* **1992**, 229–236.

(32) Esfandiar Pour, S.; Haghighat Mamaghani, A.; Hashisho, Z. Modeling of Adsorption Process on Monolith Adsorbents: A Mini-Review. *Sep. Purif. Technol.* **2025**, *354*, 128846.

(33) Xie, Z.-T.; Asoh, T.-A.; Uyama, H. Monolithic Cellulose Supported Metal Nanoparticles as Green Flow Reactor with High Catalytic Efficiency. *Carbohydr. Polym.* **2019**, *214*, 195–203.

(34) Yang, Z.; Asoh, T.-A.; Uyama, H. Removal of Cationic or Anionic Dyes from Water Using Ion Exchange Cellulose Monoliths as Adsorbents. *Bull. Chem. Soc. Jpn.* **2019**, *92* (9), 1453–1461.

(35) Svec, F.; Fréchet, J. M. J. New Designs of Macroporous Polymers and Supports: From Separation to Biocatalysis. *Science* **1996**, *273* (5272), 205–211.

(36) Svec, Frantisek.; Frechet, J. M. J. Continuous Rods of Macroporous Polymer as High-

Performance Liquid Chromatography Separation Media. *Anal. Chem.* **1992**, *64* (7), 820–822.

(37) Walsh, Z.; Paull, B.; Macka, M. Inorganic Monoliths in Separation Science: A Review. *Anal. Chim. Acta* **2012**, *750*, 28–47.

(38) Zhang, R.; Qi, L.; Xin, P.; Yang, G.; Chen, Y. Preparation of Macroporous Monolith with Three Dimensional Bicontinuous Skeleton Structure by Atom Transfer Radical Polymerization for HPLC. *Polymer* **2010**, *51* (8), 1703–1708.

(39) Pulko, I.; Krajnc, P. High Internal Phase Emulsion Templating – A Path To Hierarchically Porous Functional Polymers. *Macromol. Rapid Commun.* **2012**, *33* (20), 1731–1746.

(40) Tiraferri, A.; Yip, N. Y.; Phillip, W. A.; Schiffman, J. D.; Elimelech, M. Relating Performance of Thin-Film Composite Forward Osmosis Membranes to Support Layer Formation and Structure. *J. Membr. Sci.* **2011**, *367* (1–2), 340–352.

(41) Parlett, C. M. A.; Wilson, K.; Lee, A. F. Hierarchical Porous Materials: Catalytic Applications. *Chem. Soc. Rev.* **2013**, *42* (9), 3876–3893.

(42) Xin, Y.; Xiong, Q.; Bai, Q.; Miyamoto, M.; Li, C.; Shen, Y.; Uyama, H. A Hierarchically Porous Cellulose Monolith: A Template-Free Fabricated, Morphology-Tunable, and Easily Functionalizable Platform. *Carbohydr. Polym.* **2017**, *157*, 429–437.

(43) Yang, L.; Xiao, H.; Qian, Y.; Zhao, X.; Kong, X.-Y.; Liu, P.; Xin, W.; Fu, L.; Jiang, L.; Wen, L. Bioinspired Hierarchical Porous Membrane for Efficient Uranium Extraction from Seawater. *Nat. Sustain.* **2021**, *5* (1), 71–80.

(44) Schwieger, W.; Machoke, A. G.; Weissenberger, T.; Inayat, A.; Selvam, T.; Klumpp, M.; Inayat, A. Hierarchy Concepts: Classification and Preparation Strategies for Zeolite Containing Materials with Hierarchical Porosity. *Chem. Soc. Rev.* **2016**, *45* (12), 3353–3376.

(45) Sun, P.; Ma, L.; Liao, J.; Wang, J.; Huang, C.; Xu, L.; Fu, M.; Wang, J.; Zhou, Q.; Ma, H. Hierarchical Porous Cellulose Monolith Prepared by Thermally Induced Phase Separation for High-Efficiency Uranium Adsorption. *Sep. Purif. Technol.* **2024**, *337*, 126419.

(46) Wang, F.; Altschuh, P.; Ratke, L.; Zhang, H.; Selzer, M.; Nestler, B. Progress Report on Phase Separation in Polymer Solutions. *Adv. Mater.* **2019**, *31* (26), 1806733.

(47) Ma, W.; Zhou, Z.; Ismail, N.; Tocci, E.; Figoli, A.; Khayet, M.; Matsuura, T.; Cui, Z.; Tavajohi, N. Membrane Formation by Thermally Induced Phase Separation: Materials, Involved Parameters, Modeling, Current Efforts and Future Directions. *J. Membr. Sci.* **2023**, *669*, 121303.

(48) Kiefer, J.; Hilborn, J. G.; Hedrick, J. L. Chemically Induced Phase Separation: A New Technique for the Synthesis of Macroporous Epoxy Networks. *Polymer* **1996**, *37* (25), 5715–5725.

(49) Kiefer, J.; Hedrick, J. L.; Hilborn, J. G. Macroporous Thermosets by Chemically Induced Phase Separation. In *Macromolecular Architectures* **1999**, 147, 161–247.

(50) Guillen, G. R.; Pan, Y.; Li, M.; Hoek, E. M. V. Preparation and Characterization of Membranes Formed by Nonsolvent Induced Phase Separation: A Review. *Ind. Eng. Chem. Res.* **2011**, *50* (7), 3798–3817.

(51) Wang, Y.; Zhang, L.; Asoh, T.-A.; Uyama, H. Facile Preparation of Hierarchically Porous Monolith with Optical Activity Based on Helical Substituted Polyacetylene via One-Step Synthesis for Enantioselective Crystallization. *ACS Appl. Mater. Interfaces* **2021**, *13* (40), 48020–48029.

(52) Dobry, A.; Boyer-Kawenoki, F. Phase Separation in Polymer Solution. *J. Polym. Sci.* **1947**, *2* (1), 90–100.

(53) Béguin, P.; Aubert, J.-P. The Biological Degradation of Cellulose. *FEMS Microbiol. Rev.* **1994**, *13* (1), 25–58.

(54) Blanco, A.; Monte, M. C.; Campano, C.; Balea, A.; Merayo, N.; Negro, C. Nanocellulose for Industrial Use. *Handbook of Nanomaterials for Industrial Applications* **2018**, 74–126.

(55) Nishino, T.; Matsuda, I.; Hirao, K. All-Cellulose Composite. *Macromolecules* **2004**, *37* (20), 7683–7687.

(56) McFarlane, H. E.; Döring, A.; Persson, S. The Cell Biology of Cellulose Synthesis. *Annu. Rev. Plant Biol.* **2014**, *65* (1), 69–94.

(57) John, M.; Thomas, S. Biofibres and Biocomposites. *Carbohydr. Polym.* **2008**, *71* (3), 343–364.

(58) Andresen, M.; Johansson, L.-S.; Tanem, B. S.; Stenius, P. Properties and Characterization

of Hydrophobized Microfibrillated Cellulose. *Cellulose* **2006**, *13* (6), 665–677.

(59) Montanari, S.; Roumani, M.; Heux, L.; Vignon, M. R. Topochemistry of Carboxylated Cellulose Nanocrystals Resulting from TEMPO-Mediated Oxidation. *Macromolecules* **2005**, *38* (5), 1665–1671.

(60) Azizi Samir, M. A. S.; Alloin, F.; Dufresne, A. Review of Recent Research into Cellulosic Whiskers, Their Properties and Their Application in Nanocomposite Field. *Biomacromolecules* **2005**, *6* (2), 612–626.

(61) Lee, J.; Deng, Y. The Morphology and Mechanical Properties of Layer Structured Cellulose Microfibril Foams from Ice-Templating Methods. *Soft Matter* **2011**, *7* (13), 6034.

(62) Hsieh, Y.-C.; Yano, H.; Nogi, M.; Eichhorn, S. J. An Estimation of the Young's Modulus of Bacterial Cellulose Filaments. *Cellulose* **2008**, *15* (4), 507–513.

(63) Li, T.; Chen, C.; Brozena, A. H.; Zhu, J. Y.; Xu, L.; Driemeier, C.; Dai, J.; Rojas, O. J.; Isogai, A.; Wågberg, L.; Hu, L. Developing Fibrillated Cellulose as a Sustainable Technological Material. *Nature* **2021**, *590* (7844), 47–56.

Chapter 1. Development of Citric-Acid-Modified Cellulose Monolith for Enriching Glycopeptides

1.1. Introduction

Glycoproteins, prevalent in biological systems, perform myriad functions[1] such as roles in immunity[2,3] and disease detection.[4–6] Glycosylation modification of proteins is considered one of the most common post-translational modifications of proteins. It refers to the glycosylation of proteins by covalent linkage of polysaccharides to amides or alcohols in proteins.[7] Glycans exhibit diverse structures, correlating to their varied activities. B.A.H. Smith delineated three principal functions of glycosylation: imparting unique physical characteristics, influencing properties of attached entities like protein stability or receptor dimerization, and acting as lectin ligands for carbohydrate receptor interactions.[8] A critical objective of contemporary research at the intersection of glycobiology and immunology is identifying glycan composition changes indicative of autoimmune diseases.

Mass spectrometry (MS) is the most widely adopted technique for glycopeptide analysis due to its superior sensitivity and qualitative capabilities.[9–12] However, directly analyzing glycosylations in biological samples via MS is challenging owing to the low abundance and ionization efficiency of glycopeptides and glycoproteins.[13] The "bottom-up" proteomics analysis strategy offers an effective indirect protein analysis approach, employing chemicals or enzymes to decompose intact proteins and analyzing the resultant peptides to characterize proteins.[14] Given their glycan-induced increased hydrophilicity, glycopeptides exhibit higher hydrophilicity than non-glycopeptides.[15] Exploiting this hydrophilicity[16,17] difference, hydrophilic interaction liquid chromatography (HILIC) has been utilized to enrich various glycopeptides, thereby preserving complete glycan information.[18,19] Several materials have been examined using HILIC, including graphene oxide (GO)[20–22], magnetic nanoparticles[23–25], titanium dioxide[19,26], metal-organic frameworks (MOFs)[27–29], and covalent organic frameworks (COF[30–32]). Nonetheless, traditional HILIC particle-based stationary phases face limitations such as tiny nanopores causing substantial mass transfer resistance, which leads to diminished performance and limited enrichment efficiency.[33] Moreover, these materials often entail high costs and complex, environmentally detrimental production methods.[17,33]

Monoliths, characterized by their hierarchical, continuous, porous three-dimensional (3D) structure, have garnered significant interest due to their straightforward preparation and consistent architecture.[34] Monoliths offer advantages over particulate materials, such as ease of separation, lower pressure drop, improved mass transfer, superior mechanical stability, and customizable geometric configurations. Their interconnected porous structures enable efficient fluid flow with reduced energy costs. Additionally, customizable shapes make them versatile for integration into various systems, particularly in catalytic and separation processes. These structures present numerous advantages over traditional chromatography stationary phases, including reduced back pressure, swift mass transfer kinetics, elevated loading capacity, and uncomplicated manufacturing processes.[35–37] Cellulose, the most abundant natural polymer on Earth, is ecologically benign and provides an inexhaustible supply of raw materials for creating environmentally sustainable and biocompatible products.[38] Its notable hydrophilicity, robust mechanical strength, and the ease of modifying its hydroxyl-rich surface make cellulose monoliths ideal candidates for HILIC substrates.[39,40]

Cellulose monolith (CM) is produced through thermally induced phase separation (TIPS), starting from cellulose acetate (CA) and followed by deacetylation.[34] This process endows CM with physicochemical stability due to its rigid polymer framework and high resilience to common solvents and thermal conditions. Additionally, the morphology of the skeleton, which can be tailored by altering polymer concentration, phase separation temperature, and solvent ratio, minimizes steric hindrances between the material and peptides during enrichment, thereby enhancing permeability and mass transfer.[41] Advances in HILIC materials aim to increase the density of hydrophilic groups on immobilized materials, thus improving glycopeptide detection sensitivity and loading capacity.[17]

Citric acid, derived from citrus fruits, is an eco-friendly, non-toxic compound widely used as a biodegradable cleaner, food preservative, chelating agent, flavor enhancer, and water softener.[42] Also, it can be obtained by fermentation of plant-derived renewable sources as substrates, which is industrially applied for sustainable production.[43] Its utilization for surface modification increases hydrophilicity, with the polar acidic groups making it an excellent candidate for HILIC materials by promoting glycopeptide capture via hydrogen bonding with glycan moieties.[44]

This study introduces an eco-friendly citric-acid-modified cellulose monolith (CCM) prepared as a HILIC material using the TIPS method (**Fig. 1-1**).[45] The author investigated the impact of morphology on enrichment capacity by preparing CCM with varying pore sizes and evaluated its efficacy in enriching glycopeptides from trypsin-digested immunoglobulin G (IgG) using MS. The study encompassed assessing the optimal loading buffer ratio, determining CCM selectivity with the addition of interfering protein bovine serum albumin (BSA), exploring the detection limit by decreasing IgG peptide amounts, and assessing CCM reusability through repeated adsorption-desorption cycles. Significantly, this method is both simple and environmentally benign, with the produced CCM demonstrating satisfactory performance in protein glycosylation analysis.

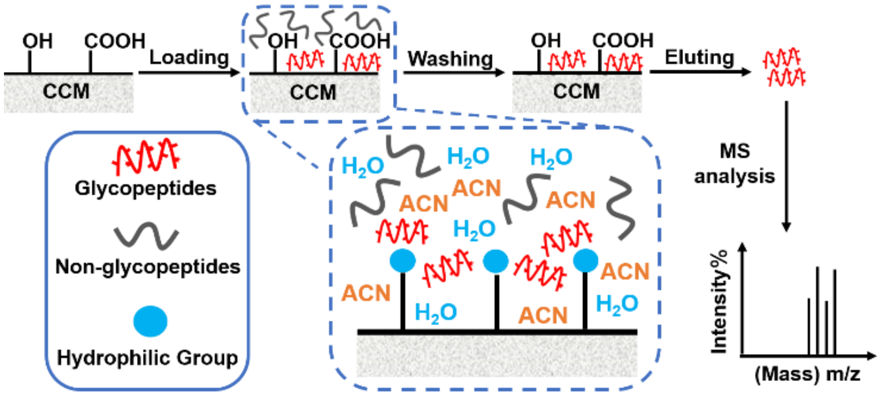

Fig. 1-1. Schematic illustration of processes involved in the enrichment of glycopeptides from the tryptic digest proteins via HILIC.

1.2. Experimental Section

1.2.1. Materials and measurement

L30 CA was acquired from Daicel Corporation (Tokyo, Japan). *N,N*-Dimethylformamide (DMF), methanol (MeOH), and anhydrous citric acid were procured from Nacalai Tesque, Inc. (Japan). 1-Hexanol was obtained from Sigma-Aldrich, while sodium hydroxide (NaOH), hydrochloric acid (HCl), and acetonitrile (ACN) were sourced from FUJIFILM Wako Pure Chemical Industries. Dithiothreitol (DTT), iodoacetamide (IAA), β-casein, immunoglobulin G (IgG), BSA, plasma from human, trypsin, and trifluoroacetic acid (TFA) were purchased from Sigma Co., Ltd. Deionized water for this study was produced by a Milli-Q system (Millipore Corp., Milford, MA, USA). The human hepatocellular carcinoma tissue was obtained from the First Affiliated Hospital of the Fourth Military Medical University (Xi'an, China). The utilization of human hepatocellular carcinoma tissue obeyed the guideline of Ethics Committee of the Hospital.

Fourier-transform infrared (FT-IR) spectroscopy was performed using a Nicolet iS5 spectrometer from Thermo Scientific (USA), equipped with an iD5 ATR attachment. SEM images were captured with a Hitachi S-3000N instrument (Japan) at 15 kV after sample preparation, including sectioning into small pieces and coating with gold via an ion-sputtering apparatus (E-1010 Ion Sputter, Hitachi Ltd., Japan). Water contact angle measurements were performed with a Drop Master DM300 (Kyowa Interface Science, Japan) using 1.0 μL water droplets. The permeability of the monolithic column was calculated applying Darcy's law through the equation $B_0 = F\eta L/(\pi r^2 \Delta P)$, where F ($\mathrm{m^3\ s^{-1}}$) represents the flow rate of the mobile phase, η (Pa s) the viscosity of the mobile phase (2.98×10^{-3} Pa s for water), L (m) and r (m) the effective length and inner diameter of the monolith, respectively, and ΔP (Pa) the pressure drop across the monolith. L and r of the CCM80 CCM100, and CCM120 were $9.68 \pm 0.2\times 10^{-3}$ m and $2.36 \pm 0.01\times 10^{-3}$ m, $8.35 \pm 0.2\times 10^{-3}$ m and $2.31 \pm 0.01\times 10^{-3}$ m, and $8.15 \pm 0.2\times 10^{-3}$ m and $2.14\pm0.01\times 10^{-3}$m, respectively. To determine the permeability of the obtained monoliths, they were tightly fitted with heat shrink tubing and joined with a digital quantitative tubing pump (As One, DSP-100SA) to control the flow rate of the mobile phase ranging from 0.2 to 2.0 mL $\mathrm{min^{-1}}$ and a digital pressure gauge (Krone, KDM30) to determine pressure drop. Then, the permeability of could be calculated by Darcy’s law. Conductivity and pH measurements of the monolith were conducted with a standard pH electrode 9615-10D connected to a Horiba LAQUA F-74 analyzer. MALDI-TOF MS analyses were performed in a positive-ion mode on an Autoflex III (Bruker, Germany), mixing 0.5 μL of the sample solution with 0.5 μL of a DHB solution (25 mg mL^{-1}, in ACN/H_2O/H_3PO_4, 70/29/1, v/v/v) sequentially placed on the MALDI plate. The LC-MS/MS experiments were carried out on Thermo Orbitrap Explores 480 (Thermo Fisher Scientific, San Jose, USA) with a Vanquish NEO HPLC system (Thermo Fisher Scientific). Temperature and rotational speed for the batch system were regulated using a bioshaker.

1.2.2. Fabrication of CM

The fabrication of the cellulose acetate monolith (CAM) was accomplished via the TIPS method.[45]. Initially, CA powder quantities of 2.0 g, 2.5 g, and 3.0 g were individually dissolved in 10 mL of DMF at 90 °C, with continuous stirring until each mixture became clear and transparent. Following this, 15 mL of 1-hexanol was incrementally added to each dispersion in three separate 5 mL additions while stirring continued. The resulting CA dispersion was then transferred to a glass tube and left undisturbed at 25 °C overnight to allow for phase separation. The CAM was formed after several cycles of solvent exchange with methanol at 25 °C, followed by drying. For the conversion to CM, the CAM underwent deacetylation by immersion in a 0.2 molL^{-1} sodium hydroxide/methanol solution. To eliminate any residual unreacted NaOH on the surface and within the monolith, the nascent CM was extensively rinsed with deionized water until a neutral pH of approximately 7 was reached. The final stage involved drying the sample under vacuum to remove any remaining water, thereby obtaining the CM.

1.2.3. Preparation of CCM

For CCM preparation, the CM was submerged in a 192 mg mL^{-1} citric acid/methanol solution and agitated in a bioshaker for 3 h at room temperature to ensure thorough contact with the citric acid solution with the monolith. After the methanol was evaporated through drying, the samples were subjected to a 3-h heat treatment at 120 °C to facilitate the esterification reaction between the hydroxyl groups of cellulose and the carboxyl groups of citric acid. To remove any unreacted citric acid from the surface and interior of the monolith, the newly prepared CCM underwent multiple washes with deionized water and methanol.

Finally, water in the sample was removed by drying under a vacuum to obtain the CCM. Three different pore sizes of the monolith are mentioned in **Table 1-1**.

Table 1-1. Monoliths with different cellulose acetate concentrations.

Cellulose acetate concentration (mg mL^{-1})	80	100	120
Cellulose Acetate Monolith	CAM80	CAM100	CAM120
Cellulose Monolith	CM80	CM100	CM120
Citric-Acid-modified Cellulose Monolith	CCM80	CCM100	CCM120

1.2.4. Glycopeptide enrichment

The process of glycopeptide enrichment using hydrophilic interaction chromatography (HILIC) typically encompasses three phases: loading, washing, and elution. In this procedure, 1 mg of the CCM was initially rinsed with 200 μL of loading buffer (acetonitrile/water/trifluoroacetic acid, ACN/H_2O/TFA) three times. Following this, 200 μL of the same loading buffer, containing 1 μg of IgG tryptic digest (3.3 pmol mL^{-1} in deionized water), was introduced to the CCM and incubated on an oscillator at 25 °C for 30 min. (The step of denaturation and enzymatic digestion of protein solutions is described in supplementary information.) The mixture was then centrifuged at 10000 RPM for 2 min to remove the supernatant, and the CCM was further washed with 200 μL of the loading buffer three times. For elution, 10 μL of an eluting solution (ACN/H_2O/TFA = 30/69/1, v/v/v) was employed to release the bound glycopeptides at room temperature. The eluted solution was subsequently analyzed using a matrix-assisted laser desorption/ionization time-of-flight (MALDI-TOF) system.

The study also evaluated the reusability of the CCM through five consecutive enrichment cycles. Before each re-enrichment, the CCM underwent three washes with the eluting solution (ACN/H_2O/TFA = 30/69/1, v/v/v) to detach any peptides lingering on the surface or within the CCM.

To enrich N-glycopeptides from human hepatocellular carcinoma tissue, the lyophilized tryptic digest (900 μg) was dissolved in 500 μL of a loading solution composed of ACN/H_2O/TFA (79/20/1, v/v/v). Subsequently, 10 mg of CCM was introduced into the solution. The resulting mixture was incubated on a platform shaker at room temperature for 30 minutes. Following incubation, the CCM was separated from the mixture by centrifugation at 1500*g* for

2 min and washed with 500 μL of washing solution (ACN/H_2O/TFA = 79/20/1, v/v/v). The glycopeptides were then eluted with 3 × 250 μL elution solution (ACN/H_2O/TFA = 30/69/1, v/v/v) over a 10 min period at room temperature. The eluents were pooled, lyophilized, and subjected to deglycosylation prior to LC-MS/MS analysis. Detailed protocols for LC-MS measurements are provided in the Supporting Information.

1.2.5. Mass spectrometry analysis

MALDI-TOF MS experiments were carried out in positive ion mode on an Autoflex III (Bruker, Germany). The sample solution (0.5 μL) and 0.5 μL DHB solution (25 mg mL^{-1}, ACN/H_2O/H_3PO_4, 70/29/1, v/v/v) were deposited sequentially on the MALDI plate for MS analysis.

The complete MS scan range was from m/z 400 to 2,000 and was obtained by Orbitrap at 70,000 resolutions in the mass spectrometer. The 20 strongest multi-charged ions were fragmented by higher energy collision dissociation. The normalized HCD collision energy was 27%, and the spray voltage was 2 kV. The temperature of the heated capillary was set at 250 °C. All MS and MS/MS spectra were collected in data-dependent acquisition mode using Xcalibur software.

1.2.6. Enzymatic Digestion of Protein

BSA (2 mg) or IgG or human serum samples in 1 mL denaturation buffer (0.1 mol L^{-1} NH_4HCO_3 was mixed with 8.0 mol L^{-1} urea), adding 20 μL of 20 mmol L−1 DTT solution. The mixture was incubated at 60 °C for 1 h. Then, 7.4 mg IAA was added to the mixture and incubated for 30 min at room temperature in the dark. The mixture was then diluted to one-eighth of the concentration of the stock solution using 0.1 mol L^{-1} NH_4HCO_3, followed by 80 μg trypsin, and incubated for 16 h at 37 °C. Then, TFA solution (10%, wt%) was used to adjust the pH to 2~3. Then, the other TFA solution (0.1%, wt%) was used as the eluent to extract the digest with a C18 solid-phase extraction column to obtain the BSA/IgG trypsin digest. Finally, the BSA/IgG trypsin digest may be separated, lyophilized, and stored at -20 °C for later use.

1.2.7. Loading Capacity

2 mg CCM80, CCM100, or CCM120 was mixed with 10 mL Pullulan solution within the concentration range of 0.05−1.5 mg mL^{-1}, respectively. After vibrating for 0.5 h, then subjected to UV-Vis analysis. The absorbance at the wavelength of 490 nm was monitored and selected

as the data source for calculating the remained pullulan in the supernatant according to the calibration curve.

1.2.8. Enzymatic Digestion of real samples

The human hepatocellular carcinoma tissue samples were cut into soybean-sized pellets and added to the lysis tube with 3 clean zirconium beads and 1 mL of lysis solution (4% SDS, 100 mM Tris-HCl (pH 8.5), 1 mM PMSF, 1% proteinase inhibitor, and 1% phosphatase inhibitor mixture) in the tissue disruptor to be lysed 3 times, and after completion, the samples were transferred to a 50 mL centrifuge tube with 5 mL of After completion, the samples were transferred to a 50 mL centrifuge tube with 5 mL of lysis solution and continued to be lysed in the cell disruptor. After the samples were fully lysed, the proteins were precipitated overnight at -20°C using a pre-cooled 3-fold volume of acetone. After precipitation, the proteins were washed three times with pre-cooled anhydrous ethanol and centrifuged to remove the anhydrous ethanol, and then dried to evaporate the residual ethanol. The protein concentration was measured using a BCA kit and stored at -60°C for enzymatic digestion.

1.2.9. Clinical Sample Collection

The study protocol was obeyed the guideline of Ethics Committee of the First Affiliated Hospital of the Fourth Military Medical University, Xi'an, China. The study design and conduct complied with all relevant regulations regarding the use of human study participants and was conducted in accordance with the criteria set by the Declaration of Helsinki.

1.2.10. LC-MS/MS experiments conditions

The tryptic digestion of the extracted proteins from hepatocellular carcinoma tissue of human was prepared by referring to the previously reported method. The LC-MS/MS experiments were carried out on Thermo Orbitrap Explores 480 (Thermo Fisher Scientific, San Jose, USA) with a Vanquish NEO HPLC system (Thermo Fisher Scientific). Analytical Column is ACQUITY UPLC® Peptide BEH C18 columns (1.0 mm i.d. × 15 cm, PN: 186005594) that was procured from Waters corporation. The H2O containing 0.1% FA was used as mobile phase A, and the mixture of ACN/DMSO/H2O (v/v/v, 80/3/17) was used as mobile phase B. The gradient used in analysis of the digest of hepatocellular carcinoma tissue of human (10 μL) was 3-4% B in 1 min, 4-32% B in 30 min. The pos ion spray voltage was set at 3.5 kV, the temperature of the ion transfer tube was 320℃, and the collision energy was 28%. The full MS scan ranging from m/z 350 to m/z 1300 was selected in the mass spectrometer. The 28 most intense ions were selected for fragmentation via high energy collision dissociation (HCD). All MS and MS/MS spectra were acquired in the data-dependent MS/MS acquisition mode. System control and data collection were done by Thermo Scientific SII for Xcalibur 1.7.0.468.

The MaxQuant software was used to process mass spectrometry data of peptides and deglycosylated peptides. Initially, the raw data were searched by the MaxQuant v2.4.2.0 against Uniport human reference database containing 20,422 canonical entries (downloaded 03/2023). Trypsin was selected with a maximum of two missed cleavage sites. In terms of protein modifications, carbamidomethylation of cysteine was set as a fixed modification, while oxidation of methionine and acetylation of the protein N-terminus were considered as variable modifications. Apart from the aforementioned parameters, default settings in MaxQuant were used. The false discovery rate (FDR) was set to 1% at the site, peptide-spectrum match (PSM) and protein level.

1.3. Results and discussion

1.3.1. Preparation of the citric-acid-modified cellulose monolith (CCM)

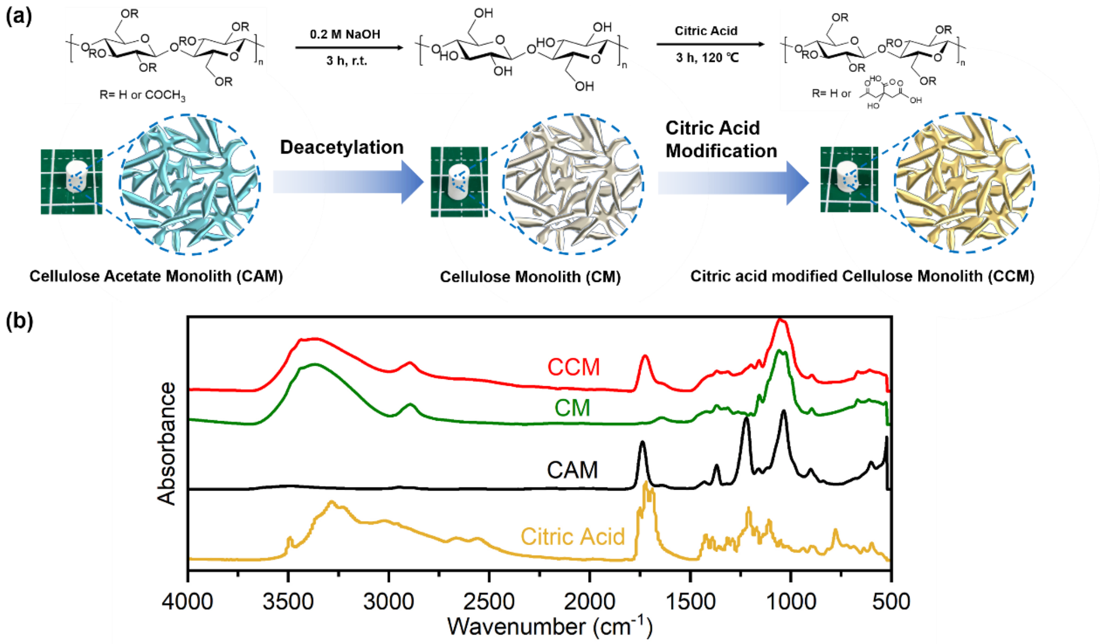

Fig. 1-2. (a) Scheme of the preparation process of citric-acid-modified cellulose monolith (CCM). (b) FT-IR spectra of the citric acid, cellulose acetate monolith (CAM), cellulose monolith (CM), and CCM.

The CAM was fabricated from cellulose acetate using the TIPS method (**Fig. 1-2a**).[45] A simple deacetylation procedure was used to prepare the CM. An efficient method was used to modify CM via an esterification reaction. Compared to the CAM, there was no apparent difference in the appearance of the CCM (**Fig. 1-2a**), supporting that the monolith has sufficient strength to maintain its shape after chemical modification.

FT-IR spectroscopy was employed to verify the successful synthesis of the CCM, as shown in **Fig. 1-2b**. The FT-IR spectra facilitated the identification of significant changes associated with the transformation of CA to cellulose and the subsequent citric acid modification of the CM. Notably, the ester group's C=O stretching vibration peak at 1742 cm^{-1}, characteristic of CAM, was absent in the CM spectra. Instead, a broad peak around 3300 cm^{-1}, indicative of the OH stretching vibration of cellulose, emerged, signifying the effective hydrolysis of CAM. Upon modification with citric acid, the re-appearance of the C=O peak, attributed to the ester group formed during the esterification reaction between cellulose and citric acid, confirmed the successful preparation of CCM.

The hydrophilicity of both CM and CCM was assessed through water contact angle measurements (**Fig. 1-3**). The contact angle was measured on smooth surfaces prepared by compressing powdered cellulose and citric acid-modified cellulose to minimize the influence of surface roughness and porosity. The CM exhibited a water contact angle of 48°, reflective of its inherent hydrophilicity attributed to the hydroxyl groups present. For the CCM, the contact angle was significantly reduced to 25°, evidencing enhanced hydrophilicity. This increase in hydrophilicity is attributed to introducing hydrophilic carboxyl groups into the CM. Consequently, the CCM demonstrated superior hydrophilicity, highlighting its potential for efficient glycopeptide enrichment.

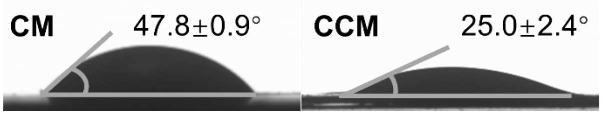

Fig. 1-3. Water contact angle of CM and CCM.

1.3.2. Physical properties of the CCM

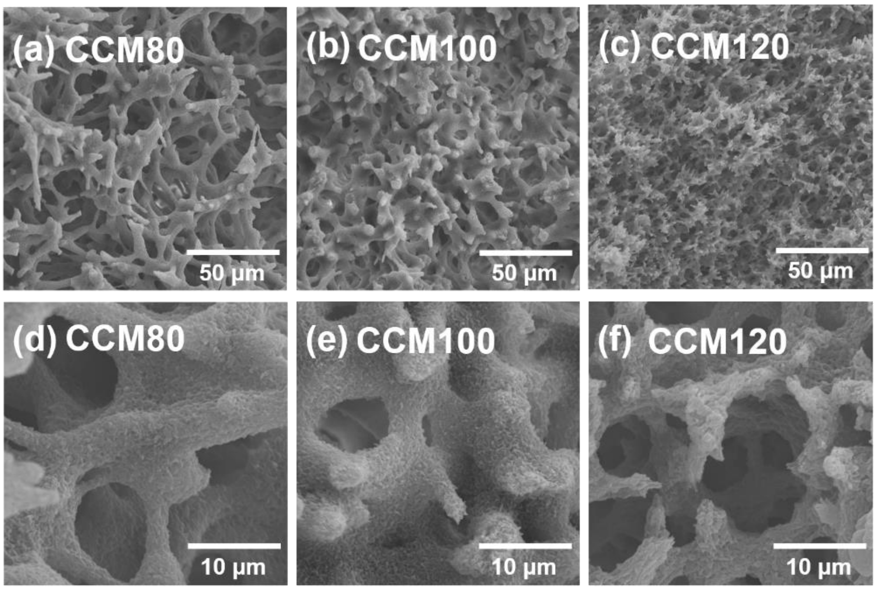

Fig. 1-4. SEM images of citric-acid-modified cellulose monolith (CCM) prepared with different concentrations of cellulose acetate (a and d) CCM80; (b and e) CCM100; and (c and f) CCM120.

The pore size of the CCM was tailored by adjusting the CA concentration. The SEM images demonstrated the impact of different CA concentrations (80, 100, and 120 mg mL^{-1}) on the CCM's structure, as depicted in **Fig. 1-4** and **Fig. 1-5**. The internal structure of the CCM, featuring a continuous porous configuration, mirrored that of the unmodified CM (**Fig. 1-5**), indicating that the citric acid chemical modification did not significantly alter the monolith's morphology. Furthermore, the CM displayed a coral-like 3D continuous porous structure, with the surface presenting villous features reminiscent of a coral's surface. These structures (**Fig. 1-5g-i**) are advantageous for reducing steric hindrance between peptides and the material during enrichment processes and offering additional adsorption sites. Post citric acid modification, the CCM preserved its coral-like skeletal framework and acquired a rough surface akin to the CM (**Fig. 1-4**).

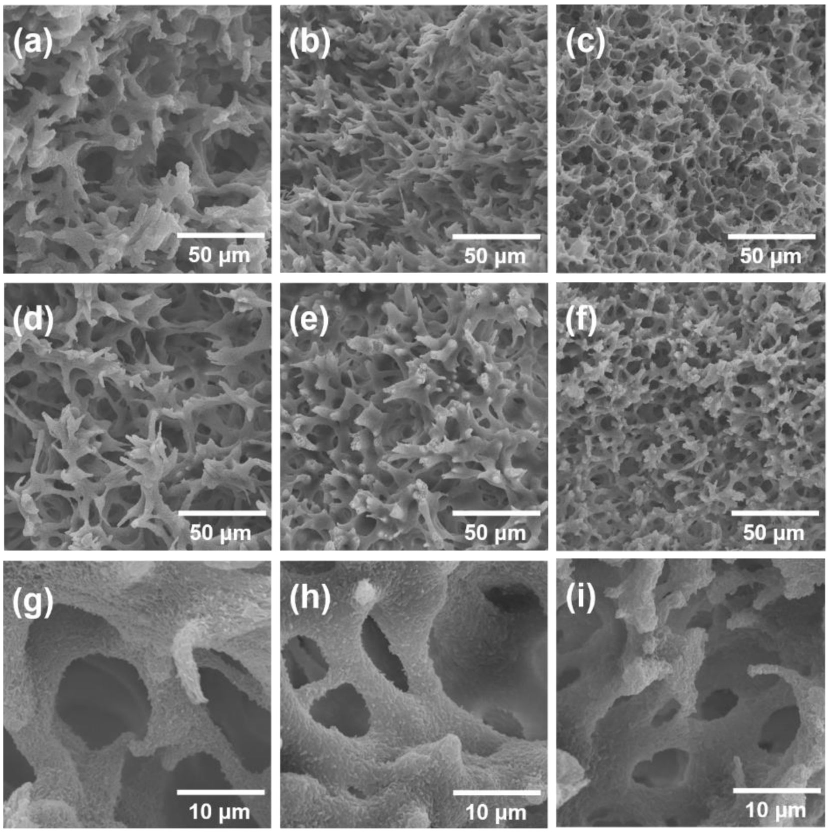

Fig. 1-5. SEM images of CCM prepared with different concentrations of cellulose acetate (a) CAM80; (b) CAM100; (c) CAM120; (d and g) CM80; (e and h) CM100; (f and i) CM120.

Nitrogen adsorption/desorption analysis of CCM80, CCM100, and CCM120 yielded type IV isotherms with type-H1 hysteresis loops, indicative of mesoporous materials, within the relative pressure (P/P_0) ranges of 0.05–1.0 (**Fig. 1-6**). The specific surface areas of CCM80, CCM100, and CCM120 were determined to be 2.91, 5.41, and 13.15 m^2 g^{-1}, respectively, utilizing the multi-point Brunauer-Emmett-Teller (BET) equation. Pore size distribution analysis conducted through the nonlocal density functional theory (NLDFT) method revealed uniformly sized pores with diameters around 10 nm across all samples. This unique surface morphology, resembling rough, coral-like structures, facilitates the free passage of solutions through the porous material surfaces.[46] The distinctive morphology is crucial for the enrichment of glycopeptides; considering the large molecular mass of intact glycopeptides often results in significant steric hindrance, which can hinder efficient enrichment by HILIC materials.[16,46]

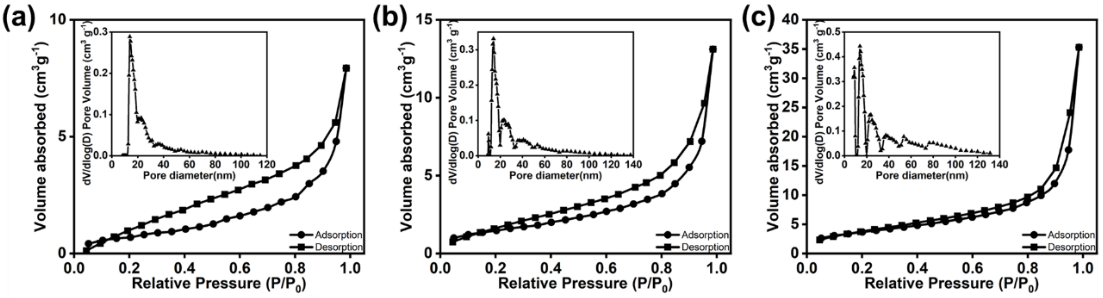

Fig. 1-6. Nitrogen adsorption/desorption isotherms of (a) CCM80, (b) CCM100, and (c) CCM120. Inset: pore size distribution plots of CCM80, CCM100, and CCM120.

The permeability coefficient B_0 of monoliths with different pore sizes was measured to evaluate the permeabilities of the various samples (**Fig. 1-7**). A monolith sample was secured within a heat-shrinkable tube, and water was propelled continuously through the sample at a defined flow rate using a peristaltic pump. CCM80, characterized by its coral-like 3D continuous open pores, showcased remarkable permeability (6.74 × 10^{-12} m^2), thus enhancing mass transfer capabilities. Also, batch mode in glycopeptide enrichment offers benefits over column formats, including enhanced preservation of fragile glycopeptides, easier optimization of enrichment conditions, and cost-effective scalability, while the high permeability of CCM suggests potential future applications in column setups.

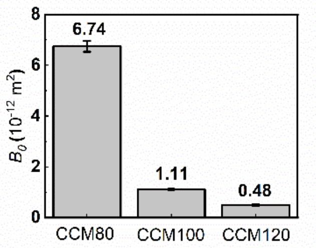

Fig. 1-7. Permeability coefficient (B_0) of citric-acid-modified cellulose monolith (CCM) with different pore sizes.

A conductivity titration was used to calculate the amount of citric acid introduced into the CCM. The results are presented in **Table 1-2**. The number of carboxyl groups introduced onto the monolith increased as the pore size increased. Furthermore, these results show that this method can easily introduce carboxyl groups with high content to CM. According to the results of the permeability and carboxylic content, CCM80 was selected for subsequent experiments.

Table 1-2. Carboxyl content of CCM.

	CCM80	CCM100	CCM120
Carboxyl content / mmol g^{-1}	2.68	2.25	1.62

1.3.3. Adsorption Performance

To assess the adsorption capacity of CCM80, CCM100, and CCM120 for glycopeptides, the loading abilities of pullulan were measured (**Fig. 1-8**). The saturated loading capacity of pullulan on CCM80 was measured to be 71.1 μmol g^{-1}, which is higher than that of CCM100 and CCM120, with saturated loading capacities of 56.9 μmol g^{-1} and 46.3 μmol g^{-1}, respectively. These excellent adsorption performances are attributed to the following factors. After immobilizing citric acid onto CM, the resulting CCM80 contained more abundant carboxyl groups. Carboxyl groups generally contribute to the selective retention of glycopeptides via the interaction with their hydroxyl group through hydrophilic partitioning and hydrogen bonding interactions.[47] The enhancement of hydrophilicity by the incorporation of the carboxyl group allowed CCM80 to interact effectively with hydrophilic target molecules through the HILIC mechanism, making it ideal for glycopeptide enrichment. Also, efficient diffusion property of CCM80 contributes to the greater adsorption performance as well.

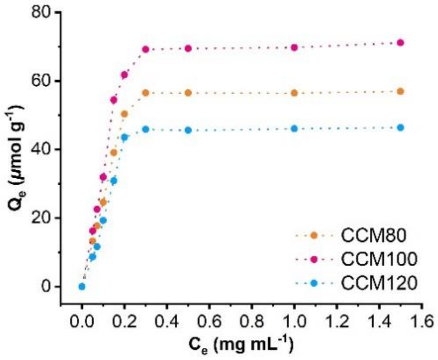

Fig. 1-8. Saturated adsorption isotherms for pullulan adsorbed by CCM80, CCM100, and CCM120.

1.3.4. Enrichment of glycopeptides

The solvent composition of the loading buffer, particularly the ratio of the less-polar solvent (acetonitrile, ACN) to the polar solvent (water), plays a crucial role in the chromatographic enrichment of peptides.[48] The retention behavior of glycopeptides on the monolith's surface is significantly influenced by the solvent ratio, leveraging the differential hydrophilicity between glycopeptides and non-glycopeptides. Due to their hydrophilic interactions facilitated by hydroxyl groups on glycans, Glycopeptides are adsorbed and retained on the porous skeletal surface within the loading buffer. In contrast, non-glycopeptides are removed during the loading buffer treatment due to their lesser hydrophilicity. To elute glycopeptides, the water proportion in the elution buffer is increased to diminish the hydrophilic interaction between glycopeptides and the stationary phase, thereby releasing the glycopeptides from the monolith.[15,49] As a result, glycopeptides are separated from non-glycopeptides and enriched for subsequent MS analysis.

An investigation was conducted to determine the optimal ACN concentration in the loading buffer for effective glycopeptide enrichment. Control experiments involving direct MALDI-TOF analysis of unenriched, purified IgG trypsin digests (**Fig. 1-9**) highlighted the challenge of detecting glycopeptides amidst a significant presence of non-glycopeptides, which suppressed the glycopeptide signal. The study then examined the impact of varying ACN concentrations in the loading buffer on glycopeptide enrichment efficacy using CCM80 (**Fig. 1-10)**. The addition of 1 vol% TFA) to the ACN/water mixture was critical for peptide neutralization through ion pairing effects, facilitating clearer separation of glycopeptides from non-glycopeptides[50].

The findings revealed that using an ACN/H_2O/TFA (75/24/1, v/v/v) loading buffer resulted in the complete disappearance of non-glycopeptide signals, though only a limited number of glycopeptides were detected (**Fig. 1-10a**). In contrast, a loading buffer with ACN/H_2O/TFA (77/22/1, v/v/v) significantly reduced non-glycopeptide signals and enhanced the detection of a wider variety of glycopeptides (**Fig. 1-10b**). An ACN/H_2O/TFA (79/20/1, v/v/v) ratio further decreased non-glycopeptide presence and provided clear, intense signals for glycopeptides (**Fig. 1-10c**). However, increasing the ACN concentration beyond 81% led to the detection of both

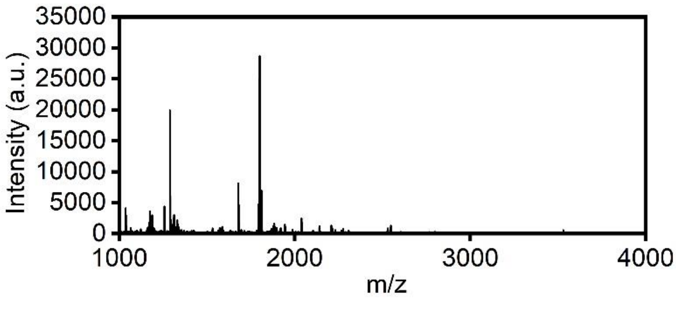

Fig. 1-9. MALDI-TOF mass spectra of direct analysis of the tryptic digest of IgG after being purified using the SPE column.

glycopeptide and non-glycopeptide molecular weights without significant selectivity (**Fig. 1-10d–f**). The optimal loading buffer composition was identified as ACN/H_2O/TFA (79/20/1, v/v/v), which enabled the characterization of 35 glycopeptides with minimal interference from non-glycopeptides (**Fig. 1-10c**), thereby chosen for subsequent enrichment experiments. The ability of CCM100 and CCM120 to enrich glycopeptides was also tested using the same conditions. CCM100 and CCM120 can be enriched with 28 glycopeptides and 19 glycopeptides, respectively. Because of the differences among the above properties, CCM80 was selected for subsequent experiments.

The detection sensitivity of CCM80 was evaluated based on the low quantity of glycopeptides in the analyzed biological specimens (**Fig. 1-11**). From 2.5 fmol μL^{-1} of the IgG trypsin digest, which is more than a thousand-fold dilution of the original specimen, 16 glycopeptides were detected after the glycopeptide enrichment (**Fig. 1-11a**). Most importantly, 11 glycopeptides were still detected when the concentration of the IgG trypsin digest was lowered to 0.25 fmol μL^{-1} (**Fig. 1-11b**). No significant peak was observed in the lower concentration of 0.05 fmol μL^{-1}. These findings demonstrate that CCM80 exhibits remarkable sensitivity to glycopeptide enrichment with a significantly low detection limit of glycopeptide at 0.25 fmol μL^{-1}.

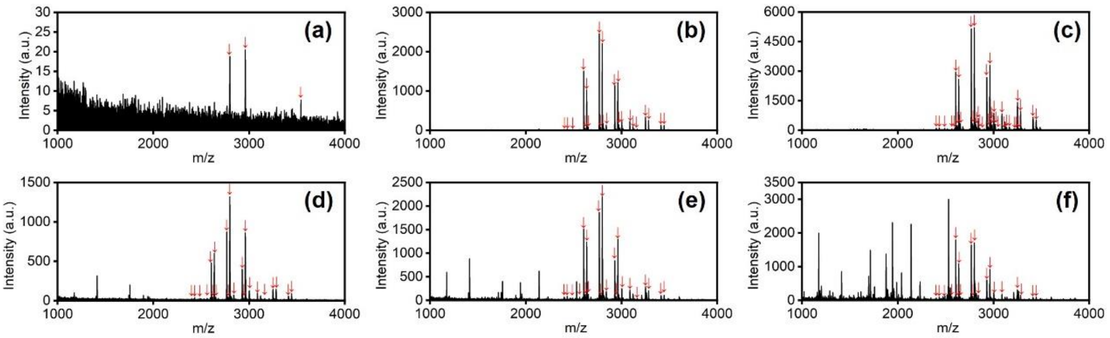

Fig. 1-10. MALDI-TOF mass spectra of glycopeptides from IgG digest after enrichment by citric-acid modified-cellulose monolith CCM80 with different ACN content: (a) ACN/H_2O/TFA (75/24/1, v/v/v), (b) ACN/H_2O/TFA (77/22/1, v/v/v), (c) ACN/H_2O/TFA (79/20/1, v/v/v), (d) ACN/H_2O/TFA (81/18/1, v/v/v), (e) ACN/H_2O/TFA (83/16/1, v/v/v), and (f) ACN/H_2O/TFA (85/14/1, v/v/v); identified glycopeptide peaks were marked with the symbol↓.

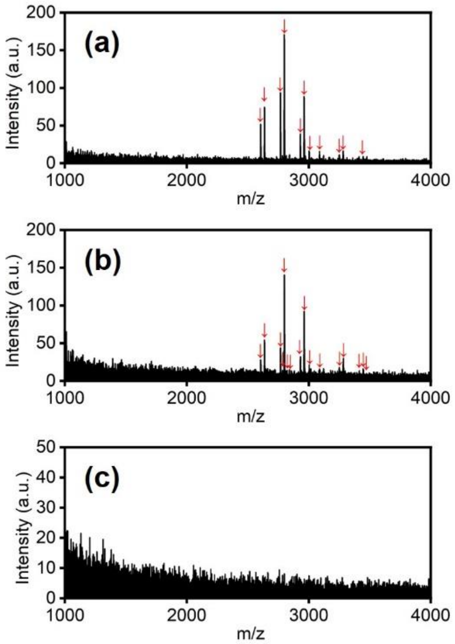

Fig. 1-11. MALDI-TOF mass spectra of glycopeptides from different amount of IgG digest after enrichment with loading buffer ACN/H_2O/TFA (79/20/1, v/v/v): (a) 2.5 fmol μL^{-1} IgG, (b) 0.25 fmol μL^{-1} IgG, (c) 0.05 fmol μL^{-1} IgG; identified glycopeptide peaks were marked with the symbol ↓.

Glycopeptides derived from the trypsin digestion of IgG are relatively abundant because IgG is a well-glycosylated protein. However, in complex biological samples, non-glycopeptides significantly outnumber glycopeptides. Thus, there is a crucial need for selective glycopeptide detection from systems contaminated with a large number of non-glycopeptides.[51] The HILIC technique is employed to meet this need. To further evaluate the selectivity of CCM80 in such contaminated systems, a mixture of trypsin digests from IgG and BSA), a non-glycosylated protein was utilized in enrichment experiments (**Fig. 1-12**).

The enrichment experiments with varying molar ratios of IgG to BSA trypsin digests highlighted the exceptional selectivity of CCM80. At a 1/100 molar ratio of IgG to BSA trypsin digests, 29 glycopeptides were successfully identified, with nearly complete elimination of non-glycopeptide interference (**Fig. 1-12a**). This high level of selectivity persisted even when the molar ratio was increased to 1/500, resulting in the identification of 22 glycopeptides (**Fig. 1-12b**) and negligible detection of non-glycopeptides. Remarkably, even at a 1/1000 molar ratio (**Fig. 1-12c)**, where non-glycopeptide signals were minimally present, 16 glycopeptides were still identified. These results from the BSA interference experiments underscore the high selectivity of CCM80 for glycopeptide enrichment, demonstrating its effectiveness in

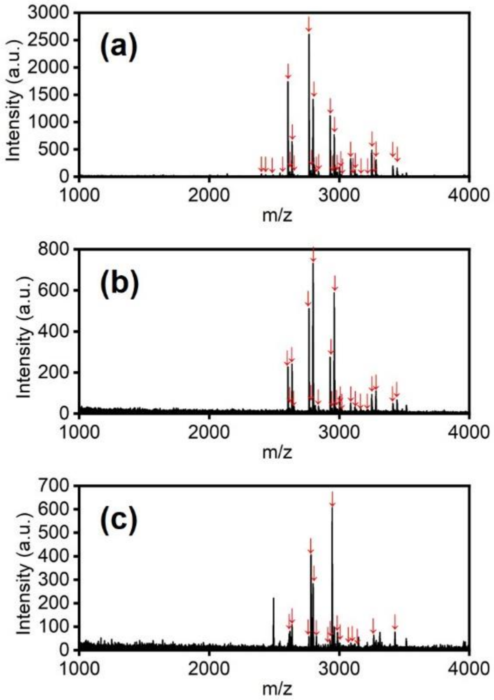

Fig. 1-12. MALDI-TOF mass spectra of glycopeptides from different mole ratio of IgG and BSA digest after enrichment with loading buffer ACN/H_2O/TFA (79/20/1, v/v/v): (a) IgG/BSA = 1/100, (b) IgG/BSA = 1/500, and (c) IgG/BSA = 1/1000; identified glycopeptide peaks were marked with the symbol↓.

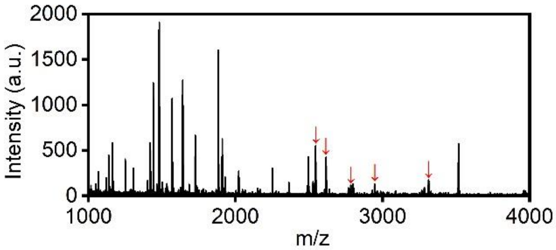

Fig. 1-13. MALDI-TOF mass spectra of glycopeptides from the mole ratio IgG/BSA = 1/500 after enrichment with loading buffer ACN/H_2O/TFA (79/20/1, v/v/v) by CM80. Identified glycopeptide peaks were marked with the symbol ↓.

selectively isolating glycopeptides from samples heavily contaminated with non-glycopeptides.

To compare the efficacy of glycopeptide enrichment, cellulose monolith 80 (CM80) was tested alongside citric-acid-modified cellulose monolith 80 (CCM80). In experiments involving a 1/500 molar ratio of IgG to BSA trypsin digests, CM80 enrichment (**Fig. 1-13**) outcomes revealed a substantial presence of non-glycopeptide signals, which overshadowed glycopeptide signals due to the prevalence of non-glycopeptides. Conversely, when using CCM80 for enrichment, 22 glycopeptides were identifiable, with negligible detection of non-glycopeptide signals (**Fig. 1-12b**). This comparison highlights the superior enrichment capability of CCM80

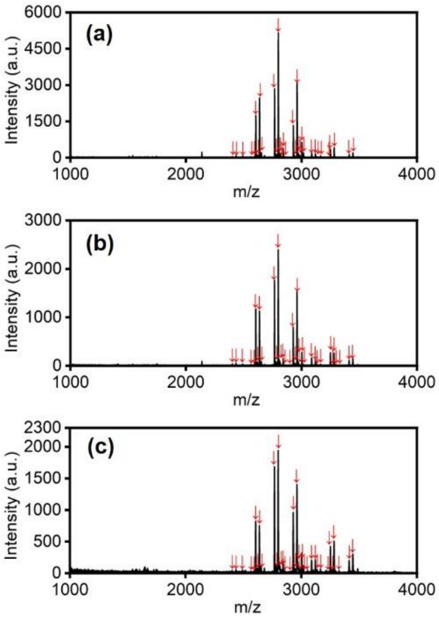

Fig. 1-14. MALDI-TOF mass spectra of glycopeptides from 5-cycles-enrichment experiments with loading buffer ACN/H_2O/TFA (79/20/1, v/v/v); samples were washed with 30% acetonitrile buffer thrice between each cycle: (a) cycle 1, (b) cycle 3, and (c) cycle 5; identified glycopeptide peaks were marked with the symbol ↓.

in a contaminated system, underscoring the beneficial effect of incorporating carboxylic acid groups into the hydrophilic stationary phase for enhancing glycopeptide enrichment selectivity.

The sustainability and eco-friendliness of a material are significantly determined by its reusability. To assess the reusability of CCM80, five glycopeptide enrichment cycles were conducted using 2 μg of IgG tryptic digest. Following each cycle, the samples underwent three washes with a buffer consisting of ACN/H_2O/TFA (30/69/1, v/v/v). The consistency in glycopeptide enrichment results across all cycles (**Fig. 1-14**) underscored the robust reusability of CCM80. This finding indicates CCM80's potential as a sustainable and eco-friendly material and its efficiency in maintaining performance over multiple enrichment cycles.

Finally, the enrichment ability of CCM for actual biological samples was investigated. Plasma was initially selected from human serum and used the same enzymatic digestion method as for IgG. Due to human serum samples usually contain IgG, 6 glycopeptide peaks of IgG can be found in the MALDI-TOF result (**Fig. 1-15**). To further explore the potential applications of CCM, human hepatocellular carcinoma tissue was chosen as a representative biological sample to assess its performance. Following the outlined procedures for processing hepatocellular carcinoma tissue samples and performing deglycosylation using PNGaseF, the resulting

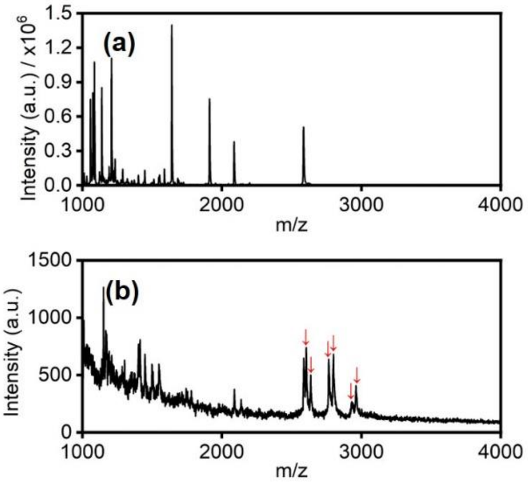

Fig. 1-15. MALDI-TOF mass spectra of (a) peptides from human serum samples, (b) glycopeptides enriched by CCM80 with loading buffer ACN/H_2O/TFA (79/20/1, v/v/v); identified glycopeptide peaks were marked with the symbol ↓.

products were analyzed by LC–MS/MS. Through three parallel enrichment experiments with CCM80 and subsequent database searches of the experimental data, 641 unique N-glycosylation sites of 698 unique glycopeptides from 393 glycosylated proteins were identified from a 900 µg sample (**Fig. 1-16**). These findings highlight the exceptional selectivity and efficiency of CCM80 in glycopeptide enrichment, demonstrating its potential for broad application in the analysis of complex biological samples.

The detection sensitivities of different materials can be compared using the data in **Table 1-3**. Most significantly, CCM80 enriched most glycopeptides from the IgG tryptic digest compared to the other materials.

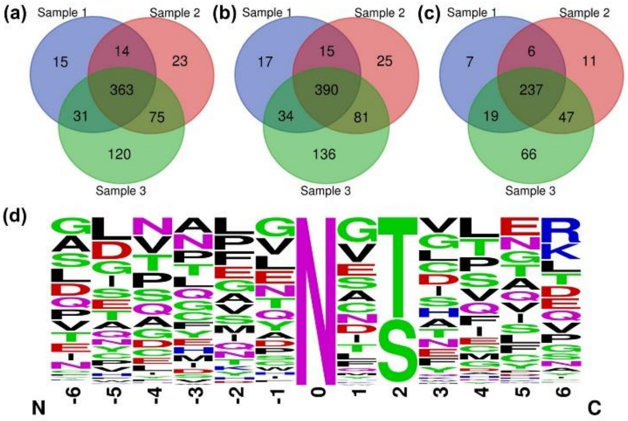

Fig. 1-16. Venn diagrams of (a) N-glycosylation sites, (b) N-glycopeptides, and (c) N-glycoproteins after enriched by CCM80, and (d) Sequence motif of N-glycosite visualized by WebLogo.

Table 1-3. Comparison of the enrichment performances of different materials for enriching glycopeptides.

Material	Selectivity of glycopeptide (IgG/BSA molar ratio)	Limit of detection (fmol μL^{-1})	Identified glycopeptide numbers	Ref.
MIL-101(Cr)-NH_2@PAMAM	1/100	1	14	50
PSDVB–PAM	1/364	/	22	51
MoS_2/Au-NP–L-cysteine	1/1250	0.1	32	52
BHCM	1/500	0.25	33	13
mMOF@Au-MSA	1/100	0.5	29	43
Fe_3O_4@mTiO_2-MSA	1/100	1	22	53
N-wood & D-wood	1/345	10	36 and 38	54
PNI-*co*-ATBA0.2@SiO_2	1/500	/	39	55
Ti^{4+}-immobilized MARs	1/10	1	27	56
GO@CS@ZIF-8 foam	1/500	1	27	57
magCDP@Ada-MSA	1/500	0.1	27	58
MMA/EGDMA/1,2-epoxy-5-hexene-cysteic acid	1/200	0.1	35	59
CCM80	1/1000	0.25	35	This work

1.4. Conclusions

A CCM was crafted using a straightforward and environmentally friendly approach to advance the development of porous materials suitable for the HILIC stationary phase. This method, leveraging the TIPS technique, utilized cellulose and citric acid—both abundant biomass resources. The resulting CCM featured a distinctive coral-like skeletal structure with continuous pores and a rough surface. These characteristics significantly enhanced the specific surface area, facilitated high permeability of the mobile phase, and promoted efficient mass transfer.

In glycopeptide enrichment, CCM exhibited remarkable selectivity and sensitivity for enriching glycopeptides from trypsin-digested immunoglobulin G (IgG), serving as a model protein. It successfully identified 35 glycopeptide species with minimal detection of non-glycopeptides. Moreover, the material demonstrated excellent detection sensitivity, with a lower limit of 0.25 fmol μL^{-1}. Its enrichment capability remained robust, even in samples heavily contaminated with non-glycopeptides from BSA, maintaining selectivity at an IgG/BSA ratio of 1/1000. Additionally, the material's reusability as a HILIC stationary phase underscores the sustainability of this system. Furthermore, CCM demonstrated broad applicability and remarkable selectivity across various types of glycopeptides, highlighting its significant potential for the enrichment of glycopeptides from complex biological samples.

The development of CCM represents a significant step forward in protein glycosylation studies. Its ability to efficiently and selectively enrich glycopeptides underlines its potential contribution to medical science and pharmaceutical research, particularly in protein-based therapeutics and diagnostics. This innovative material offers valuable insights and advancements in understanding protein glycosylation, a critical post-translational modification with profound implications for biological function and disease.

1.5. References

(1) Winterburn, P. J.; Phelps, C. F. *Nature* **1972**, *236*, 147.

(2) Carmi, Y.; Spitzer, M. H.; Linde, I. L.; Burt, B. M.; Prestwood, T. R.; Perlman, N.; Davidson, M. G.; Kenkel, J. A.; Segal, E.; Pusapati, G. V.; Bhattacharya, N.; Engleman, E. G. Allogeneic IgG Combined with Dendritic Cell Stimuli Induce Antitumour T-Cell Immunity. *Nature* **2015**, *521* (7550), 99–104.

(3) Rudd, P. M.; Elliott, T.; Cresswell, P.; Wilson, I. A.; Dwek, R. A. Glycosylation and the Immune System. *Science* **2001**, *291* (5512), 2370–2376.

(4) Ervasti, J. M.; Ohlendieck, K.; Kahl, S. D.; Gaver, M. G.; Campbell, K. P. Deficiency of a Glycoprotein Component of the Dystrophin Complex in Dystrophic Muscle. *Nature* **1990**, *345* (6273), 315–319.

(5) Nilsson, I. M.; Yamashina, I. Effect of Human A1-Acid Glycoprotein on Blood Coagulation. *Nature* **1958**, *181* (4610), 711–712.

(6) Zhang, Q.; Ma, C.; Chin, L.-S.; Li, L. Integrative Glycoproteomics Reveals Protein N-Glycosylation Aberrations and Glycoproteomic Network Alterations in Alzheimer's Disease. *Sci. Adv.* **2020**, *6* (40), eabc5802.

(7) Lowe, J. B. Glycosylation, Immunity, and Autoimmunity. *Cell* **2001**, *104* (6), 809–812.

(8) Smith, B. A. H.; Bertozzi, C. R. The Clinical Impact of Glycobiology: Targeting Selectins, Siglecs and Mammalian Glycans. *Nat. Rev. Drug Discov.* **2021**, *20* (3), 217–243.

(9) Shu, Q.; Li, M.; Shu, L.; An, Z.; Wang, J.; Lv, H.; Yang, M.; Cai, T.; Hu, T.; Fu, Y.; Yang, F. Large-Scale Identification of N-Linked Intact Glycopeptides in Human Serum Using

HILIC Enrichment and Spectral Library Search. *Mol. Cell. Proteomics* **2020**, *19* (4), 672–689.

(10) Leymarie, N.; Zaia, J. Effective Use of Mass Spectrometry for Glycan and Glycopeptide Structural Analysis. *Anal. Chem.* **2012**, *84* (7), 3040–3048.

(11) Domon, B.; Aebersold, R. Mass Spectrometry and Protein Analysis. *Science* **2006**, *312* (5771), 212–217.

(12) Yang, Y.; Franc, V.; Heck, A. J. R. Glycoproteomics: A Balance between High-Throughput and In-Depth Analysis. *Trends Biotechnol.* **2017**, *35* (7), 598–609.

(13) Zhang, L.; Ma, S.; Chen, Y.; Wang, Y.; Ou, J.; Uyama, H.; Ye, M. Facile Fabrication of Biomimetic Chitosan Membrane with Honeycomb-Like Structure for Enrichment of Glycosylated Peptides. *Anal. Chem.* **2019**, *91* (4), 2985–2993.

(14) Zhang, Y.; Fonslow, B. R.; Shan, B.; Baek, M.-C.; Yates, J. R. Protein Analysis by Shotgun/Bottom-up Proteomics. *Chem. Rev.* **2013**, *113* (4), 2343–2394.

(15) Mysling, S.; Palmisano, G.; Højrup, P.; Thaysen-Andersen, M. Utilizing Ion-Pairing Hydrophilic Interaction Chromatography Solid Phase Extraction for Efficient Glycopeptide Enrichment in Glycoproteomics. *Anal. Chem.* **2010**, *82* (13), 5598–5609.

(16) Wuhrer, M.; de Boer, A. R.; Deelder, A. M. Structural Glycomics Using Hydrophilic Interaction Chromatography (HILIC) with Mass Spectrometry. *Mass Spectrom. Rev.* **2009**, *28* (2), 192–206.

(17) Liu, Z.; Xu, M.; Zhang, W.; Miao, X.; Wang, P. G.; Li, S.; Yang, S. Recent Development in Hydrophilic Interaction Liquid Chromatography Stationary Materials for Glycopeptide Analysis. *Anal. Methods* **2022**, *14* (44), 4437–4448.

(18) Takegawa, Y.; Deguchi, K.; Keira, T.; Ito, H.; Nakagawa, H.; Nishimura, S.-I. Separation of Isomeric 2-Aminopyridine Derivatized N-Glycans and N-Glycopeptides of Human Serum Immunoglobulin G by Using a Zwitterionic Type of Hydrophilic-Interaction Chromatography. *J. Chromatogr. A* **2006**, *1113* (1–2), 177–181.

(19) Palmisano, G.; Lendal, S. E.; Engholm-Keller, K.; Leth-Larsen, R.; Parker, B. L.; Larsen, M. R. Selective Enrichment of Sialic Acid–Containing Glycopeptides Using Titanium Dioxide Chromatography with Analysis by HILIC and Mass Spectrometry. *Nat. Protoc.* **2010**, *5* (12), 1974–1982.

(20) Liang, X.; Wang, X.; Ren, H.; Jiang, S.; Wang, L.; Liu, S. Gold Nanoparticle Decorated Graphene Oxide/Silica Composite Stationary Phase for High-Performance Liquid Chromatography: Liquid Chromatography. *J. Sep. Sci.* **2014**, *37* (12), 1371–1379.

(21) Jiang, B.; Wu, Q.; Deng, N.; Chen, Y.; Zhang, L.; Liang, Z.; Zhang, Y. Hydrophilic GO/Fe3O4/Au/PEG Nanocomposites for Highly Selective Enrichment of Glycopeptides. *Nanoscale* **2016**, *8* (9), 4894–4897.

(22) Zhang, W.; Han, H.; Bai, H.; Tong, W.; Zhang, Y.; Ying, W.; Qin, W.; Qian, X. A Highly Efficient and Visualized Method for Glycan Enrichment by Self-Assembling Pyrene Derivative Functionalized Free Graphene Oxide. *Anal. Chem.* **2013**, *85* (5), 2703–2709.

(23) Kuo, C.-W.; Wu, I.-L.; Hsiao, H.-H.; Khoo, K.-H. Rapid Glycopeptide Enrichment and N-Glycosylation Site Mapping Strategies Based on Amine-Functionalized Magnetic Nanoparticles. *Anal. Bioanal. Chem.* **2012**, *402* (9), 2765–2776.

(24) Eivazzadeh-Keihan, R.; Bahreinizad, H.; Amiri, Z.; Aliabadi, H. A. M.; Salimi-Bani, M.; Nakisa, A.; Davoodi, F.; Tahmasebi, B.; Ahmadpour, F.; Radinekiyan, F.; Maleki, A.; Hamblin, M. R.; Mahdavi, M.; Madanchi, H. Functionalized Magnetic Nanoparticles for the Separation and Purification of Proteins and Peptides. *TrAC Trends Anal. Chem.* **2021**, *141*, 116291.

(25) Li, Y.; Zhang, X.; Deng, C. Functionalized Magnetic Nanoparticles for Sample Preparation in Proteomics and Peptidomics Analysis. *Chem. Soc. Rev.* **2013**, *42* (21), 8517.

(26) Larsen, M. R.; Jensen, S. S.; Jakobsen, L. A.; Heegaard, N. H. H. Exploring the Sialiome Using Titanium Dioxide Chromatography and Mass Spectrometry. *Mol. Cell. Proteomics* **2007**, *6* (10), 1778–1787.

(27) Ji, Y.; Xiong, Z.; Huang, G.; Liu, J.; Zhang, Z.; Liu, Z.; Ou, J.; Ye, M.; Zou, H. Efficient Enrichment of Glycopeptides Using Metal–Organic Frameworks by Hydrophilic Interaction Chromatography. *The Analyst* **2014**, *139* (19), 4987–4993.

(28) Liu, Q.; Deng, C.; Sun, N. Hydrophilic Tripeptide-Functionalized Magnetic Metal–Organic Frameworks for the Highly Efficient Enrichment of N-Linked Glycopeptides. *Nanoscale* **2018**, *10* (25), 12149–12155.

(29) Ma, W.; Xu, L.; Li, Z.; Sun, Y.; Bai, Y.; Liu, H. Post-Synthetic Modification of an Amino-Functionalized Metal–Organic Framework for Highly Efficient Enrichment of N-Linked

Glycopeptides. *Nanoscale* **2016**, *8* (21), 10908–10912.

(30) Ma, Y.-F.; Yuan, F.; Zhang, X.-H.; Zhou, Y.-L.; Zhang, X.-X. Highly Efficient Enrichment of N-Linked Glycopeptides Using a Hydrophilic Covalent-Organic Framework. *The Analyst* **2017**, *142* (17), 3212–3218.

(31) Wang, J.; Li, J.; Gao, M.; Zhang, X. Self-Assembling Covalent Organic Framework Functionalized Magnetic Graphene Hydrophilic Biocomposites as an Ultrasensitive Matrix for N-Linked Glycopeptide Recognition. *Nanoscale* **2017**, *9* (30), 10750–10756.

(32) Luo, B.; Li, G.; Li, Z.; He, J.; Zhou, J.; Wu, L.; Lan, F.; Wu, Y. Construction of a Magnetic Covalent Organic Framework with Synergistic Affinity Strategy for Enhanced Glycopeptide Enrichment. *J. Mater. Chem. B* **2021**, *9* (32), 6377–6386.

(33) Qing, G.; Yan, J.; He, X.; Li, X.; Liang, X. Recent Advances in Hydrophilic Interaction Liquid Interaction Chromatography Materials for Glycopeptide Enrichment and Glycan Separation. *TrAC Trends Anal. Chem.* **2020**, *124*, 115570.

(34) Xin, Y.; Xiong, Q.; Bai, Q.; Miyamoto, M.; Li, C.; Shen, Y.; Uyama, H. A Hierarchically Porous Cellulose Monolith: A Template-Free Fabricated, Morphology-Tunable, and Easily Functionalizable Platform. *Carbohydr. Polym.* **2017**, *157*, 429–437.

(35) Svec, F.; Fréchet, J. M. J. New Designs of Macroporous Polymers and Supports: From Separation to Biocatalysis. *Science* **1996**, *273* (5272), 205–211.

(36) Svec, Frantisek.; Frechet, J. M. J. Continuous Rods of Macroporous Polymer as High-Performance Liquid Chromatography Separation Media. *Anal. Chem.* **1992**, *64* (7), 820–822.

(37) Zhang, M.; Wei, F.; Zhang, Y.-F.; Nie, J.; Feng, Y.-Q. Novel Polymer Monolith Microextraction Using a Poly(Methacrylic Acid-Ethylene Glycol Dimethacrylate) Monolith and Its Application to Simultaneous Analysis of Several Angiotensin II Receptor Antagonists in Human Urine by Capillary Zone Electrophoresis. *J. Chromatogr. A* **2006**, *1102* (1–2), 294–301.

(38) Béguin, P.; Aubert, J.-P. The Biological Degradation of Cellulose. *FEMS Microbiol. Rev.* **1994**, *13* (1), 25–58.

(39) Boscott, R. J. Solvent-Treated Cellulose Acetate as the Stationary Phase in Partition Chromatography. *Nature* **1947**, *159* (4036), 342–342.

(40) Tabaght, F. E.; Azzaoui, K.; Idrissi, A. E.; Jodeh, S.; Khalaf, B.; Rhazi, L.; Bellaouchi, R.; Asehraou, A.; Hammouti, B.; Sabbahi, R. Synthesis, Characterization, and Biodegradation Studies of New Cellulose-Based Polymers. *Sci. Rep.* **2023**, *13* (1), 1673.

(41) Zhang, L.; Wang, Y.; Pan, L.; Tang, R.; Asoh, T.-A.; Ou, J.; Uyama, H. Fabrication of a Reusable Bifunctional Biomimetic Ti $^{4+}$ -Phosphorylated Cellulose Monolith with a Coral-like Structure for Enrichment of Phosphorylated and Glycosylated Peptides. *Green Chem.* **2021**, *23* (19), 7674–7684.

(42) Cui, X.; Ozaki, A.; Asoh, T.-A.; Uyama, H. Cellulose Modified by Citric Acid Reinforced Poly(Lactic Acid) Resin as Fillers. *Polym. Degrad. Stab.* **2020**, *175*, 109118.

(43) Angumeenal, A. R.; Venkappayya, D. An Overview of Citric Acid Production. *LWT - Food Sci. Technol.* **2013**, *50* (2), 367–370.

(44) Hu, X.; Liu, Q.; Wu, Y.; Deng, Z.; Long, J.; Deng, C. Magnetic Metal-Organic Frameworks Containing Abundant Carboxylic Groups for Highly Effective Enrichment of Glycopeptides in Breast Cancer Serum. *Talanta* **2019**, *204*, 446–454.

(45) Yang, Z.; Asoh, T.-A.; Uyama, H. Removal of Cationic or Anionic Dyes from Water Using Ion Exchange Cellulose Monoliths as Adsorbents. *Bull. Chem. Soc. Jpn.* **2019**, *92* (9), 1453–1461.

(46) Tian, Y.; Tang, R.; Liu, L.; Yu, Y.; Ma, S.; Gong, B.; Ou, J. Glutathione-Modified Ordered Mesoporous Silicas for Enrichment of N-Linked Glycopeptides by Hydrophilic Interaction Chromatography. *Talanta* **2020**, *217*, 121082.

(47) Melnikov, S. M.; Höltzel, A.; Seidel-Morgenstern, A.; Tallarek, U. A Molecular Dynamics Study on the Partitioning Mechanism in Hydrophilic Interaction Chromatography. *Angew. Chem. Int. Ed.* **2012**, *51* (25), 6251–6254.

(48) Xiong, Z.; Chen, Y.; Zhang, L.; Ren, J.; Zhang, Q.; Ye, M.; Zhang, W.; Zou, H. Facile Synthesis of Guanidyl-Functionalized Magnetic Polymer Microspheres for Tunable and Specific Capture of Global Phosphopeptides or Only Multiphosphopeptides. *ACS Appl. Mater. Interfaces* **2014**, *6* (24), 22743–22750.

(49) Ahmad Izaham, A. R.; Ang, C.-S.; Nie, S.; Bird, L. E.; Williamson, N. A.; Scott, N. E. What Are We Missing by Using Hydrophilic Enrichment? Improving Bacterial Glycoproteome Coverage Using Total Proteome and FAIMS Analyses. *J. Proteome Res.*

2021, *20* (1), 599–612.

(50) Hinamoto, Y.; Sugawara, A.; Asoh, T.-A.; Nandi, M.; Uyama, H. Functionalized Cellulose Monolith Based Affinity Chromatography Columns for Efficient Separation of Protein Molecules. *RSC Appl. Polym.* **2023**, *1* (1), 82–96.

(51) de Haan, N.; Reiding, K. R.; Haberger, M.; Reusch, D.; Falck, D.; Wuhrer, M. Linkage-Specific Sialic Acid Derivatization for MALDI-TOF-MS Profiling of IgG Glycopeptides. *Anal. Chem.* **2015**, *87* (16), 8284–8291.

(52) Xia, C.; Jiao, F.; Gao, F.; Wang, H.; Lv, Y.; Shen, Y.; Zhang, Y.; Qian, X. Two-Dimensional MoS 2 -Based Zwitterionic Hydrophilic Interaction Liquid Chromatography Material for the Specific Enrichment of Glycopeptides, *Anal. Chem.* **2018**, *90* (11), 6651–6659.

(53) Sun, N.; Wang, J.; Yao, J.; Chen, H.; Deng, C. Magnetite Nanoparticles Coated with Mercaptosuccinic Acid-Modified Mesoporous Titania as a Hydrophilic Sorbent for Glycopeptides and Phosphopeptides Prior to Their Quantitation by LC-MS/MS, *Microchim. Act*a **2019**, *186* (3), 159.

(54) Zhou, Y.; Sheng, X.; Garemark, J.; Josefsson, L.; Sun, L.; Li, Y.; Emmer, Å. Enrichment of Glycopeptides Using Environmentally Friendly Wood Materials, *Green Chem.* **2020**, *22* (17), 5666–5676.

(55) Lu, Q.; Chen, C.; Xiong, Y.; Li, G.; Zhang, X.; Zhang, Y.; Wang, D.; Zhu, Z.; Li, X.; Qing, G.; Sun, T.; Liang, X. High-Efficiency Phosphopeptide and Glycopeptide Simultaneous Enrichment by Hydrogen Bond–Based Bifunctional Smart Polymer, *Anal. Chem.* **2020**, *92* (9), 6269–6277.

(56) Tang, R.; Yu, Y.; Dong, J.; Yao, Y.; Ma, S.; Ou, J.; Ye, M. Facile Preparation of Bifunctional Adsorbents for Efficiently Enriching N-Glycopeptides and Phosphopeptides, *Anal. Chim. Acta* **2021**, *1144*, 111–120.

(57) Liu, R.; Gao, W.; Yang, J.; Zhang, S.; Wang, C.; Lin, J.; Zhang, S.; Yu, J.; Tang, K. A Novel Graphene Oxide/Chitosan Foam Incorporated with Metal–Organic Framework Stationary Phase for Simultaneous Enrichment of Glycopeptide and Phosphopeptide with High Efficiency, *Anal. Bioanal. Chem.* **2022**, *414* (6), 2251–2263.

(58) Zhao, B.; Wang, Y.; Ma, J.; Jia, Q. Design of a Hydrophilic Mercaptosuccinic Acid-Functionalized β-Cyclodextrin Polymer via Host–Guest Interaction: Toward Highly Efficient Glycopeptide Enrichment, *Analyst* **2022**, *147* (20), 4553–4561.

(59) Sajid, M. S.; Saleem, S.; Jabeen, F.; Najam-ul-Haq, M.; Ressom, H. W. Terpolymeric Platform with Enhanced Hydrophilicity via Cysteic Acid for Serum Intact Glycopeptide Analysis, *Microchim. Acta* **2022**, *189* (8), 277.

Chapter 2. Development of Molecularly Imprinted Cellulose Monoliths for the Selective Separation of Shikimic Acid in Continuous Flow Systems

2.1. Introduction

Influenza poses significant global health challenges, causing seasonal epidemics and occasional pandemics with substantial morbidity and mortality[1–4]. Oseltamivir[5], a neuraminidase inhibitor, is crucial for managing these outbreaks as it reduces viral replication, alleviates symptoms, lowers hospitalization rates, and prevents complications in vulnerable populations[6–8]. Additionally, its prophylactic efficacy in limiting virus transmission highlights its indispensable role in public health and pandemic preparedness[9,10]. Shikimic acid (SA) serves as a crucial intermediate in the synthesis of the antiviral drug oseltamivir[11,12]. It can be obtained through chemical synthesis, microbial fermentation, or extraction from specific plants[13–15]. During early clinical trials, SA used for oseltamivir production was synthesized chemically; however, this approach proved unsuitable for large-scale commercial production[16,17]. While chemical and microbial methods for cost-effective SA production are under development, the majority of SA is still obtained through extraction from the seeds of Chinese star anise (Illicium verum)[18–21]. However, the multistep extraction and purification processes remain expensive. Alternative synthetic pathways for oseltamivir that do not depend on SA have been proposed; however, none have been commercialized to date[22].

In practical extraction processes, SA is typically obtained with various impurities, requiring subsequent isolation and purification steps.[21,23] Several methods have been reported for SA separation, including carbon adsorption[24], recrystallization[25], microsphere adsorption[26,27], and ion exchange chromatography[28,29]. However, these methods face various challenges, such as complex processes, low selectivity, and high energy demands. Therefore, there is a critical need for the development of separation techniques that are straightforward, highly selective, and economically viable for efficiently extracting SA from complex solutions. Molecular imprinting technology (MIT) is a powerful and versatile method for creating synthetic materials with selective recognition capabilities, mimicking the behavior of biological systems such as enzymes or antibodies[30,31]. The core principle of MIT involves the formation of specific molecular recognition sites within a polymer matrix during synthesis[32]. The resulting molecularly imprinted polymer (MIP) exhibits high selectivity and affinity for its target molecule, even in complex mixtures[32,33]. Surface molecular imprinting technology (SMIT) offers several advantages over traditional bulk imprinting methods[34]. By confining recognition sites to the surface or a thin layer, SMIT ensures enhanced accessibility, faster binding kinetics, and improved binding efficiency[35]. SMIT also enables versatile material design on various substrates, facilitates easier template removal, and overcomes steric hindrance issues for macromolecules[36]. These features make SMIT highly effective for applications in biosensors, drug delivery, catalysis, and environmental monitoring[37–39].

Various materials serve as carriers in SMIT, membranes[40,41], metal oxides[42–44], and polymeric microspheres[45–47]. These carrier materials present promising opportunities for surface modification. However, they face several significant limitations. Their extremely small nanopores create substantial resistance to mass transfer, adversely affecting overall performance and efficiency[48]. Additionally, manufacturing these materials is both expensive and complex. The production processes are not only resource-intensive but also harmful to the environment, further contributing to their high production costs. Monoliths, characterized by their hierarchical, continuous, and porous three-dimensional (3D) structures, have gained considerable attention due to their simple preparation and uniform architecture.[49] These structures offer several advantages over particulate materials, including ease of separation, reduced pressure drop, enhanced mass transfer, superior mechanical stability, and customizable geometric designs[50]. Their interconnected porous networks enable efficient fluid flow while minimizing energy consumption[51]. Furthermore, their adaptable shapes make them highly versatile for integration into a wide range of systems, particularly in separation processes.[50] Monoliths provide benefits such as lower back pressure, faster mass transfer kinetics, higher loading capacities, and simpler manufacturing procedures.[52–54] Owing to these structural advantages, the primary advantage of monolith over adsorbent is their direct applicability to continuous flow adsorption systems, eliminating the need for repetitive centrifugation and other operations to achieve efficient adsorption and desorption. Additionally, monoliths, characterized by their unique porous structure and eco-friendly materials such as cellulose, offer a sustainable and efficient alternative to traditional SMIT carrier materials.

In this work, the author prepared an SA surface-imprinted layer based on a cellulose monolith (CM) by introducing surface imprinting layer with boronic acid groups for the adsorption and selective separation of SA. Cellulose, the most abundant natural polymer on Earth, stands out as an eco-friendly and renewable resource, offering an endless supply of raw material for the development of sustainable and biocompatible products.[55] The CM with a coral-like porous structure can be fabricated through the thermally induced phase separation (TIPS) method. To enable selective recognition of SA, the material was engineered by constructing a surface-imprinted layer on the cellulose monolith (CM) backbone, utilizing 4-vinylphenylboronic acid (VPBA) as a boronic-acid functional monomer[56–58]. The reusability and selective separation capacity of the molecularly imprinted cellulose monolith (MIPs-CM) were evaluated through adsorption kinetics and isothermal adsorption studies in a continuous flow system. The MIPs-CM demonstrated enhanced selectivity, and acceptable regeneration ability due to the combined advantages of the surface imprinting strategy and unique structure and morphology provided by monolithic material. Compared to conventional MIP formats such as particulate polymers and membranes, monolithic MIPs offer distinct advantages, including low pressure drop, improved mass transfer, superior mechanical strength, and ease of handling. Their rigid, solid structure allows easy separation from solution without centrifugation, reducing material loss during use. In addition, their structural versatility enables fabrication into various shapes and sizes, making them suitable for scalable continuous flow applications. This study presents a promising strategy for developing eco-friendly adsorbents capable of effectively separating SA from complex plant extracts by leveraging the advantages of monolithic materials.

2.2. Experimental Section

2.2.1. Materials and measurement

L30 CA was acquired from Daicel Corporation (Tokyo, Japan). *N,N*-Dimethylformamide (DMF), methanol (MeOH), and pH 5.0, 6.0 acetate buffer solution were procured from Nacalai Tesque, Inc. (Japan). 1-Hexanol, 3-(trimethoxysilyl)propyl methacrylate (KH570), and SA was obtained from Sigma-Aldrich, while sodium hydroxide (NaOH), hydrochloric acid (HCl), *p*-vinylphenylboronic acid (VPBA), 2,2'-azobis(isobutyronitrile) (AIBN), pyrocatechol (Cat), quercetin (Que) and alizarin (1,2-Doa) were sourced from FUJIFILM Wako Pure Chemical

Industries. pH 7.0, 8.0 KH_2PO_4-NaOH buffer solution and pH 9.0, 10.0 $NaHCO_3$-NaOH buffer solution were obtained from Tokyo Chemical Industry Co., Ltd (Japan). Ethylene dimethacrylate (EGDMA) was purchased from Sigma Co., Ltd. Deionized water for this study was produced by a Milli-Q system (Millipore Corp., Milford, MA, USA).

Fourier transform infrared (FT-IR) spectroscopy was performed using a Thermo Scientific Nicolet iS5 spectrometer equipped with an iD5 ATR attachment. All spectra were acquired at a resolution of 4 cm^{-1} over 100 scans within a spectral range of 4000–500 cm^{-1}. The morphologies of the monoliths were investigated via scanning electron microscopy (SEM) by using a Hitachi S-3000N scanning electron microscope operated at 15 kV. pH measurements of the monolith were conducted with a standard pH electrode 9615-10D connected to a Horiba LAQUA F-74 analyzer. The elemental compositions of the surfaces were calculated using X-ray photoelectron spectroscopy (XPS, Kratos Ultra 2). The Brunauer–Emmett–Teller (BET) surface area was studied by nitrogen adsorption–desorption analysis (Quantachrome Instruments). Samples were vacuum-degassed at 70 1C for 24 h prior to measurement. The pore diameter distribution and pore volume were obtained using the density functional theory (DFT). For XPS, monochromatic Al Kα was used, and the power of analysis was 75 W (wide) and 150 W (narrow). The survey and high-resolution XPS spectra were collected at fixed analyzer pass energies of 160 eV and 10 eV, respectively. To confirm reproducibility, the measurement was performed three times for each sample. The peaks were fitted using CasaXPS Version 2.3.15 (Casa Software Ltd, Japan). The surface elemental composition of the monoliths was measured using energy-dispersive X-ray spectroscopy (EDX, HITACHI, Miniscope TM 3000 equipped with Swift ED 3000). The continuous flow system was operated using a peristaltic pump (EYELA, MP-1000). The concentration of SA was checked using a UV-visible spectrophotometer (HITACHI, U-2810).

2.2.2. Fabrication of CM

The cellulose acetate monolith (CAM) was fabricated using the TIPS method[59]. Initially, CA powder quantities of 2.0 g, 2.5 g, and 3.0 g were individually dissolved in 10 mL of DMF at 90 °C, with continuous stir-ring until a clear and transparent solution was obtained. Subsequently, 15 mL of 1-hexanol was gradually added to each dispersion in three separate 5 mL increments while the stir-ring continued. The resulting CA dispersion was then transferred into a glass tube and left undisturbed at 25 °C overnight to facilitate phase separation. The CAM was formed after several cycles of solvent exchange with methanol at 25 °C, followed by drying. To convert CAM into CM, deacetylation was performed by immersion in a 0.2 mol L^{-1} sodium hydroxide/methanol solution. To eliminate any residual unreacted NaOH on the surface and within the monolith, the nascent CM was extensively rinsed with deionized water until a neutral pH of approximately 7.0 was reached. The final stage involved drying the sample under a vacuum to remove any remaining water, thereby obtaining the CM.

2.2.3. Fabrication of MIPs-CM

The fabrication of MIPs-CM involved a two-step process. First, the functionalization of CM with a double bond (referred to as KH570-CM), followed by the imprinting process conducted on KH570-CM. 0.5 g of CM and 3.0 mL of KH570 were added to a solution containing 20 mL of ethanol and 20 mL of water, and the reaction was carried out at 75 °C for 24 h. The KH570-CM was washed several times with ethanol and water, followed by vacuum drying[60]. VPBA as the functional monomer, EGDMA as the cross-linking agent, AIBN as the initiator, and SA as the template molecule were added to a three-necked flask containing 50 mL of ethanol[56]. The mixture was ultrasonicated for 30 min to obtain the prepolymerization solution. After 0.1 g of KH570-CM was added to the solution, nitrogen was injected into the three-necked flask to eliminate residual air. The polymerization reaction proceeded at 80 °C, and upon completion, the MIPs-CM were washed using deionized water and ethanol. Finally, MIPs-CM containing specific recognition sites for SA was obtained by removing the template using an elution solution composed of methanol and acetic acid (9:1, v/v), followed by vacuum drying at room temperature. The template molecule, shikimic acid, was removed using an acetic acid aqueous solution (10 vol%). The removal process was monitored by UV–vis spectroscopy, and elution was considered complete when no further increase in absorbance at the characteristic wavelength of shikimic acid was observed in the eluent[61]. For comparison, NIPs-CM was synthesized under identical conditions but without the addition of SA.

2.2.4. Adsorption capacities experiments

The adsorption capacities of MIPs-CM, NIPs-CM, and CM were evaluated using a continuous flow system. The monoliths were precisely encased in polytetrafluoroethylene (PTFE) heat-shrinkable tube to construct the flow system, with approximately 0.03 g per operation. A reservoir was filled with 20 mL of SA solution at varying concentrations, and the SA solution circulated using a peristaltic pump set at a flow rate of 3 mL min^{-1}. After being flown through the monolith, the SA solution was recycled back into the reservoir at room temperature. After 1 h of adsorption, the final SA concentrations at different pH levels were measured by UV–Vis spectrophotometry at 213nm, and the binding amounts were calculated by Eq. (2-1):

$$Q_e = \frac{(C_0 - C_e)V}{m}, \tag{2-1}$$

where C_0 and C_e (mg L^{-1}) represent the initial and equilibrium concentrations of SA, respectively, and Q_e (mg g^{-1}) represents the adsorption quantity of SA. V (L) and m (g) are the volume of SA solution and the weight of monoliths.

Furthermore, the binding capacity was investigated through isothermal and kinetic static binding tests. The kinetic adsorption experiment followed a procedure similar to the isothermal tests, with minor changes. Specifically, a monolith sample (approximately 0.03 g) was passed through a continuous flow of SA solution (100 mg L^{-1}, 20 mL, pH = 8) at 298 K from 0 to 120 min. The residual concentration of SA was determined by ultraviolet-visible spectrometry. The process was also conducted in triplicate. To gain deeper insight into the adsorption mechanism, the pseudo-first-order and pseudo-second-order kinetic models were employed to fit the data. The linear fitting equations for these models are provided as Eq. 2-3 and 4 in the supporting information. For the investigation on adsorption isotherm, approximately 0.03 g monolith sample was passed through a continuous flow of SA solution (20 mL, pH = 8) with various concentrations (20, 40, 60, 80, 100 and 120 mg L^{-1}). The test was performed for 240 min under 298 K. The isotherm tests were carried out in triplicate. The adsorption quantity under different concentrations was calculated, and the experimental data were fitted to the Langmuir and Freundlich models. The corresponding equations (Eq. 2-5 and 6) are provided in the supporting information.

2.2.5. Selective binding experiments

The selective recognition ability of MIPs-CM and NIPs-CM for SA was assessed through selective binding experiments, using Cat, Que, and 1,2-Doa as interferents. Typically, MIPs-CM and NIPs-CM were passed through a continuous flow of 20 mL interferent solution at a concentration of 100 mg L^{-1} and continuous adsorption by peristaltic pump for 2 h. Subsequently, the concentrations of the various interferents in the supernatant were measured using UV–Vis spectrophotometry. The absorption wavelengths corresponding to Cat, Que, and 1,2-Doa were 280, 340, and 519 nm, respectively. The imprinting factor (IF) was determined to assess the imprinting efficiency of MIPs-CM using Eq. (2-2) :

$$\mathrm{IF} = \frac{\mathrm{Q_{MIPs}}}{\mathrm{Q_{NIPs}}}, \tag{2-2}$$

where $\mathrm{Q_{MIPs}}$ and $\mathrm{Q_{NIPs}}$ represent the adsorption capacities of MIPs-CM and NIPs-CM, respectively, for SA and its analogues.

2.2.6. Regeneration tests

The reusability of the adsorbents serves as a critical parameter for assessing their adsorption performance. To evaluate this aspect, the reusability of MIPs-CM was examined through a series of adsorption–desorption experiments. Briefly, MIPs-CM was introduced into a solution containing 20 mL of SA (100 mg L^{-1}) and processed through a continuous flow system at room temperature for 2 h. Subsequently, the SA concentration in the supernatant was determined using a UV–Vis spectrophotometer. The eluent, consisting of a methanol/acetic acid solution (9:1, v/v), was used in the subsequent cycle. The adsorbed MIPs-CM were first rinsed with the eluent until no detectable SA remained, followed by washing with water and drying. This adsorption–desorption process was repeated five times, and the corresponding adsorption capacity was calculated. To ensure experimental reproducibility, the entire procedure was performed at least three times.

2.2.7. Rebinding kinetics and adsorption isotherm

The kinetic data of MIPs-CM and NIPs-CM were analyzed using pseudo-first-order and pseudo-second-order models, and the calculating equations were expressed as Eq. 2-3 and Eq. 2-4, respectively.

$$Q_t = Q_e - Q_e \mathrm{e}^{-k_1 \mathrm{t}}, \tag{2-3}$$

where k_1 (min^{-1}) is the rate constant of the pseudo-first adsorption. Q_e and Q_t (mg g^{-1}) are the adsorption capacities at equilibrium and time t (min), respectively. The rate constants k_1, Q_e, and correlation coefficients R^2 were calculated using the slope and intercept of plots of ln (Q_e - Q_t) versus t.

$$Q_t = \frac{k_2 Q_e^2 \mathrm{t}}{1 + k_2 Q_e \mathrm{t}}, \quad (2\text{-}4)$$

where k_2 (mg g^{-1} min^{-1}) was the rate constant of the pseudo-second order equation. Here, k_2, Q_e, and correlation coefficients R^2 were calculated from the linear plots of t/Q_t versus t.

The experimental adsorption data were investigated to fit with the Langmuir model (Eq. 2-5) and the Freundlich model (Eq. 2-6).

$$\frac{C_e}{Q_e} = \frac{1}{Q_\mathrm{m}} C_e + \frac{1}{\mathrm{K_a} Q_\mathrm{m}}, \quad (2\text{-}5)$$

$$\log Q_e = \log \mathrm{K_f} + \frac{1}{\mathrm{n}} \log C_e, \quad (2\text{-}6)$$

where Q_e (mg g^{-1}) is the adsorption capacity at equilibrium, C_e (mg L^{-1}) is the SA concentration at equilibrium, $\mathrm{K_f}$ (L mg^{-1}) is the Freundlich constant, n is the heterogeneity factor, and $\mathrm{K_a}$ (L mg^{-1}) and Q_m (mg g^{-1}) are the Langmuir coefficients, indicating an adsorption equilibrium constant and a monolayer capacity, respectively. The Freundlich model explains that the sites on the adsorbent surface are not equal and result in multilayer adsorption, whereas the Langmuir model represents monolayer adsorption on an energetically uniform surface.

2.2.8. Adsorption selectivity

The selectivity coefficient α and relative selectivity coefficient αr were defined as Eq. (2-7), respectively.

$$\alpha = \frac{Q_{e_{SA}}}{Q_{e_M}}, \quad (2\text{-}7)$$

where α represent the selectivity coefficient and relative selectivity coefficient, respectively, and M represents Cat, Que, or 1,2-Doa.

As listed in Table S3, the α values of NIPs-CM for SA with respect to interferents were 2.78, 12.5, and 5.85, which were rather low compared with those of MIPs-CM. These results should be ascribed to the different affinities between the interferents and MIPs-CM. The IF represents the relative adsorption affinity of the imprinted compound. The IF values of Cat, Que, and 1,2-Doa are 1.17, 1.24, and 1.21 lower than that of SA, respectively, which contrasts with the trend observed for α. These results suggest that MIPs-CM exhibited excellent selectivity for the SA owing to the imprinting effect.

2.3. Results and discussion

2.3.1. Fabrication and Characterization of MIPs-CM

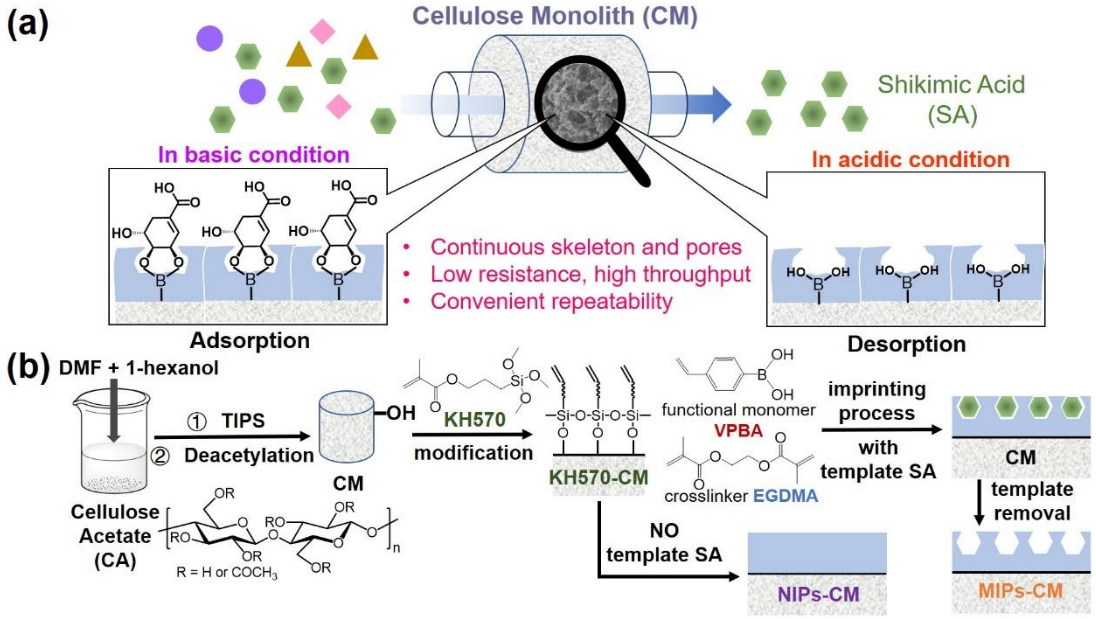

Fig. 2-1. (a) Schematic illustration of MIPs-CM separation of SA. (b) Fabrication process of the MIPs-CM and NIPs-CM.

The molecularly imprinted polymer cellulose monolith (MIPs-CM) was fabricated by immobilizing a molecularly imprinted layer on the surface of the porous framework, using SA as the target template (**Fig. 2-1**). The CM, featuring a co-continuous porous structure, was employed as the supporting material to facilitate the flow system. To realize excellent recognition properties, *p*-vinylphenylboronic acid (VPBA), which can selectively bind to SA, was used as a functional monomer for the creation of molecularly imprinted polymers (MIPs) layers[62]. The CM was initially prepared from cellulose acetate using the TIPS method and simple deacetylation procedure[51]. Notably, prior to deacetylation, no apparent difference in appearance was observed between CAM and CM, indicating that the monolith maintained sufficient strength to retain its shape after chemical treatment. For the subsequent imprinting polymerization process, the CM was first treated with KH570, a silane coupling agent containing a methacryloyl group. Subsequently, a surface imprinting method was applied to the KH570-CM via radical polymerization of VPBA and a cross-linker EGDMA in the presence of SA as the template molecule. SA could selectively and specifically bind to VPBA via boronic ester bond, contributing to the effective creation of the imprinted sites on the MIPs layer through the polymerization. Finally, to remove the template of SA from the MIPs-CM, methanol/acetic acid mixture (9:1, V/V, pH = 3.6) was used, and the monolith was subsequently dried under vacuum. Non-imprinted polymers cellulose monoliths (NIP-CM) were also prepared with the same method except without the template SA. In the MIPs-CM, the imprinted cavities on the surface of MIPs-CM were not only structurally complementary to SA but also contained boronic acid groups capable of interacting with the *cis*-diol structure of SA to form a cyclic boronic ester complex. By leveraging the synergistic effect of the imprinted cavities and boronic acid groups, the adsorbent can be designed to efficiently separate and purify SA. The incorporation of imprinted cavities is expected to effectively minimize the impact of interfering substances on adsorption accuracy, contributing to improved product purity. Under alkaline conditions, the boronic acid groups and the *cis*-diol structure of SA form a pentacyclic ester, whereas under acidic conditions, the pentacyclic ester dissociates, facilitating the release of SA[63,64]. Accordingly, selecting VPBA as the functional monomer not only enables the selective recognition of *cis*-dihydroxy-containing compounds but also allows for the controlled adsorption and desorption of SA by adjusting the pH, thereby significantly improving separation efficiency.

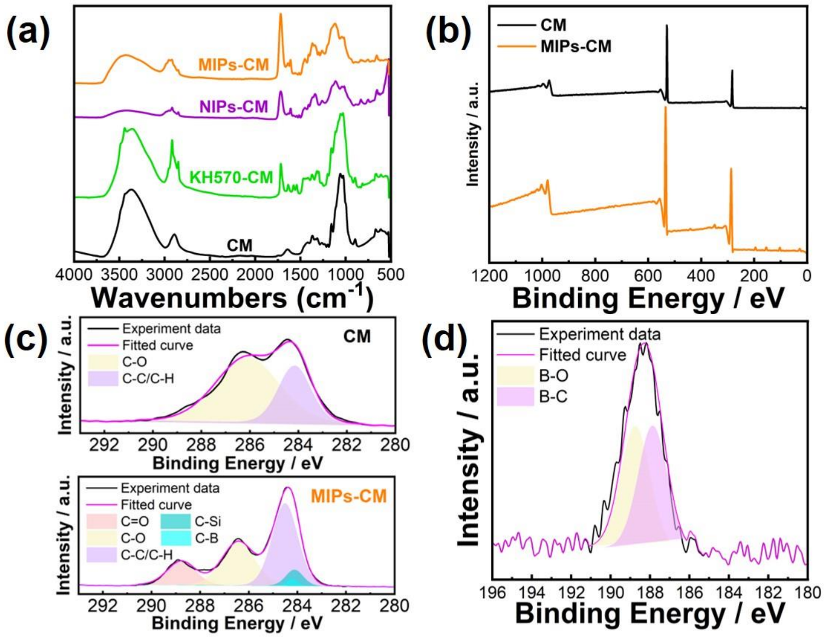

Fig. 2-2. (a) FT-IR spectra of CM, KH570-CM, NIPs-CM and MIPs-CM; (b) XPS survey spectra of CM and MIPs-CM; high-resolution XPS spectra of (c) C1s-CM and C1s-MIPs-CM and (d) B1s-MIPs-CM.

FT-IR spectroscopy was employed to examine changes in surface functional groups on the monoliths, and the corresponding FT-IR spectra of CM, KH570-CM, NIPs-CM and MIPs-CM are presented in **Fig. 2-2a**. In the spectrum of KH570-CM, the most prominent peaks correspond to the asymmetric stretching vibration of methyl and the symmetric stretching vibration of methylene, observed at 2952 cm^{-1} and 2842 cm^{-1}, respectively, which are attributed to the methyl and propyl groups of KH570. Additionally, the peak at 1646 cm^{-1} is associated with the stretching vibration of the C=C bond of methacryloyl group. The characteristic absorption peaks at 1083 cm^{-1} and 818 cm^{-1} correspond to the Si–O bond in KH570, confirming the successful surface modification of CM by KH570. Following the imprinting polymerization process, the FT-IR spectra of NIPs-CM and MIPs-CM exhibit similar profiles, with slight variations compared to KH570-CM. The disappearance of the C=C bond peak at 1646 cm^{-1} likely results from the formation of the imprinting layer on the CM surface. These results confirm the successful synthesis of MIPs-CM.

X-ray photoelectron spectroscopy (XPS) was further conducted to analyze the composition of CM and MIPs-CM. **Fig. 2-2b** presents the wide-scan XPS spectra of CM and MIPs-CM. In the spectrum of CM, the C 1s and O 1s peaks were observed at 284.4 eV and 534.3 eV, respectively. In contrast, the spectrum of MIPs-CM revealed the emergence of three new peaks at 154.5 eV, 103.4 eV, and 188.2 eV, corresponding to Si 2s, Si 2p, and B 1s, respectively, indicating the successful formation of the imprinted polymer on the CM surface. Furthermore, as shown in **Fig. 2-2c**, a new peak corresponding to C=O appeared in the spectrum of MIPs-CM. In addition, the narrow scan of B 1s in MIPs-CM was deconvoluted into two

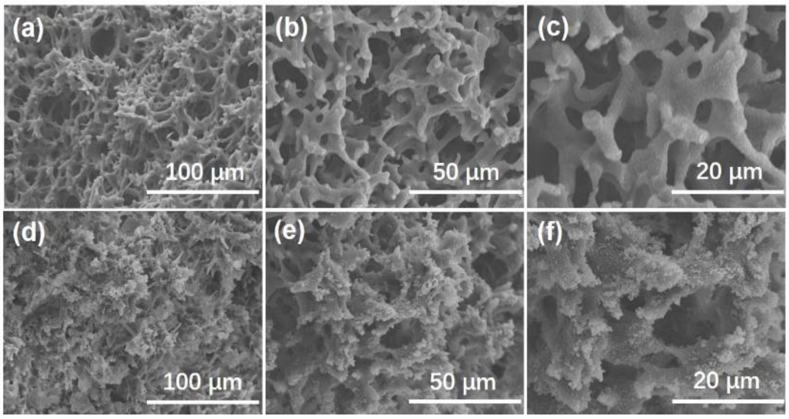

Fig. 2-3. SEM images of (a, b, c) CM and (d, e, f) MIPs-CM.

peaks with binding energies of 187.8 eV and 188.7 eV, which were attributed to B–O and B–C bonds, respectively (**Fig. 2-3d**)[65]. The presence of the B 1s peak strongly confirms the successful formation of the surface layer with boronic acid groups.

The morphological characteristics of the CM and MIPs-CM were examined through scanning electron microscopy (SEM) (**Fig. 2-3**). The CM exhibited a distinctive three-dimensional continuous porous architecture featuring a coral-like morphology, with surface topography providing compelling evidence of the successful molecular imprinting process. Such architectural features confer significant advantages by mitigating steric hindrance between target molecules and the material during separation processes, while simultaneously augmenting potential adsorption sites. Following the post-imprinting polymerization procedure, the MIPs-CM maintained its intricate coral-like skeletal framework, with a uniform distribution of imprinting particles across the CM surface, which provides compelling evidence of the successful implementation of the molecular imprinting process. The corresponding elemental mapping of MIPs-CM (**Fig. 2-4**) reveals a homogeneous spatial distribution of B, C, O, and Si elements throughout the membrane, demonstrating the successful construction of imprinted layer on the CM substrate.

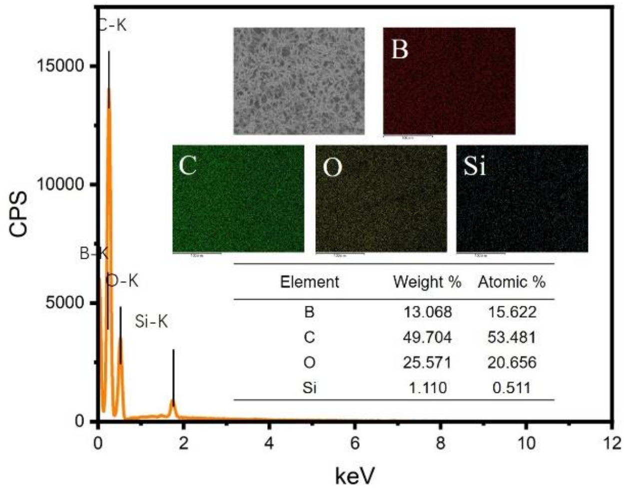

Element	Weight %	Atomic %
B	13.068	15.622
C	49.704	53.481
O	25.571	20.656
Si	1.110	0.511

Fig. 2-4. Corresponding element mapping and SEM images (inset) of MIPs-CM.

The N_2 adsorption–desorption analysis of CM and MIPs-CM was conducted to evaluate their pore structure and surface area. As shown in **Fig. 2-5**, the CM presents type IV isotherms, The adsorption increases slowly at low P/P_0 (< 0.2), followed by a sharp increase at high P/P_0 (> 0.8). This trend suggests that the material has a large pore structure, probably dominated by mesopores and macropores. The adsorption and desorption curves bifurcate significantly at P/P_0

≈ 0.6-1.0, forming an H3-type hysteresis loop, which indicates that the material has a certain mesoporous structure. The specific surface area of CM was determined to be 4.66 m^2 g^{-1} utilizing the multipoint Brunauer–Emmett–Teller (BET) equation. These results suggest that the pores of CM may consist of lamellar or fissured pores or irregular macropores. After the imprinting polymerization process, the N_2 adsorption–desorption isotherms of MIPs-CM also exhibit a type IV behavior. At low P/P_0 (<0.2), the adsorption increases slowly; at $P/P_0 \approx 0.4$-0.8, the amount of adsorption increases steadily, which is characteristic of mesoporous materials. At $P/P_0 > 0.8$, there is a steep increase in adsorption and a clear hysteresis loop, indicating that the material may have some macroporous structure. The adsorption-desorption isotherms exhibit an H2-type hysteresis loop in the relative pressure (P/P_0) range of 0.5–1.0, indicating a mesoporous structure featuring bottle-neck shaped pores with narrow entrances but wider internal cavities. The presence of this hysteresis pattern suggests the successful formation of uniform mesopores arranged in a hierarchical porous network. After MIP modification, the specific surface area was significantly increased to 23.15 m^2 g^{-1}. This change suggests that the introduction of the molecularly imprinted layer effectively increased the number of pores and the available adsorption surface area. The adsorption capacity of the material was significantly enhanced compared to the unmodified samples and may provide better separation of specific target molecules SA.

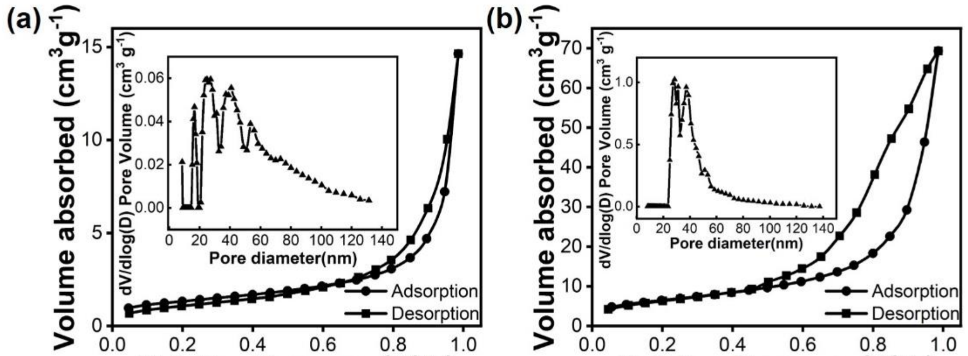

Fig. 2-5. Nitrogen adsorption–desorption curves of (a) CM and (b) MIPs-CM. The corresponding pore size distributions are presented in the insets.

2.3.2. Optimization of the Fabrication Conditions of MIPs-CM

It is well established that various factors involved in the synthesis of MIPs can influence the formation of the imprinted layer and recognition sites, thereby affecting the adsorption capacity of the sample. In the synthesis of MIPs-CM, several parameters were optimized, including the amounts of VPBA, the cross-linker EGDMA, the template molecule SA, and the polymerization time, to enhance the adsorption performance of MIPs-CM.

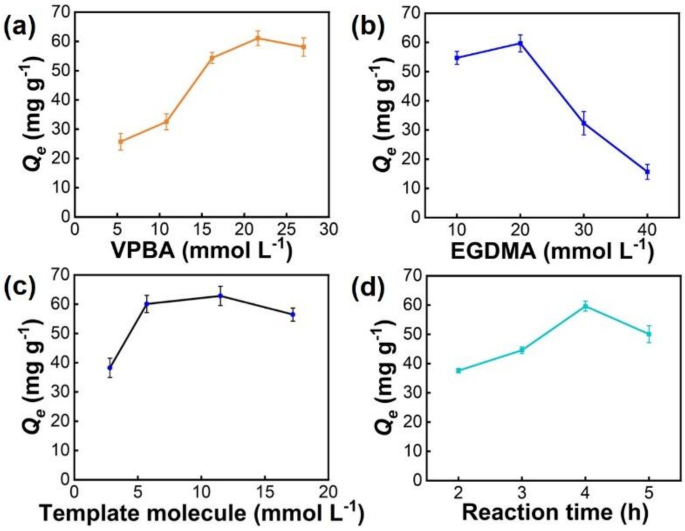

Fig. 2-6. (a) Influences of VPBA dosage, (b) cross-linker volume, (c) template amount, and (d) imprinting polymerization time on the adsorption capacity of MIPs-CM.

First, different amounts of VPBA were introduced to evaluate its effect on adsorption capacity, as the grafted boric acid groups play a pivotal role in determining the adsorption efficiency of MIPs-CM. As shown in **Fig. 2-6a**, the adsorption capacity gradually increases with increasing VPBA content from 40 to 200 mg, reaching a plateau when the VPBA amount exceeds 160 mg. This phenomenon can be attributed to the increasing number of active boric acid groups grafted onto CM, which enhances the availability of binding sites for SA. The adsorption capacity plateau observed beyond 160 mg of VPBA is attributed to the saturation of effective binding sites. While initial increases in VPBA promote the formation of specific recognition sites for the template molecule, excessive VPBA induces non-specific polymerization, steric hindrance, and the generation of inaccessible regions, thereby limiting further enhancement. These results further highlight the significant role of VPBA in improving the adsorption capacity of MIPs-CM.

Furthermore, the effects of cross-linker dosage on the imprinted layer formation and morphology of MIPs-CM were systematically investigated[66]. **Fig. 2-6b** illustrates the adsorption capacity for SA as the cross-linker dosage varies from 100 to 400 μL. Notably, the adsorption capacity exhibits a sharp increase with in the rise in EGDMA volume from 150 to 300 μL. This enhancement can be attributed to the formation of more rigid imprinted sites that facilitate SA recognition. However, when the EGDMA dosage exceeds 200 μL, a noticeable decline in binding capacity is observed due to a reduction in the number of accessible adsorption sites. **Fig. 2-7a–d** presents SEM images of the imprinted products synthesized with different EGDMA amounts (100, 200, 300, and 400 μL). At an EGDMA dosage of 100 μL, the material maintains a morphology similar to CM, with a thin imprinted layer. In contrast, as the EGDMA dosage increases, a progressively thicker imprinted layer forms, which seals the cocontinuous pores and restricts their accessibility to SA. Based on these findings, the optimal cross-linker dosage for this study was determined to be 200 μL.

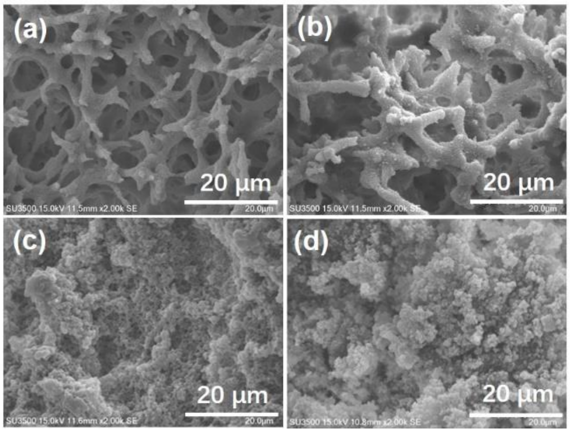

Fig. 2-7. SEM images of MIPs-CM synthesized by different cross-linker volumes: (a) 100 μL, (b) 200 μL, (c) 300 μL, and (d) 400 μL.

Additionally, the effect of template SA dosage (25, 50, 100, and 150 mg) was investigated to determine the optimal balance between the template and functional monomer, and the results are presented in **Fig. 2-6c**. The binding capacity exhibits a continuous increase until the SA dosage reaches 100 mg, after which a decline is observed. This phenomenon is likely due to the optimal dispersion of imprinted sites for SA on the CM substrate occurring at a template dosage of 100 mg. The optimal adsorption capacity observed at 100 mg of shikimic acid is attributed to an ideal template-to-monomer ratio. Exceeding this amount disrupts complex formation, resulting in low-fidelity imprinted sites and reduced adsorption performance due to interference from excess free template molecules during polymerization. The influence of polymerization time on adsorption capacity was also examined, with results shown in **Fig. 2-6d** for reaction durations ranging from 2 to 5 h. The adsorption capacity for SA gradually increases during the first 4 h of polymerization, reaching its maximum at 4 h. However, extending the polymerization time beyond this point results in a slight decrease in adsorption capacity, likely due to a closure of pores along the diffusion path of the target molecule. Based on these findings, the optimal imprinting conditions were determined to be 160 mg of VPBA, 200 μL of EGDMA, 100 mg of SA, and a polymerization time of 4 h. The final MIPs-CM permeability obtained was (1.08 ± 0.97) × 10^{-12} m^2 (**Table 2-1**). Even though there is a decrease compared to CM, MIPs-CM still supports high-speed flow adsorption with low back pressure which demonstrates the strong potential for efficient separation.

Table 2-1. The permeability of MIPs-CM and CM.

	MIPs-CM	CM
B_0 (×10^{-12} m^2)	1.08 ± 0.97	4.18 ± 0.13

2.3.3. Adsorption kinetics and isotherm

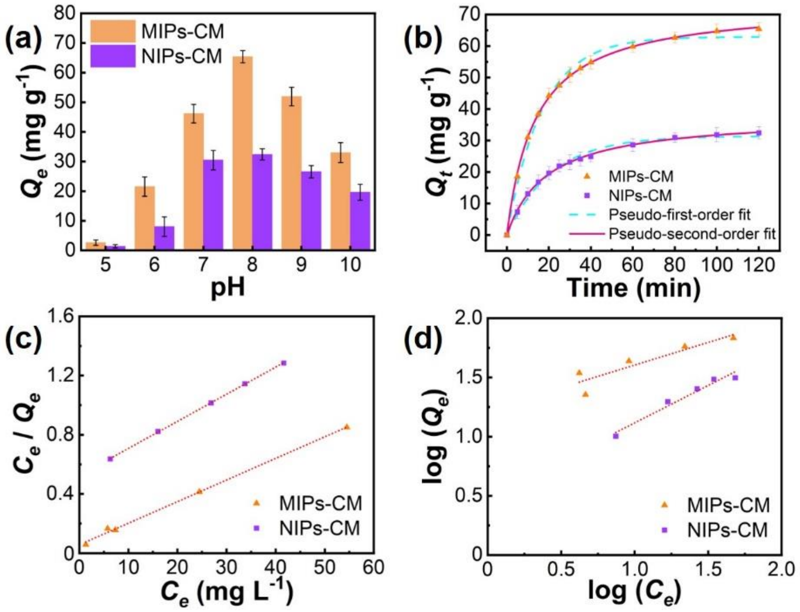

Fig. 2-8. (a) Effect of solution pH on the adsorption amount of MIPs-CM and NIPs-CM for SA, (b) adsorption kinetics study of MIPs-CM and NIPs-CM, (c) Langmuir and (d) Freundlich isotherm of MIPs-CM and NIPs-CM.

The binding affinity between boronic acids and *cis*-diol compounds exhibits strong pH dependence. To assess this effect, an investigation was conducted to evaluate the influence of solution pH (ranging from 5.0 to 10.0) on the adsorption behavior of both MIPs-CM and NIPs-CM. The experimental results, illustrated in **Fig. 2-8a**, demonstrated that both materials exhibited a bell-shaped relationship between adsorption capacity and pH, with optimal binding occurring at pH 8.0. This phenomenon can be attributed to the underlying mechanism of interactions between boronic acid and *cis*-diol. Under alkaline conditions, boronic acid moieties form reversible covalent bonds with the *cis*-diol groups present in SA, whereas these bonds undergo dissociation in acidic environments, facilitating the release of bound analytes. At around pH 8, boronic acids are partially converted to their anionic boronate form, which strongly and selectively interacts with the *cis*-diol groups of shikimic acid. At higher pH, however, the fully deprotonated carboxyl group of shikimic acid introduces additional negative charge, which may lead to electrostatic repulsion with the boronate anions and a slight decrease in binding efficiency. Notably, MIPs-CM displayed marked pH-dependent variations in adsorption capacity, indicating substantial pH influence on binding characteristics. This observation informed the selection of optimal pH conditions for subsequent binding studies. In contrast, NIPs-CM exhibited lower binding capacities and pH sensitivity, which can be attributed to the absence of specific imprinted cavities and reduced surface exposure of boronic acid functionalities. The data presented in **Fig. 2-6a** revealed that MIPs-CM maintained satisfactory binding performance within the ordinary common relevant pH range of 7.0-8.0. This characteristic renders MIPs-CM particularly suitable for practical applications under conventional pH conditions. Based on these findings, pH 5.0 was established as the optimal dissociation condition for subsequent experiments.

To elucidate the adsorption characteristics of the MIPs-CM adsorbent towards SA, comprehensive investigations of adsorption kinetics and isotherms were conducted. The kinetic studies carried out using an initial SA concentration of 100 mg L^{-1}, with particular emphasis on examining the temporal evolution of adsorption capacity. The experimental conditions were maintained at pH 8.0 and 298 K, with both MIPs-CM and NIPs-CM materials being subjected to SA solution for 2 h while monitoring concentration variations at predetermined time intervals. The equilibrium adsorption capacities (Q_t) were calculated utilizing Equations 2-1, with the resultant kinetic profiles illustrated in **Fig. 2-8b**. Both adsorbents exhibited progressive increases in adsorption capacity over time, achieving equilibrium within approximately 2 h. A rapid initial uptake was observed during the first 40 minutes, accounting for more than 95% of the maximum adsorption capacity, indicating efficient occupation of the imprinted cavities by SA template molecules. This rapid adsorption rate indicates that MIPs-CM exhibits low diffusion resistance. This can be attributed to the hierarchical porous structure observed in SEM and BET analyses, which features interconnected macropores and mesopores that promote fast mass transfer to the recognition sites. Subsequently, the adsorption rate diminished due to decreased SA concentration in the solution, ultimately reaching a maximum adsorption capacity of 65.4 mg g^{-1} over the following 80 minutes. While NIPs-CM demonstrated similar adsorption trends, its maximum capacity (32.4 mg g^{-1}) was notably lower than that of MIPs-CM. This disparity can be attributed to the presence of specifically engineered cavities within MIPs-CM that facilitate precise molecular recognition through complementary shape, size, and functional group arrangements. The enhanced adsorption capacity clearly demonstrates the efficacy of the boronic acid-functionalized imprinting methodology. Kinetic modeling was performed using pseudo-first-order and pseudo-second-order models (Eq. 2-3 and 2-4, respectively). The calculated kinetic parameters are presented in **Table 2-2**. The pseudo-second-order model exhibited superior correlation (R^2 = 0.999) compared to the pseudo-first-order model (R^2 = 0.990), indicating that the adsorption mechanisms are predominantly governed by pseudo-second-order kinetics. However, the calculated equilibrium adsorption capacities ($Q_{e,c}$) from the pseudo-first-order model were closer to the experimental values ($Q_{e,e}$) than those from the pseudo-second-order model, indicating a better fit in terms of adsorption capacity. This discrepancy implies that while the adsorption rate may follow pseudo-second-order kinetics, the overall process likely involves physical adsorption rather than purely chemical adsorption.

Table 2-2. Kinetic model parameters obtained in adsorption of SA onto MIPs-CM and NIPs-CM.[a]

Samples	[b] $Q_{e,e}$ (mg g^{-1})	Pseudo-first-order equation			Pseudo-second-order equation		
		[c] $Q_{e,c}$ (mg g^{-1})	k_1 (min^{-1})	R^2	$Q_{e,c}$ (mg g^{-1})	k_2 (g mg^{-1} min^{-1})	R^2
MIPs-CM	65.4	62.9	0.059	0.990	73.4	1.0×10^{-3}	0.999
NIPs-CM	32.4	31.4	0.046	0.989	37.8	1.4×10^{-3}	0.998

[a] The testing condition was pH = 8.0, C_0 = 100 mg L^{-1}, and T = 298K.

[b] $Q_{e,e}$ (mg g^{-1}) is the experimental data of equilibrium rebinding amount.

[c] $Q_{e,c}$ (mg g^{-1}) is the calculated data of equilibrium rebinding amount.

The equilibrium adsorption characteristics of MIPs-CM and NIPs-CM were systematically investigated across varying SA initial concentrations. As depicted in **Fig. 2-8c,d** and **Table 2-3**, the adsorption isotherm analysis reveals distinct adsorption behaviors of SA on MIPs-CM and NIPs-CM. This observation substantiates the critical role of molecular imprinting techniques in enhancing adsorption performance. To elucidate the binding interactions between MIPs-CM and SA more comprehensively, a representative set of experimental values was selected for Langmuir and Freundlich fitting, as articulated in supplementary equations 2-5 and 2-6. In the Langmuir model, the MIPs-CM exhibited a significantly higher maximum adsorption capacity (Q_m) of 77.0 mg g^{-1} compared to 53.4 mg g^{-1} for the NIPs-CM. The adsorption equilibrium constant (K_a) was also higher for MIPs-CM (0.150 L mg^{-1}) than for NIPs-CM (0.035 L mg^{-1}), indicating stronger affinity toward the target molecule. These results suggest that the MIPs-CM possess specific SA recognition sites, enabling efficient and selective adsorption. Similarly, in the Freundlich model, the MIPs-CM showed a markedly higher K_f value (16.9 mg L^{-1}) than that of the NIPs-CM (3.24 mg L^{-1}), supporting the enhanced adsorption capacity of the MIPs. Notably, the 1/n value for MIPs-CM was lower (0.376), indicating greater heterogeneity of the adsorption sites and the presence of high-affinity, selective binding sites. In contrast, the NIPs-CM exhibited a higher 1/n value (0.622), suggesting a more uniform but less selective adsorption behavior. Both models yielded high coefficients of determination (R^2), with the Langmuir model providing particularly good fits (MIPs-CM: 0.993, NIPs-CM: 0.988). This implies that the adsorption process is predominantly governed by monolayer adsorption through specific interactions, consistent with the Langmuir-type behavior.

Consequently, the adsorption isotherm analysis clearly demonstrates that MIPs-CM possess superior binding characteristics toward SA compared to NIPs-CM, as reflected by higher adsorption capacities, stronger binding affinities, and greater site heterogeneity. The Langmuir model provided an excellent fit to the experimental data, indicating that the adsorption process predominantly involves monolayer coverage driven by specific interactions between SA and the imprinted recognition sites. These findings highlight the effectiveness of molecular imprinting in creating highly selective adsorbents with enhanced performance.

Table 2-3. Adsorption isotherm constants obtained in adsorption of SA onto MIPs-CM and NIPs-CM.[a]

Samples	Langmuir model			Freundlich model		
	Q_m (mg g^{-1})	K_a (L mg^{-1})	R^2	K_f (mg L^{-1})	1/n	R^2
MIPs-CM	77.0±6.1	0.150±0.079	0.993±0.005	16.9±4.5	0.376±0.071	0.914±0.065
NIPs-CM	53.4±1.2	0.035±0.001	0.988±0.015	3.24±0.18	0.622±0.016	0.983±0.015

[a] The testing condition was pH = 8.0, adsorption time 120 min, and $T = 298$K.

2.3.4. Binding specificity and reusability

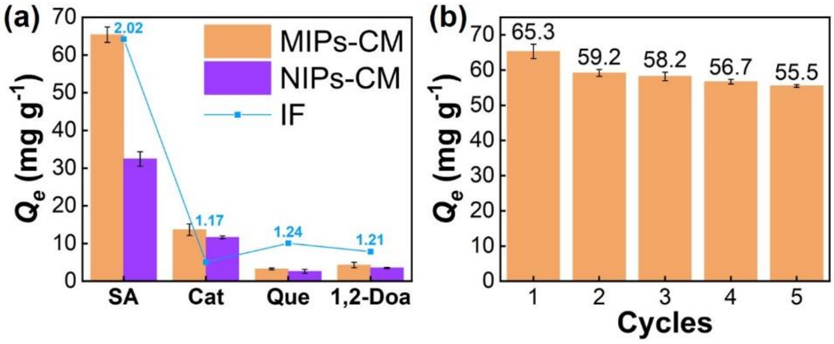

Fig. 2-9. (a) Specific recognition ability of MIPs-CM and NIPs-CM, and (b) the reusability performance of MIPs-CM.

Table 2-4. Adsorption selectivity constants of MIPs-CM and NIPs-CM toward SA.

Target	MIPs-CM		NIPs-CM		IF
	Q_e (mg g^{-1})	α	Q_e (mg g^{-1})	α	
SA	65.4		32.420		2.02
Cat	13.7	4.79	11.648	2.78	1.17
Que	3.24	20.2	2.603	12.5	1.24
1,2-Doa	4.28	15.3	3.532	5.85	1.21

To evaluate the specificity of the adsorbents, three interfering compounds were selected as competitive adsorbates: catechol (Cat), quercetin (Que), and alizarin (1,2-Doa). These compounds were selected based on their structural resemblance to shikimic acid, especially their phenolic character and the presence of vicinal hydroxyl groups, as well as their frequent occurrence in plant-derived materials[67,68,69]. The adsorption capacities of MIPs-CM and NIPs-CM toward these compounds are presented in **Fig. 2-9a**. Notably, MIPs-CM and NIPs-CM exhibited significantly different adsorption capacities for SA and the interfering compounds, primarily due to the presence of the *cis*-diol structure in SA, which can be selectively captured by the boronic acid-functionalized adsorbent. Although these three interfering compounds also contain a *cis*-diol compound, the absence of specific imprinted cavities for them on the surface of MIPs-CM resulted in a lower adsorption capacity. In contrast, the adsorption capacity of NIPs-CM for SA was lower than that of MIPs-CM, owing to the lack of recognition sites. These findings suggest that the presence of imprinted sites enhances adsorption capacity, while boronic acid groups confers selective recognition toward *cis*-diol compounds. The results confirm the specific adsorption ability of MIPs-CM. This conclusion is further supported by the imprinting factor line chart in **Fig. 2-9a**, which shows that the IF of the adsorbents for the interfering compounds ranged from approximately 1.1 to 1.2, whereas the imprinting factor for SA was notably higher, reaching 2.0. Additionally, the selectivity coefficient (α) and IF were calculated (**Table 2-4**). Meanwhile, MIPs-CM and NIPs-CM exhibited similar adsorption capacities for the three interfering compounds, suggesting that the selective binding of MIPs-CM to SA was primarily attributed to the molecular imprinting effect rather than nonspecific physical adsorption.

To evaluate the reusability of MIPs-CM, five regeneration cycles were conducted, and the adsorption capacity after each cycle was calculated and presented in **Fig. 2-9b**. The adsorption capacity of MIPs-CM remained relatively stable, exhibiting only a 15% reduction over successive recycling experiments (decreasing from 65.3 mg g^{-1} to 55.5 mg g^{-1}). Such a decline in adsorption capacity during recycling is commonly observed. The reduction in separation performance after five cycles can be attributed to several factors[70]. First, some imprinted sites may have been partially degraded during the regeneration process, affecting the imprinting efficiency. Second, incomplete elution during repeated use may have resulted in partial blockage of imprinted sites. Third, potential contamination or structural fatigue of the material during recycling could have further contributed to the decrease in adsorption capacity. Also, the compressive stress–strain curves of the monoliths indicate that MIPs-CM exhibits enhanced mechanical stability compared to unmodified CM (**Fig. 2-10**). The smooth and continuous curves suggest uniform deformation behavior without significant structural defects. Notably,

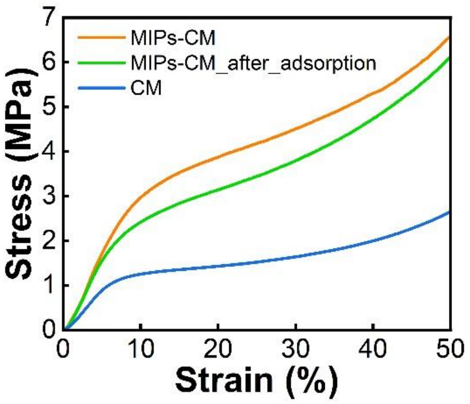

Fig. 2-10. Mechanical strength test results of the dried MIPs-CM, CM and MIPs-CM after absorption/desorption experiment, compressed up to a 50% strain.

MIPs-CM retained comparable mechanical properties even after the adsorption/desorption process, indicating that its structure remained intact during repeated flow-through operations. Overall, the MIPs-CM synthesized in this study demonstrates promising potential for practical applications.

2.4. Conclusions

A boronic acid-functionalized molecularly imprinted monolith (MIPs-CM) was constructed by surface imprinting on a porous cellulose monolith (CM), serving as a robust support for selective adsorption of shikimic acid (SA). The imprinted monolith, featuring a granular imprinted thin layer, exhibited a hierarchical porous structure on both its outer surface and internal pore channels, facilitating efficient mass transfer and enhancing adsorption performance. Compared with traditional methods, MIPs-CM demonstrated improved binding affinity and selectivity toward the target compound, SA, due to the introduction of boronic acid groups as specific functional monomers. The maximum adsorption capacity of the imprinted monolith reached 65.4 mg g^{-1}, nearly twice that of the non-imprinted monolith (32.4 mg g^{-1}). Adsorption isotherm analysis indicated that the Langmuir model provided a good fit, suggesting a quasi-monolayer chemisorption-driven process. Notably, MIPs-CM exhibited strong specificity for SA even in the presence of structural analogs, with imprinting factors (IF) of 1.17, 1.24, and 1.21 for Cat, Que, and 1,2-Doa, respectively, confirming its superior imprinting effect for SA. Furthermore, the monolith demonstrated excellent reusability, maintaining 85% of its initial adsorption capacity after five adsorption-desorption cycles. This study also aligns with several of the 12 Principles of Green Chemistry. Cellulose acetate, a partially synthetic yet environmentally friendly polymer derived from renewable biomass, was used as the starting material (Principle 7: renewable feedstocks). The cellulose monolith was prepared via the thermally induced phase separation (TIPS) method under moderate temperature conditions (80 °C to 20 °C), supporting Principles 6 and 8 (energy efficiency). The MIP layer was formed through a simple, one-step polymerization using an optimized amount of the template SA, minimizing derivatization and waste (Principles 1 and 8). While the MIP layer is not biodegradable, the overall approach emphasizes resource sustainability, reduced process complexity, and environmental responsibility. This study provides valuable insights into the development of highly selective and reusable imprinted monoliths, offering a promising approach for the efficient capture of natural SA and other drug molecules in practical applications.

2.5. References

(1) Palese, P. Influenza: Old and New Threats. *Nat. Med.* **2004**, *10* (S12), S82–S87.

(2) Gao, Y.; Zhao, Y.; Liu, M.; Luo, S.; Chen, Y.; Chen, X.; Zheng, Q.; Xu, J.; Shen, Y.; Zhao, W.; Li, Z.; Huang, S.; Huang, J.; Tian, J.; Guyatt, G.; Hao, Q. Antiviral Medications for Treatment of Nonsevere Influenza: A Systematic Review and Network Meta-Analysis. *JAMA Intern. Med.* **2025**, *185* (3), 293.

(3) Klepser, M. E. Socioeconomic Impact of Seasonal (Epidemic) Influenza and the Role of Over-the-Counter Medicines. *Drugs* **2014**, *74* (13), 1467–1479.

(4) Neumann, G.; Noda, T.; Kawaoka, Y. Emergence and Pandemic Potential of Swine-Origin H1N1 Influenza Virus. *Nature* **2009**, *459* (7249), 931–939.

(5) McClellan, K.; Perry, C. M. Oseltamivir: A Review of Its Use in Influenza. *Drugs* **2001**, *61* (2), 263–283.

(6) Dutkowski, R.; Thakrar, B.; Froehlich, E.; Suter, P.; Oo, C.; Ward, P. Safety and Pharmacology of Oseltamivir in Clinical Use: *Drug Saf.* **2003**, *26* (11), 787–801.

(7) Dobson, J.; Whitley, R. J.; Pocock, S.; Monto, A. S. Oseltamivir Treatment for Influenza in Adults: A Meta-Analysis of Randomised Controlled Trials. *Lancet* **2015**, *385* (9979), 1729–1737.

(8) Nicholson, K.; Aoki, F.; Osterhaus, A.; Trottier, S.; Carewicz, O.; Mercier, C.; Rode, A.; Kinnersley, N.; Ward, P. Efficacy and Safety of Oseltamivir in Treatment of Acute Influenza: A Randomised Controlled Trial. *Lancet* **2000**, *355* (9218), 1845–1850.

(9) Welliver, R. Effectiveness of Oseltamivir in Preventing Influenza in Household ContactsA Randomized Controlled Trial. *JAMA* **2001**, *285* (6), 748.

(10) Hayden, F. G.; Atmar, R. L.; Schilling, M.; Johnson, C.; Poretz, D.; Paar, D.; Huson, L.; Ward, P.; Mills, R. G. Use of the Selective Oral Neuraminidase Inhibitor Oseltamivir to Prevent Influenza. *N. Engl. J. Med.* **1999**, *341* (18), 1336–1343.

(11) Trost, B. M.; Zhang, T. A Concise Synthesis of (−)-Oseltamivir. *Angew. Chem. Int. Ed.* **2008**, *47* (20), 3759–3761.

(12) Satoh, N.; Akiba, T.; Yokoshima, S.; Fukuyama, T. A Practical Synthesis of (-)-

Oseltamivir. *Angew. Chem. Int. Ed.* **2007**, *46* (30), 5734–5736.

(13) Ghosh, S.; Chisti, Y.; Banerjee, U. C. Production of Shikimic Acid. *Biotechnol. Adv.* **2012**, *30* (6), 1425–1431.

(14) Krämer, M.; Bongaerts, J.; Bovenberg, R.; Kremer, S.; Müller, U.; Orf, S.; Wubbolts, M.; Raeven, L. Metabolic Engineering for Microbial Production of Shikimic Acid. *Metab. Eng.* **2003**, *5* (4), 277–283.

(15) Draths, K. M.; Knop, D. R.; Frost, J. W. Shikimic Acid and Quinic Acid: Replacing Isolation from Plant Sources with Recombinant Microbial Biocatalysis. *J. Am. Chem. Soc.* **1999**, *121* (7), 1603–1604.

(16) Candeias, N. R.; Assoah, B.; Simeonov, S. P. Production and Synthetic Modifications of Shikimic Acid. *Chem. Rev.* **2018**, *118* (20), 10458–10550.

(17) Knop, D. R.; Draths, K. M.; Chandran, S. S.; Barker, J. L.; Von Daeniken, R.; Weber, W.; Frost, J. W. Hydroaromatic Equilibration During Biosynthesis of Shikimic Acid. *J. Am. Chem. Soc.* **2001**, *123* (42), 10173–10182.

(18) Patra, J. K.; Das, G.; Bose, S.; Banerjee, S.; Vishnuprasad, C. N.; Del Pilar Rodriguez-Torres, M.; Shin, H. Star Anise (*ILLICIUM VERUM*): Chemical Compounds, Antiviral Properties, and Clinical Relevance. *Phytother. Res.* **2020**, *34* (6), 1248–1267.

(19) Shi, Y.; Chen, G.; Chen, K.; Chen, X.; Hong, Q.; Kan, J. Assessment of Fresh Star Anise (Illicium Verum Hook.f.) Drying Methods for Influencing Drying Characteristics, Color, Flavor, Volatile Oil and Shikimic Acid. *Food Chem.* **2021**, *342*, 128359.

(20) Edmonds, M.; Payne, R. Isolation of Shikimic Acid from Star Aniseed. *J. Chem. Educ.* **2005**, *82* (4), 599.

(21) Cai, M.; Luo, Y.; Chen, J.; Liang, H.; Sun, P. Optimization and Comparison of Ultrasound-Assisted Extraction and Microwave-Assisted Extraction of Shikimic Acid from Chinese Star Anise. *Sep. Purif. Technol.* **2014**, *133*, 375–379.

(22) Fukuta, Y.; Mita, T.; Fukuda, N.; Kanai, M.; Shibasaki, M. De Novo Synthesis of Tamiflu via a Catalytic Asymmetric Ring-Opening of *Meso* -Aziridines with $TMSN_3$. *J. Am. Chem. Soc.* **2006**, *128* (19), 6312–6313.

(23) Kulić, Ž.; Wolff, J.; Wilhelm, E.; Schüler, V.; Röck, B.; Butterer, A. Sourcing Shikimic Acid from Waste Streams of *Ginkgo Biloba* Leaf Extract Production. *ACS Sustainable*

Chem. Eng. **2023**, *11* (13), 4943–4947.

(24) Jia, G.; Zhe, Z.; Hu-ji, Z.; Ye, L.; Liang, Z. Equilibrium, Thermodynamic and Kinetic Studies on Adsorption of Shikimic Acid onto Activated Carbons. *2011 IEEE 3rd International Conference on Communication Software and Networks*; Xi'an, China, **2011**, pp 240–244.

(25) Sui, R. Separation of Shikimic Acid from Pine Needles. *Chem. Eng. Technol.* **2008**, *31* (3), 469–473.

(26) Men, J.; Wang, R.; Li, H.; Li, X.; Yang, S.; Liu, H.; Gao, B. Preparation of Crosslinked Poly (Acryloyloxyethyltrimethyl Ammonium Chloride) Microsphere and Its Adsorption and Mechanism towards Shikimic Acid. *Mater. Sci. Eng. C* **2017**, *71*, 167–175.

(27) Men, J.; Dong, C.; Shi, H.; Hou, B.; Wang, R.; Cui, J.; Wang, L. Methacrylic Acid Functionalized CPS Microspheres to Adsorb Shikimic Acid. *J. Macromol. Sci. Chem. A* **2020**, *57* (1), 25–34.

(28) Hu, P.; Liu, M.; Zhao, J.; Zhang, H.; Wang, Y.; Zhang, M. Integrated Expanded-Bed Ion Exchange Chromatography as a Tool for Direct Recovery of Shikimic Acid from *Illicium Verum*. *Solvent Extr. Ion Exc.* **2014**, *32* (3), 316–332.

(29) Zhang, S.; Gong, X.; Qu, H. A Simple and Effective Method for the Preparation of High-Purity Shikimic Acid from Chromatography Wash Effluent of *Ginkgo Biloba* Leaf Extract by Macroporous Resin Considering the Effect of Varying Feed Solution Compositions. *J. Pharm. Pharmacol.* **2021**, *73* (4), 447–459.

(30) Sarvutiene, J.; Prentice, U.; Ramanavicius, S.; Ramanavicius, A. Molecular Imprinting Technology for Biomedical Applications. *Biotechnol. Adv.* **2024**, *71*, 108318.

(31) Zhang, Y.; Zhao, G.; Han, K.; Sun, D.; Zhou, N.; Song, Z.; Liu, H.; Li, J.; Li, G. Applications of Molecular Imprinting Technology in the Study of Traditional Chinese Medicine. *Molecules* **2022**, *28* (1), 301.

(32) Andersson, L. I. Molecular Imprinting: Developments and Applications in the Analytical Chemistry Field. *J. Chromatogr. B, Biomed. Appl.* **2000**, *745* (1), 3–13.

(33) Jia, M.; Zhang, Z.; Li, J.; Ma, X.; Chen, L.; Yang, X. Molecular Imprinting Technology for Microorganism Analysis. *Trends Anal. Chem.* **2018**, *106*, 190–201.

(34) Nicholls, I. A.; Rosengren, J. P. Molecular Imprinting of Surfaces. *Bioseparation* **2001**,

10 (6), 301–305.

(35) Xu, H.; Schönhoff, M.; Zhang, X. Unconventional Layer-by-Layer Assembly: Surface Molecular Imprinting and Its Applications. *Small* **2012**, *8* (4), 517–523.

(36) Katz, A.; Davis, M. E. Molecular Imprinting of Bulk, Microporous Silica. *Nature* **2000**, *403* (6767), 286–289.

(37) Arabi, M.; Ostovan, A.; Li, J.; Wang, X.; Zhang, Z.; Choo, J.; Chen, L. Molecular Imprinting: Green Perspectives and Strategies. *Adv. Mater.* **2021**, *33* (30), 2100543.

(38) Owens, P. Molecular Imprinting for Bio- and Pharmaceutical Analysis. *Trends Anal. Chem.* **1999**, *18* (3), 146–154.

(39) Byrne, M. E.; Park, K.; Peppas, N. A. Molecular Imprinting within Hydrogels. *Adv. Drug Deliv. Rev.* **2002**, *54* (1), 149–161.

(40) Katata, V. M.; Miyazaki, C. M.; Salvo-Comino, C.; Luz Rodríguez-Méndez, M.; Alessio, P. Molecular Imprinted Lipid Membranes towards the Fabrication of Electrochemical Sensor for Methylene Blue. *Appl. Surf. Sci.* **2025**, *684*, 161887.

(41) Chen, C.; Fang, M.; Sun, Y.; Fan, Y.; Li, K.; Yang, G.; Deng, R.; Li, X. Constructing Labyrinth Structure in Molecularly Imprinted Composite Membranes for Efficiently Separating Acteoside. *Sep. Purif. Technol.* **2025**, *353*, 128569.

(42) Li, S.; Zhou, Y.; Xu, Q.; Chen, H.; Shi, S.; Jia, R.; Zhang, Y.; Ye, H. Preparation of Novel Gallic Acid-Based Dummy-Template Molecularly Imprinted Polymer Adsorbents for Rapid Adsorption of Dibutyl Phthalate from Water. *Environ. Pollut.* **2024**, *349*, 123917.

(43) Wang, W.; Li, H.; Li, M.; Lu, H.; Pan, J. Layer-by-Layer Assembled Magnetic Molecularly Imprinted Nanoparticles for Highly Specific Separation of Adenosine 5′-Monophosphate: Relations between Adsorption Properties and Imprinted Layers. *Sep. Purif. Technol.* **2024**, *330*, 125346.

(44) Xie, D.; Kuang, Y.; Yuan, B.; Zhang, Y.; Ye, C.; Guo, Y.; Qiu, H.; Ren, J.; Alshammari, S. O.; Alshammari, Q. A.; El-Bahy, Z. M.; Zhao, K.; Guo, Z.; Rao, Q.; Yang, S. Convenient and Highly Efficient Adsorption of Diosmetin from Lemon Peel by Magnetic Surface Molecularly Imprinted Polymers. *J. Mater. Sci. Technol.* **2025**, *211*, 159–170.

(45) Xu, W.; Wang, B.; Sun, Y.; Ou, X.; Sun, Y.; Zhang, P.; Chen, Z. Fabrication of Ultrasound/Microwave Co-Assisted Ruthenium Temperature-Sensitive Ion-Imprinted

Polymer Microspheres and Evaluation of Its Selective Adsorption Performances. *Sep. Purif. Technol.* **2025**, *355*, 129652.

(46) Wu, X.; Xia, L.; Luo, Z.; Wu, K.; Lai, J.; Chen, Y.; Xiong, Y. A High Throughput Strategy for Synthesis of Molecularly Imprinted Polymers Microspheres via Oxygen Tolerant Visible Light-Mediated RAFT Polymerization for Sweeteners Sensing in Sucrose. *Eur. Polym. J.* **2025**, *222*, 113628.

(47) Sun, J.; Guo, Y.; Zheng, K.; Zhang, P.; Zhong, X.; Zhou, H.; Zhao, T.; Bao, J. Heat-Resistant Phthalonitrile Resin Composites Self-Toughened via Surface-Reactive Phthalonitrile Microspheres. *Compos. Commun.* **2025**, *53*, 102212.

(48) Merdaw, A. A.; Sharif, A. O.; Derwish, G. A. W. Mass Transfer in Pressure-Driven Membrane Separation Processes, Part II. *Chem. Eng. J.* **2011**, *168* (1), 229–240.

(49) Xin, Y.; Xiong, Q.; Bai, Q.; Miyamoto, M.; Li, C.; Shen, Y.; Uyama, H. A Hierarchically Porous Cellulose Monolith: A Template-Free Fabricated, Morphology-Tunable, and Easily Functionalizable Platform. *Carbohydr. Polym.* **2017**, *157*, 429–437.

(50) Xie, Z.; Asoh, T.; Uyama, H. Monolithic cellulose supported metal nanoparticles as green flow reactor with high catalytic efficiency. *Carbohydr. Polym.* **2019**, *214*, 195–203.

(51) Yang, Z.; Asoh, T.-A.; Uyama, H. Removal of Cationic or Anionic Dyes from Water Using Ion Exchange Cellulose Monoliths as Adsorbents. *Bull. Chem. Soc. Jpn.* **2019**, *92* (9), 1453–1461.

(52) Svec, Frantisek.; Frechet, J. M. J. Continuous Rods of Macroporous Polymer as High-Performance Liquid Chromatography Separation Media. *Anal. Chem.* **1992**, *64* (7), 820–822.

(53) Svec, F.; Fréchet, J. M. J. New Designs of Macroporous Polymers and Supports: From Separation to Biocatalysis. *Science* **1996**, *273* (5272), 205–211.

(54) Zhang, M.; Wei, F.; Zhang, Y.-F.; Nie, J.; Feng, Y.-Q. Novel Polymer Monolith Microextraction Using a Poly(Methacrylic Acid-Ethylene Glycol Dimethacrylate) Monolith and Its Application to Simultaneous Analysis of Several Angiotensin II Receptor Antagonists in Human Urine by Capillary Zone Electrophoresis. *J. Chromatogr. A* **2006**, *1102* (1–2), 294–301.

(55) Béguin, P.; Aubert, J.-P. The Biological Degradation of Cellulose. *FEMS Microbiol. Rev.*

1994, *13* (1), 25–58.

(56) He, J.; Liu, Z.; Ren, L.; Liu, Y.; Dou, P.; Qian, K.; Chen, H.-Y. On-Line Coupling of in-Tube Boronate Affinity Solid Phase Microextraction with High Performance Liquid Chromatography–Electrospray Ionization Tandem Mass Spectrometry for the Determination of Cis-Diol Biomolecules. *Talanta* **2010**, *82* (1), 270–276.

(57) Zhu, Y.; Wang, K.; Lu, J.; Pan, Z.; Rong, J.; Zhang, T.; Yang, D.; Pan, J.; Qiu, F. Teamed Boronate Affinity-Functionalized Zn-MOF/PAN-Derived Molecularly Imprinted Hollow Carbon Electrospinning Nanofibers for Selective Adsorption of Shikimic Acid. *ACS Appl. Mater. Interfaces* **2022**, *14* (23), 27294–27308.

(58) Pan, Z.; Zhu, Y.; Rong, J.; Mao, K.; Yang, D.; Zhang, T.; Pan, J.; Qiu, F. A Recognition Strategy Combining Effective Boron Affinity Technology and Surface Imprinting to Prepare Highly Selective and Easily Recyclable Polymer Membrane for Separation of Drug Molecule. *J. Colloid Interface Sci.* **2022**, *624*, 1–13.

(59) Wang, G.; Zhang, L.; Sugawara, A.; Hsu, Y.-I.; Asoh, T.-A.; Uyama, H. Development of Citric-Acid-Modified Cellulose Monolith for Enriching Glycopeptides. *Anal. Chem.* **2025**, *97* (2), 1125–1134.

(60) Li, X.; Chen, J.; Liu, J.; Yang, K. Silane Modification of Nanofibrillated Cellulose and Its Effect on the Properties of Waterborne Acrylic Resin. *J. Appl. Polym. Sci.* **2023**, *140* (42), e54543.

(61) Brazys, E.; Ratautaite, V.; Mohsenzadeh, E.; Boguzaite, R.; Ramanaviciute, A.; Ramanavicius, A. Formation of Molecularly Imprinted Polymers: Strategies Applied for the Removal of Protein Template (Review). *Adv. Colloid Interface Sci.* **2025**, *337*, 103386.

(62) Pan, Z.; Zhu, Y.; Rong, J.; Mao, K.; Yang, D.; Zhang, T.; Xu, J.; Qiu, F.; Pan, J. FeOOH Imprinted Nanorods Based on Boronate Affinity Surface Imprinting for the Separation of Shikimic Acid. *Colloids Surf. A: Physicochem. Eng. Asp.* **2021**, *622*, 126639.

(63) Yin, H.; Hang, Q.; Xue, T.; Yuan, Y.; Qin, F.; Xiong, Z. A Dual-Recognition Strategy Based on pH-Responsive Molecularly Imprinted Membrane for Highly Selective Capture of Catecholamines: From Construction to Practical Application. *Anal. Chim. Acta* **2024**, *1327*, 343173.

(64) Luo, Z.; Xu, Y.; Tian, M.; Gul, Z.; Qiao, B.; Jia, K.; Li, C.; Zhao, C. An Intelligent

Solvent-Responsive Surface Molecularly Imprinted Membrane with Switchable Adsorption/Desorption Performance for Selective Separation of Psoralen and Recognition Mechanism. *Ind. Crop. Prod.* **2024**, *207*, 117766.

(65) Gouin, X.; Grange, P.; Bois, L.; L'Haridon, P.; Laurent, Y. Characterization of the Nitridation Process of Boric Acid. *J. Alloys Compd.* **1995**, *224* (1), 22–28.

(66) Tom, L. A.; Schneck, N. A.; Walter, C. Improving the Imprinting Effect by Optimizing Template:Monomer:Cross-Linker Ratios in a Molecularly Imprinted Polymer for Sulfadimethoxine. *J. Chromatogr. B* **2012**, *909*, 61–64.

(67) Wu, S.; Chen, W.; Lu, S.; Zhang, H.; Yin, L. Metabolic Engineering of Shikimic Acid Biosynthesis Pathway for the Production of Shikimic Acid and Its Branched Products in Microorganisms: Advances and Prospects. *Molecules* **2022**, *27* (15), 4779.

(68) Singh, P., Arif, Y., Bajguz, A., Hayat, S. The role of quercetin in plants. *Plant Physiol. Biochem.* **2021**, *166*, 10.

(69) Sreeranjini, S.; Siril, E. A. Optimising Elicitors and Precursors to Enhance Alizarin and Purpurin Production in Adventitious Roots of Morinda citrifolia L. *Proc. Natl. Acad. Sci., India, Sect. B Biol. Sci.* **2015**, *85*(3), 725.

(70) Wang, P.; Zhu, H.; Liu, J.; Ma, Y.; Yao, J.; Dai, X.; Pan, J. Double Affinity Integrated MIPs Nanoparticles for Specific Separation of Glycoproteins: A Combination of Synergistic Multiple Bindings and Imprinting Effect. *Chem. Eng. J.* **2019**, *358*, 143–152.

Chapter 3. Hierarchical Titanium Dioxide–Cellulose Monolith for Removing Phosphate Ions from Water

3.1. Introduction

Phosphorus is an essential macronutrient for all living organisms and accounts for approximately 2–4% of cellular dry mass. It is an important structural and functional component of cell membranes and biomolecules, such as nucleic acids and adenosine triphosphate, thus playing a central role in maintaining biological functions.[1–3] In agriculture, phosphate-based fertilizers are widely applied to sustain crop productivity.[4] However, numerous soils have limited phosphate retention capacity, resulting in the significant loss of applied phosphorus through surface runoff.[5] This process reduces fertilizer use efficiency and adversely affects the environment.[6–8] For example, leached phosphate causes eutrophication in freshwater systems that results in excessive algal growth, which is commonly referred to as algal blooms. Such eutrophic conditions often result in oxygen depletion and ecological disruption, thereby threatening aquatic biodiversity and the overall integrity of water ecosystems.[9,10] Globally, regulatory authorities have responded by enforcing stricter discharge limits on phosphorus concentrations in wastewater.[11] Thus, a range of biological, chemical, and physical methods have been developed for phosphate removal from water; however, certain challenges remain in meeting these stricter standards while enabling efficient phosphate recovery and reuse.[12]

Phosphorus removal can be achieved using various chemical methods, including precipitation,[13] flocculation,[14] and adsorption.[15] In particular, adsorption is widely recognized as a promising technique for phosphate removal owing to its high adsorption capacity, cost efficiency, and regenerability. The performance of chemical adsorption depends on the choice of adsorbent materials,[16] such as membranes,[17–19] carbon-based adsorbents,[20,21] magnetic adsorbents,[22,23] metal–organic frameworks,[24,25] and covalent organic frameworks.[26] Although some of these technologies, or their combinations, can achieve low residual phosphorus concentrations, each approach has inherent limitations. These limitations include sensitivity to physicochemical conditions, dependence on membrane systems that are prone to fouling, the generation of poorly recoverable chemical precipitates, and significant space requirements.[27,28] Therefore, advanced adsorbent systems that can reliably capture ultra-low concentrations of phosphorus, sustain high throughput while minimizing membrane fouling, operate under low pressure drops, produce minimal waste, and enable efficient phosphorus recovery are urgently required. Recently, research has primarily focused on designing innovative adsorbent architectures to overcome the limitations of conventional materials while maximizing overall performance.

Monoliths are characterized by their hierarchical, continuous, and porous three-dimensional architecture. They have attracted significant interest owing to their straightforward fabrication and uniform structural integrity.[29–31] Moreover, their adaptable geometries enable seamless integration into diverse systems, particularly in separation processes. Monoliths offer several advantages, including reduced back pressure, enhanced mass transfer kinetics, high adsorption capacities, and simplified manufacturing procedures.[32] Notably, they can be directly implemented in continuous flow adsorption systems, eliminating the need for repetitive centrifugation and other labor-intensive operations to achieve efficient adsorption and desorption.[33] Monoliths comprising environmentally friendly materials, such as cellulose, provide a sustainable and efficient alternative to conventional adsorbents.[34] To achieve high-efficiency phosphate removal, functional materials that exhibit strong phosphate-binding capabilities can be incorporated into monoliths.

Titanium dioxide (TiO_2) is widely explored in the fields of environmental science, materials engineering, and medicine owing to its high surface reactivity, chemical stability, and cost-effectiveness.[35] However, the International Agency for Research on Cancer categorized TiO_2 as a Group 2B substance in 2006 because it is possibly carcinogenic to humans.[36] Phosphate binds strongly to TiO_2 surfaces as a bidentate ligand,[37] and Ronson and McQuillan reported that phosphate preferentially adsorbs at a pH of 6.5.[38,39] Therefore, immobilizing TiO_2 on the surface of porous monoliths could simultaneously achieve efficient adsorption and convenient recovery in water systems.

This study presents the rational design of a hierarchically porous TiO_2-cellulose monolith (CM) as an adsorbent for efficient phosphate removal. As the support material, the CM was derived from a sustainable and renewable carbon source. The TiO_2-CM was fabricated by first preparing a coral-like CM via thermally induced phase separation (TIPS). The CM then served as a scaffold for TiO_2 deposition through a sol–gel reaction with titanium isopropoxide (TTIP).[40] The synthesis conditions were optimized by adjusting the TTIP concentration and CM fabrication parameters to achieve desirable structural properties. Compared to previously reported TiO_2 monoliths, our approach employs a cellulose monolith as a bio-based template and structural scaffold to fabricate hierarchically porous TiO_2 structures with interconnected macro- and mesopores, enhanced mechanical stability, and customizable geometries without the need for template removal. This sustainable and robust fabrication strategy aligns with green chemistry principles and offers significant potential for practical adsorption and separation applications. This approach yielded a highly interconnected porous architecture with a large surface area and low flow resistance, which are essential for continuous flow adsorption. Adsorption behaviors, including pH dependence, kinetics, and isotherms, were evaluated in relation to the structural and interfacial properties of the material. These analyses provided insights into the adsorption mechanism and helped evaluate the potential of TiO_2–CM for selective, rapid, and reusable phosphate removal. The findings contribute to a broader understanding of designing monolithic adsorbent systems to efficiently capture phosphorus under environmentally relevant conditions.

3.2. Experimental Section

3.2.1. Materials

L30 cellulose acetate (CA) was acquired from Daicel Corporation (Tokyo, Japan), and *N,N*-dimethylformamide (DMF) and methanol were obtained from Nacalai Tesque, Inc. (Japan). 1-Hexanol, KH_2PO_4, Na_2SO_4, NaCl, $NaHCO_3$, potassium antimonyl tartrate ($C_8H_{10}K_2O_{15}Sb_2$), ammonium molybdate heptahydrate ($(NH_4)_6Mo_7O_{24}$), and L-ascorbic acid were obtained from Sigma-Aldrich. Sodium hydroxide (NaOH) and hydrochloric acid were sourced from Fujifilm Wako Pure Chemical Industries (Japan). TTIP, NaF, disodium 1-naphthyl phosphate and isopropyl alcohol were purchased from Tokyo Chemical Industry Co., Ltd. (Japan). The deionized water used in this study was produced using a Milli-Q system (Millipore Corp., Milford, MA, USA).

3.2.2. Characterization

Fourier-transform infrared (FT-IR) spectroscopy was performed using a Thermo Scientific Nicolet iS5 spectrometer equipped with an iD5 ATR attachment. All spectra were recorded at a resolution of 4 cm^{-1} across 100 scans in the scan range of 4000–500 cm^{-1}. The morphologies of the monoliths were investigated using scanning electron microscopy (SEM; Hitachi S-3000N) at 15 kV. The pH values were measured using a standard pH electrode (9615-10D) connected to an Horiba LAQUA F-74 analyzer. Elemental compositions of the surfaces were calculated using X-ray photoelectron spectroscopy (XPS; Kratos Ultra 2). The surface area was calculated using the Brunauer–Emmett–Teller (BET) equation based on N_2 adsorption–desorption isotherms (Nova 4200e, Quantachrome Instruments), and samples were vacuum degassed at 60 °C for 24 h prior to obtaining measurements. The pore diameter distribution and volume were calculated using density functional theory. For XPS, monochromatic Al Kα radiation was used with power settings of 75 W (wide) and 150 W (narrow). The survey and high-resolution XPS spectra were collected at fixed analyzer pass energies of 160 and 10 eV, respectively. To confirm reproducibility, measurements were obtained thrice for each sample. The peaks were fitted using CasaXPS Version 2.3.15 (Casa Software, Ltd., Japan). The surface elemental compositions of the monoliths were analyzed using energy-dispersive X-ray (EDX) spectroscopy (Hitachi, Miniscope TM 3000 equipped with Swift ED 3000). Powder X-ray diffraction (XRD) patterns were obtained using a SmartLab system (Rigaku Corporation, Japan) with a Cu Kβ X-ray source and scanning speed of 5° min^{-1} over a 2θ range of 5–80°. The generator voltage and current were 45 kV and 200 mA, respectively. The permeability of the monolithic column was calculated using Darcy's law according to Eq. (3-1):

$$B_0 = F\eta L/(\pi r^2 \Delta P) \tag{3-1}$$

where F (m^3 s^{-1}) denotes the flow rate of the mobile phase, η (Pa s) is the viscosity of the mobile phase (2.98×10^{-3} Pa s for water), L (m) and r (m) represent the effective length and radius of the monolith, respectively, and ΔP (Pa) is the pressure drop across the monolith. For this measurement, the monoliths were tightly fitted with heat-shrink tubing and connected to a digital quantitative tubing pump (As One, DSP-100SA) to control the flow rate (0.2–2.0 mL min^{-1}). In addition, a digital pressure gauge (Krone, KDM30) was used to monitor the pressure drop. The continuous flow system was operated using a peristaltic pump (Eyela, MP-

1000), and the concentration of KH_2PO_4 was measured using a UV-Visible (UV-Vis) spectrophotometer (Hitachi, U-2810).

3.2.3. Fabrication of the CM

The CA monolith (CAM) was fabricated using the TIPS method. Initially, 2.0, 2.5, and 3.0 g of CA powder were individually dissolved in 10 mL of DMF at 90 °C with continuous stirring until each mixture became clear and transparent. Subsequently, 15 mL of 1-hexanol was incrementally added to each dispersion in three separate 5 mL additions with continuous stirring. The resulting CA dispersion was transferred to a glass tube, where it remained undisturbed overnight at 25 °C to enable phase separation. The CAM was formed after several cycles of solvent exchange with methanol at 25 °C, followed by drying. For its conversion to CM, the CAM underwent deacetylation following immersion in a 0.2 mol L^{-1} NaOH/methanol solution. To remove unreacted NaOH residual from the monolith surface and within the monolith, the nascent CM was thoroughly rinsed with deionized water until a neutral pH (approximately 7.0) was attained. The final stage involved drying the sample under vacuum to remove remaining water, yielding the CM.

3.2.4. Preparation of the TiO_2-CM

The TiO_2-CM was prepared using a sol–gel reaction in the presence of the CM. Briefly, TTIP was added to isopropyl alcohol and stirred for 20 min. The CM (0.50 g) was then immersed in the TTIP/isopropyl alcohol solution, and deionized water was added under vigorous stirring. The volume ratio of isopropyl alcohol-to-water was 1:10. The solution was subsequently heated to 80 °C for 5 h and cooled to room temperature. The resulting TiO_2x-CMy (x refers to the content of TTIP (%) and y refers to the concentration of CA (mg mL^{-1})) was washed with distilled water and dried at 80 °C. The total volume of the solution after adding distilled water was 15 mL. The TTIP content is defined as the ratio of the TTIP volume to the total volume of the solution.

3.2.5. Adsorption Experiments

The adsorption capacities of the TiO_2-CM were evaluated using a continuous flow system. The monoliths were precisely encased in a polytetrafluoroethylene heat-shrinkable tube to construct a flow system, with approximately 0.03 g per operation. The reservoir was filled with different concentrations of KH_2PO_4 or disodium 1-naphthyl phosphate solutions (20 mL), which were circulated using a peristaltic pump at a flow rate of 3 mL min^{-1}. Following flow through the monolith, the KH_2PO_4 solution was recycled back into the reservoir at room temperature. After 1 h of adsorption, the final concentrations of PO_4^{3-} under different pH values were measured via UV-Vis spectrophotometry at 880 nm using the Molybdenum blue method.[41–43] The binding amounts were calculated using Eq. (3-2):

$$Q_e = \frac{(C_0 - C_e)V}{m} \tag{3-2}$$

where C_0 and C_e (mg L^{-1}) denote the initial and equilibrium concentrations of PO_4^{3-}, respectively, and Q_e (mg g^{-1}) represents the amount of PO_4^{3-}. The values for V (L) and m (g) correspond to the volume of the KH_2PO_4 solution and mass of the monoliths, respectively.

The binding capacity of the monoliths were systematically evaluated using kinetics and isothermal static adsorption experiments. For the kinetics study, approximately 0.03 g of the monolith was exposed to a continuous flow of KH_2PO_4 solution (100 mg L^{-1}, 20 mL, pH = 6) at 298 K, and sampling was conducted at predetermined intervals from 0 to 60 min. The residual concentration of PO_4^{3-} was determined using UV-Vis spectrophotometry. All experiments were performed in triplicate to ensure reproducibility. The adsorption kinetics were analyzed by fitting the experimental data to pseudo-first- and pseudo-second-order models. The corresponding linearized equations are provided as Eq. S1 and S2 (Supporting Information). For the adsorption isotherm study, a similar procedure was conducted. Approximately 0.03 g of the monolith was exposed to a continuous flow of KH_2PO_4 solution (20 mL, pH = 6) at various initial concentrations (20, 40, 60, 80, and 100 mg L^{-1}) for 60 min at 298 K. These experiments were also conducted in triplicate. The adsorption capacities at different KH_2PO_4 concentrations were calculated, and the data were fitted to the Langmuir and Freundlich isotherm models. The corresponding equations are presented as Eq. S3 and S4 (Supporting Information).

The impact of coexisting anions with TiO_2-CM for PO_4^{3-} adsorption was evaluated using five common anions, including Cl^-, SO_4^{2-}, HCO_3^-, and F^-. The TiO_2-CM was passed through a continuous flow of 20 mL of the interferent solution at varying concentration ratios and continuous adsorption using the peristaltic pump for 1 h. In the competitive experiments, the coexisting substances included NaCl, Na_2SO_4, $NaHCO_3$ and NaF, and the molar concentration ratios of substance-to-phosphate were 1:1, 5:1, and 10:1. Concentrations of the various interferents in the supernatant were measured using UV-Vis spectrophotometry.

3.2.6. Regeneration Tests

The reusability of adsorbents serves as a critical parameter for assessing their adsorption performance. Thus, TiO_2-CM reusability was examined using a series of adsorption–desorption experiments. Briefly, the TiO_2-CM was introduced into a solution containing 20 mL of KH_2PO_4 (100 mg L^{-1}) and processed through a continuous flow system at room temperature for 1 h. The resulting KH_2PO_4 concentration in the supernatant was determined using UV-Vis spectrophotometry. An eluent comprising an $NaHCO_3$–NaOH buffer solution (pH = 10.0) was used in the subsequent cycle to ensure a constant pH during the elution process. The adsorbed TiO_2-CM was first rinsed with the eluent until no detectable KH_2PO_4 remained, followed by washing with water and drying. This adsorption–desorption process was repeated five times, and the corresponding adsorption capacity was calculated. The entire procedure was performed at least thrice to ensure reproducibility.

3.2.7. Steps for determining phosphate ion concentration via molybdenum blue method

To prepare the molybdenum blue reagent, 10 mL of 2.5 M H_2SO_4 is mixed with 1 mL of 4 mM potassium antimonyl tartrate ($C_8H_{10}K_2O_{15}Sb_2$) for 45 s. Then, 3 mL of 0.1 M ammonium molybdate heptahydrate ($(NH_4)_6Mo_7O_{24}$) is added, followed by 6 mL of 0.1 M L-ascorbic acid. The resulting molybdenum blue solution is stored at room temperature and remains stable for up to 4 h. For sample analysis, 2 μL of the phosphate solution is added to 198 μL of water to attain 100-fold dilution, followed by 32 μL of the molybdenum blue reagent in a 96-well plate. After 20 min, the phosphate ion concentration in the sample is determined using UV–Vis spectrophotometry at 880 nm.

3.2.8. Rebinding kinetics and adsorption isotherm

The kinetic data of TiO_2-CM were analyzed using pseudo-first-order and pseudo-second-order models, and the corresponding equations presented as Eqs. 3-3 and 3-4, respectively.

$$Q_t = Q_e - Q_e e^{-k_1 t} \tag{3-3}$$

where k_1 (min^{-1}) is the rate constant of the pseudo-first adsorption. Q_e and Q_t (mg g^{-1})

represent the adsorption capacities at equilibrium and time t (min), respectively. The rate constants k_1, Q_e, and correlation coefficients R^2 were calculated from the slope and intercept of the linear plot of ln ($Q_e - Q_t$) versus t.

$$Q_t = \frac{k_2 Q_e^2 t}{1 + k_2 Q_e t} \tag{3-4}$$

where k_2 (mg g^{-1} min^{-1}) is the rate constant of the pseudo-second order equation. The parameters k_2 and Q_e, and the correlation coefficients R^2 are calculated from the linear plots of t/Q_t versus t.

The experimental adsorption data were investigated using the Langmuir and Freundlich models, represented by Eqs. 3-5 and 3-6, respectively.

$$\frac{C_e}{Q_e} = \frac{1}{Q_m} C_e + \frac{1}{K_a Q_m} \tag{3-5}$$

$$\log Q_e = \log K_f + \frac{1}{n} \log C \tag{3-6}$$

where Q_e (mg g^{-1}) is the adsorption capacity at equilibrium, and C_e (mg L^{-1}) is the equilibrium concentration of PO_4^{3-}. In the Freundlich model, K_f (L mg^{-1}) is the adsorption capacity constant, and n is the heterogeneity factor. In the Langmuir model, K_a (L mg^{-1}) is the adsorption equilibrium constant, and Q_m (mg g^{-1}) is the maximum monolayer adsorption capacity. The Freundlich model assumes a heterogeneous surface with multilayer adsorption, while the Langmuir model assumes monolayer adsorption on a homogeneous surface with uniform energy sites.

3.3. Results and discussion

3.3.1. Optimization of TiO_2-CM Fabrication

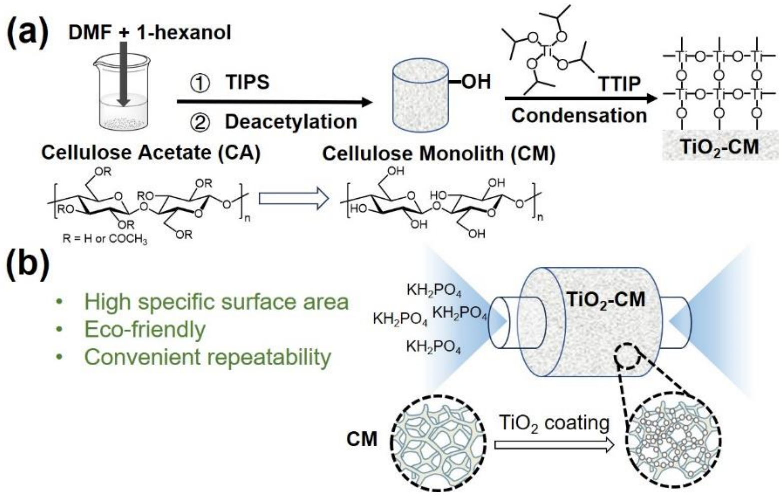

Fig. 3-1. (a) Preparation of the TiO_2-CM absorbent. (b) Schematic illustration of adsorption of phosphate ions using TiO_2-CM.

To develop a sustainable and high-performance phosphate adsorbent, a composite monolith, which featured a hierarchically porous cellulose scaffold integrated with a TiO_2 layer deposited on its surface, was fabricated. **Fig. 3-1a** presents a schematic representation of the preparation process for the TiO_2-CM. The hierarchically porous CM was first synthesized using the TIPS method, as described in a previous study.[32] TiO_2 was subsequently incorporated into this porous supporting structure using a sol–gel process, which was initiated when TTIP readily underwent hydrolysis in the presence of water. During this process, a condensation reaction occurred between the hydroxyl groups on the cellulose surface and hydrolyzed Ti species, facilitating the formation of covalent Ti–O–C bonds. Thus, with its abundant surface hydroxyl groups, cellulose served as an effective substrate for surface sol–gel modification. Furthermore, the diffusion and distribution of TiO_2 oligomers and nanoparticles into the cellulosic matrix enhanced the TiO_2-CM structure.[40] The resulting TiO_2-CM featured a coral-like structure and granular morphology, guided by sol–gel processing on the cellulose scaffold. For the {101} facets of anatase TiO_2, bidentate coordination[44,45] is often identified as the most thermodynamically favorable configuration, suggesting that phosphate predominantly adsorbed in a bidentate mode on this surface (**Fig. 3-1**).[37,46] Table S1 summarizes the synthesis of CM samples resulting from different concentrations of CA. Various concentrations of TTIP were also employed for surface modification, with specific concentrations and corresponding sample names presented in **Table 3-1**. When the TTIP content was sufficiently high, the macropore diameter decreased due to increased TiO_2 deposition on the skeleton surface of the monolith. This effect was reflected in the permeability measurements, which were conducted under flow conditions. As illustrated in **Fig. 3-2**, the permeability coefficient B_0 varied as a function of TTIP content and CM pore size. A higher TTIP content, coupled with an increased CA concentration, reduced the B_0 value in the resulting TiO_2 monolith.

Table 3-1. Synthesis conditions of TiO_2-CM for different TTIP content.

Sample	TTIP (mL)	Isopropyl alcohol (mL)	H_2O (mL)
$TiO_2$40-CM80	6	0.82	8.2
$TiO_2$60-CM80	9	0.55	5.5
$TiO_2$40-CM100	6	0.82	8.2
$TiO_2$60-CM100	9	0.55	5.5
$TiO_2$40-CM120	6	0.82	8.2
$TiO_2$60-CM120	9	0.55	5.5

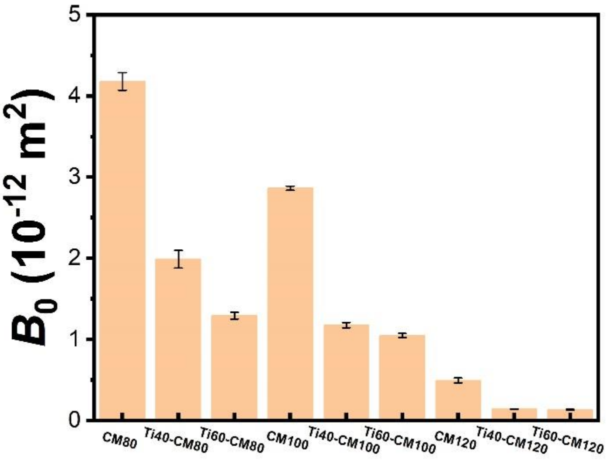

Fig. 3-2. The permeability of each CM and TiO_2-CM.

It is hypothesized that introducing a TiO$_2$ layer onto the surface of the CM material would enhance the surface area of the resulting TiO$_2$-CM. To confirm this hypothesis, N$_2$ adsorption–desorption experiments were conducted to determine the pore size distributions and BET surface areas of the materials (**Fig. 3-3** and **Fig. 3-4**). The N$_2$ adsorption–desorption isotherms revealed that the surface area of CM80 was 4.66 m^2 g^{-1}. Following TiO$_2$ deposition, a significant increase in surface area was observed, with TiO$_2$60-CM80 and TiO$_2$40-CM80 exhibiting specific surface areas of 94.2 and 36.4 m^2 g^{-1}, respectively. Moreover, the specific surface areas of CM100, TiO$_2$60-CM100, and TiO$_2$40-CM100 were 6.83, 19.0, and 21.6 m^2 g^{-1}, respectively. Therefore, TiO$_2$ modification enhanced the specific surface area of the monolith, providing more adsorption-active sites. The permeability data revealed that TiO$_2$60-CM80 exhibited higher permeability than did TiO$_2$60-CM100. This result generally indicates a larger pore size or improved pore connectivity. However, the BET results showed that TiO$_2$60-CM80 possessed a greater specific surface area than TiO$_2$60-CM100. This discrepancy can be attributed to differences in the initial pore structures of CM80 and CM100. Owing to the larger pore size of CM80, TiO$_2$ deposition predominantly occurred along the pore walls, thus increasing the specific surface area. In contrast, the relatively smaller pores of CM100 may have been partially filled by TiO$_2$, thereby reducing its specific surface area. Notably, BET analysis primarily accounts for micropores (<2 nm) and mesopores (2–50 nm), while permeability is primarily influenced by macropores (>50 nm). The high specific surface area of TiO$_2$60-CM80 suggests the presence of numerous micropores and mesopores, and its retained macropores contributed to its high permeability. Effective adsorption is required in a continuous flow system; therefore,

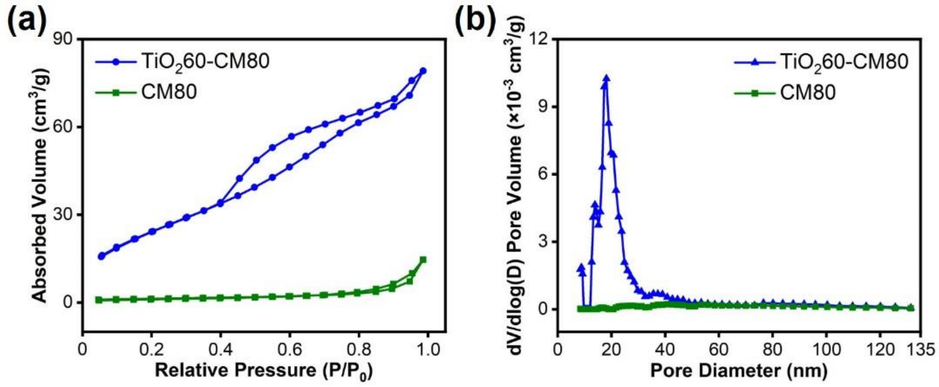

Fig. 3-3. (a) N$_2$ adsorption–desorption curves and (b) corresponding pore size distributions of TiO$_2$60-CM80 and CM80.

$TiO_2$60-CM80 was selected for subsequent experiments owing to its largest specific surface area and superior permeability.

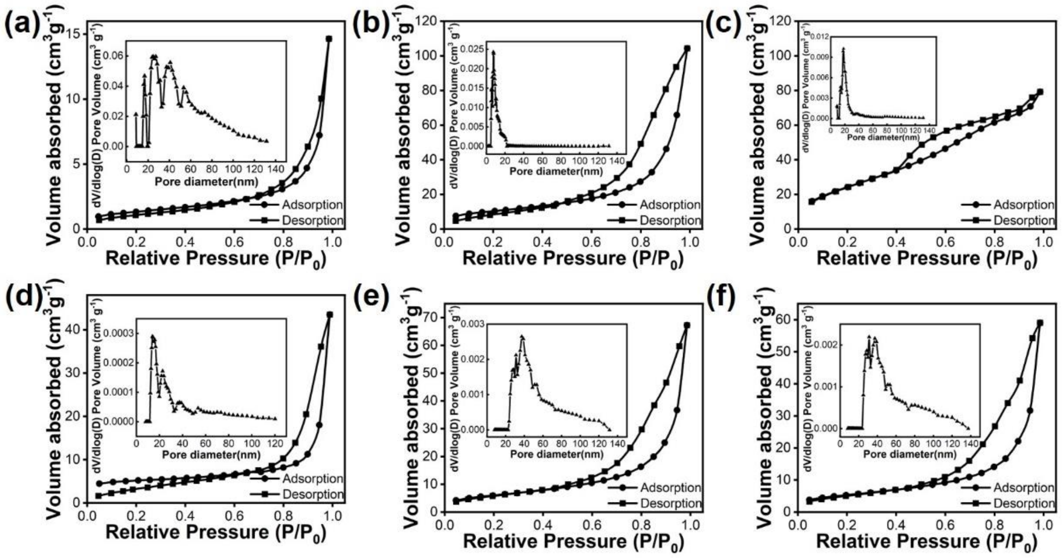

Fig. 3-4. N_2 adsorption/desorption isotherms of (a) CM80, (b) $TiO_2$40-CM80, (c) $TiO_2$60-CM80, (d) CM100, (e) $TiO_2$40-CM100, and (f) $TiO_2$60-CM100. The corresponding pore size distributions are presented in the insets

3.3.2. Characterization of the TiO_2-CM

The chemical component of the monolith was investigated using FT-IR, XRD, and XPS analyses. As shown in **Fig. 3-5a**, the FT-IR spectrum of the CM displays characteristic bands at 1023 and approximately 3400 cm^{-1}, which are attributed to C–O–C and –OH stretching vibrations, respectively. Following sol–gel processing, the TiO_2-CM exhibited new absorption bands in the range of 500–800 cm^{-1}, as well as bands at 1023 and 1632 cm^{-1}, corresponding to Ti–O–Ti, C–O–C, C–O–Ti, and Ti–O–Ti bonds. Thus, TiO_2 was successfully anchored to the CM via condensation reactions between cellulose and TTIP. The XRD patterns of CM, TiO_2-CM, and the TiO_2 powder are shown in **Fig. 3-5b**. The CM exhibited a prominent diffraction peak at approximately $2\theta = 20°$, corresponding to the (002) plane of crystalline cellulose. In contrast, the diffraction peaks at (101), (112), (200), (105), (211), (204), (116), (220), (215), and (303) are characteristic of the anatase phase of TiO_2. Notably, both the CM and TiO_2 signals were present in the XRD pattern of the TiO_2-CM, confirming that TiO_2 was successfully deposited onto the CM surface via the sol–gel process. To further confirm the elemental composition of the TiO_2-CM, both the CM and TiO_2-CM were analyzed using XPS. In the XPS

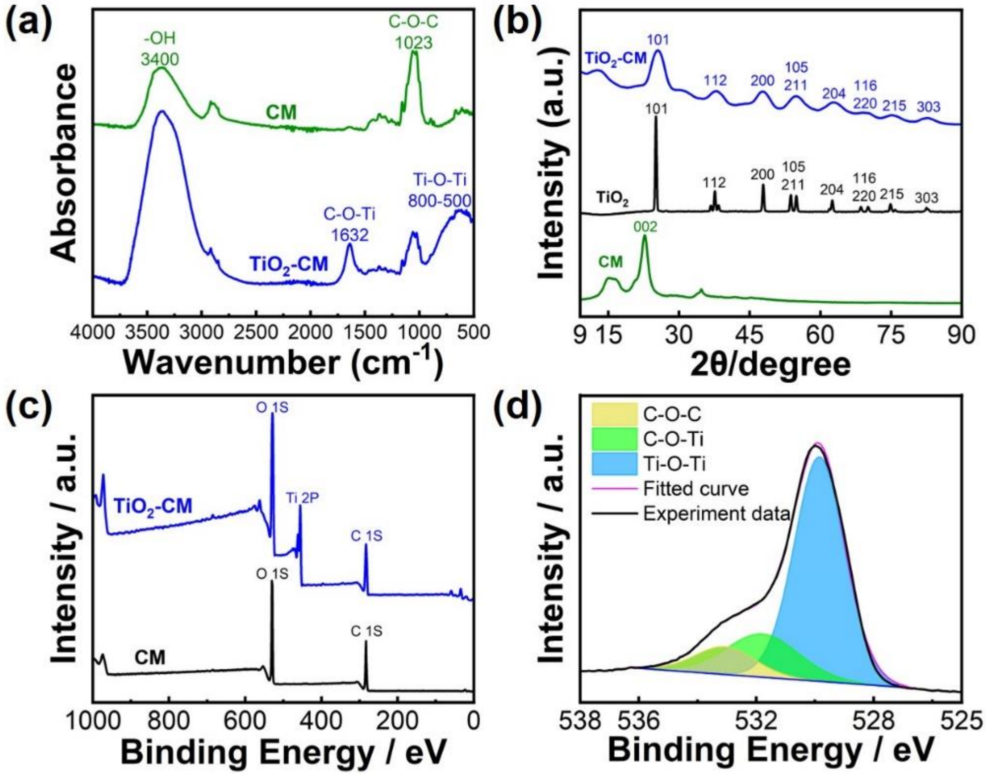

Fig. 3-5. (a) FT-IR spectra, (b) XRD patterns, and (c) survey XPS spectra of the TiO$_2$-CM and CM. (d) High-resolution O 1s XPS spectra of the TiO$_2$-CM.

spectrum of the CM, only carbon and oxygen signals were detected (**Fig. 3-5c**). In contrast, the XPS spectrum of the TiO$_2$-CM showed a distinct peak corresponding to Ti, indicating its successful incorporation. Moreover, the high-resolution O 1s XPS spectrum of the TiO$_2$-CM (**Fig. 3-5d**) revealed the presence of Ti–O–C bonds. The peaks observed at 530.0, 531.7, and 533.1 eV were assigned to the Ti–O–Ti, Ti–O–C, and C–O–C bonds, respectively. The high-resolution Ti 2p XPS spectrum (**Fig. 3-6**) showed characteristic peaks of Ti 2p$_{3/2}$ and Ti 2p$_{1/2}$ at 458.4 and 464.3 eV, respectively. Thus, a substantial amount of TiO$_2$ was successfully coated onto the surface of the TiO$_2$-CM.

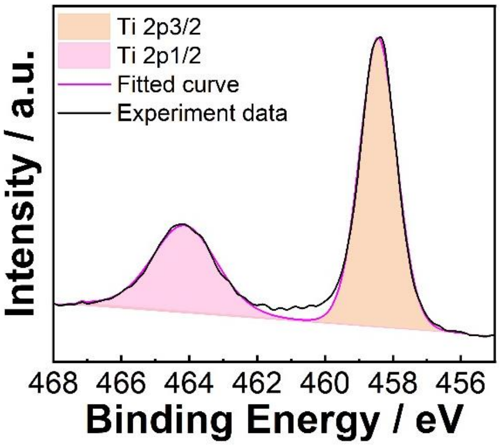

Fig. 3-6. High-resolution XPS spectra of Ti 2p of TiO$_2$-CM.

To determine the structure of the TiO$_2$ layer, the pore morphologies of the CM and TiO$_2$-CM were examined using SEM. As shown in **Fig. 3-7a,b**, the CM material exhibited a dendritic skeletal structure with a wrinkled surface resembling that of coral that was observable under high magnification. **Fig. 3-7c,d** shows that the coral-like structure of the CM material was retained following the uniform coating of TiO_2, resulting in the TiO_2-CM. Notably, the biomimetic coral-like structure of the TiO_2-CM facilitated mass transfer between the material and solution while effectively reducing steric hindrance, thus promoting efficient continuous flow adsorption. SEM-EDX was conducted to investigate the distribution of Ti on the TiO_2-CM surface. As illustrated in Fig. S4, the C, O, and Ti atoms distributed on the TiO_2-CM surface were consistent and homogeneous, confirming that TiO_2 was uniformly coated on the CM material. These results were consistent with the SEM observations.

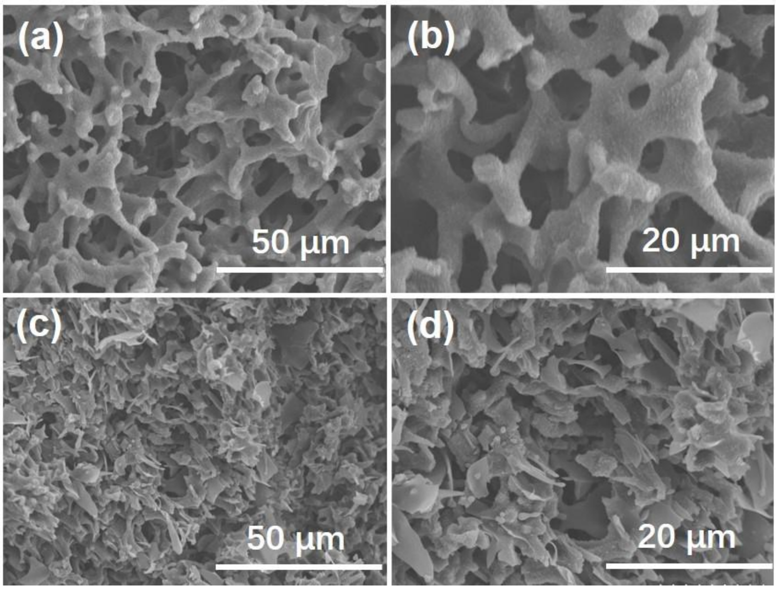

Fig. 3-7. SEM images of the (a, b) CM and (c, d) TiO_2-

3.3.3. Adsorption Kinetics and Isotherm Models

The binding affinity between phosphorus and TiO_2 is highly dependent on the pH. To evaluate this effect, the influence of solution pH (ranging from 2.0 to 9.0) on the adsorption behavior of TiO_2-CM was investigated. As shown in **Fig. 3-8a**, the adsorption capacity decreased with increasing pH above 7, with the highest binding observed at a pH of 6.0.[38,39] Notably, the adsorption capacity remained high at pH <7, suggesting that electrostatic interactions have a limited role in phosphate adsorption under these conditions. Thus, the TiO_2-CM exhibited excellent phosphate removal performance over a broad pH range (2–7), rendering it particularly suitable for applications in acidic to neutral water treatment processes. Moreover, this characteristic enhances its practicality for real-world applications under typical environmental pH conditions. Based on these findings, a pH of 6.0 was selected as the optimal condition for subsequent experiments.

The adsorption capacity of the CM toward phosphorus exhibited minimal variations across a pH range of 2–9, indicating that the process was primarily governed by non-specific physical interactions. Notably, the CM lacks active sites for chemical complexation or electrostatic attraction with phosphate ions. Moreover, its surface hydroxyl groups exhibit minor changes in charge with pH, and under alkaline conditions, electrostatic repulsion occurs between the negatively charged CM surface and phosphorus. This results in consistently low and pH-insensitive adsorption performance. Variations in phosphate sorption behavior may be attributed to the pH-dependent speciation of phosphate in aqueous solutions. For example, as the pH changes, the protonation states of phosphate species shift, resulting in distinct sorption mechanisms at the TiO_2 surface.[47] Additionally, the surface charge of TiO_2 itself is influenced by pH. With increasing pH, surface protonation decreases, resulting in a more negatively charged surface that affects phosphate binding.[48,49]A distinct peak corresponding to P 2p indicated the successful binding of phosphate to the TiO_2-CM surface, thereby supporting the proposed adsorption mechanism illustrated in **Fig. 3-1**.

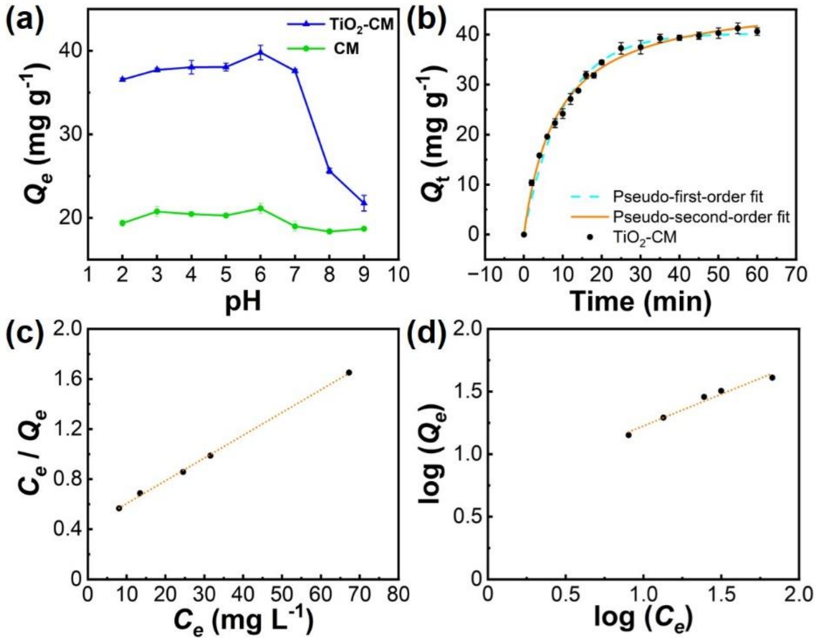

Fig. 3-8. (a) Effect of solution pH on the adsorption amount of the CM and TiO_2-CM. (b) Adsorption kinetics study of the TiO_2-CM. (c) Langmuir and (d) Freundlich isotherms of the TiO_2-CM.

To investigate the effect of flow rate on adsorption performance, adsorption experiments were conducted using $TiO_2$60-CM100 at different flow rates for 30 minutes. The adsorption capacity was found to be 31.0 ± 5.3 mg g^{-1} at 4 mL min^{-1} and 29.5 ± 4.9 mg g^{-1} at 2 mL min^{-1}, indicating that variations in flow rate had a limited influence on the adsorption capacity itself. In contrast, $TiO_2$60-CM80 demonstrated a higher capacity of 37.5 ± 1.3 mg g^{-1} under the flow rate conditions of 3 mL min^{-1}, which was employed as the standard flow rate in these experiments. These results suggest that the porous structure and permeability of the cellulose monolith have a more pronounced impact on TiO_2 incorporation efficiency and overall adsorption performance than the flow rate. The greater number of macropores and higher permeability in CM80 facilitate more effective TiO_2 deposition, which is consistent with its higher specific surface area as determined by BET analysis.

To better understand the phosphorus adsorption behavior of the TiO_2-CM adsorbent, detailed analyses of the adsorption kinetics and isotherms were conducted. As illustrated in **Fig. 3-8b**, kinetic experiments were performed using an initial KH_2PO_4 concentration of 100 mg L^{-1}, focusing on the time-dependent evolution of adsorption capacity. The adsorption tests were conducted at a pH and temperature of 6.0 and 298 K, respectively. TiO_2-CM was immersed in the phosphate solution for 1 h, and samples were collected at regular intervals to monitor the changes in concentration. The adsorption capacities at different times (Q_t) were calculated using Eq. (3-2). The resulting kinetic curves are shown in **Fig. 3-8b**. The TiO_2-CM demonstrated a time-dependent increase in phosphate uptake, reaching equilibrium within approximately 1 h. A sharp increase in adsorption was observed during the initial 20 min, accounting for >95% of the total capacity, followed by a gradual plateau as the phosphate concentration in the solution decreased. The maximum adsorption capacity was 40.6 mg g^{-1} following 60 min of contact time.

Table 3-2. Kinetic model parameters obtained in the adsorption of PO_4^{3-} onto the TiO_2-CM.[a]

Sample	[b] $Q_{e,e}$	Pseudo-first-order equation			Pseudo-second-order equation		
	(mg g^{-1})	[c] $Q_{e,c}$ (mg g^{-1})	k_1 (min^{-1})	R^2	$Q_{e,c}$ (mg g^{-1})	k_2 (g mg^{-1} min^{-1})	R^2
TiO_2-CM	40.6	40.2	0.099	0.987	47.7	2.5×10^{-3}	0.991

[a] Testing conditions: pH = 6.0, C_0 = 100 mg L^{-1}, and T = 298 K.

[b] $Q_{e,e}$ (mg g^{-1}) is the experimental data of equilibrium rebinding amount.

[c] $Q_{e,c}$ (mg g^{-1}) is the calculated data of equilibrium rebinding amount.

To further analyze the adsorption mechanism, the kinetics data were fitted to pseudo-first- and pseudo-second-order models (Eq. 3-3 and 3-4), and the derived parameters are listed in **Table 3-2**. The pseudo-second-order model exhibited a slightly higher correlation coefficient (R^2 = 0.991) than the pseudo-first-order model (R^2 = 0.987). Thus, the adsorption process may have involved chemisorption mechanisms such as surface complexation. However, the equilibrium capacity predicted using the pseudo-first-order model (40.2 mg g^{-1}) was more consistent with the experimental value (40.6 mg g^{-1}) than that using the pseudo-second-order model (47.7 mg g^{-1}). While chemisorption may have contributed to the overall kinetics, with phosphate ions forming bidentate complexes through either chelating a single titanium center or bridging between two titanium atoms, the adsorption process was also influenced by physical interactions, such as electrostatic interactions or van der Waals forces.

The equilibrium adsorption behavior of the TiO_2-CM toward PO_4^{3-} was systematically evaluated over various initial KH_2PO_4 concentrations. As shown in **Fig. 3-8c,d** and detailed in Table S4, the experimental data were analyzed using both the Langmuir and Freundlich isotherm models (Eq. 3-5 and 3-6). To gain deeper insight into the adsorption mechanism, the fitting performance of each model was compared and summarized (**Table 3-3**). The Langmuir model exhibited a higher correlation coefficient (R^2 = 0.989) than the Freundlich model (R^2 = 0.958). Thus, the adsorption process is better described by monolayer adsorption on a relatively homogeneous surface. The maximum adsorption capacity (Q_m) calculated from the Langmuir model was 55.1 mg g^{-1}, indicating that the TiO_2-CM provided numerous accessible binding sites for phosphate ions. Additionally, the Langmuir affinity constant (K_a = 0.044 L mg^{-1}) reflected a moderate binding strength between phosphate and the TiO_2-CM surface. The Freundlich constant (1/n = 0.505) further indicated that the adsorption process was favorable but not extremely strong. This result is consistent with a physical adsorption mechanism involving electrostatic interactions or van der Waals forces.

Table 3-3. Adsorption isotherm constants obtained in the adsorption of PO_4^{3-} onto the TiO_2-CM.[a]

Sample	Langmuir model			Freundlich model		
	Q_m (mg g^{-1})	K_a (L mg^{-1})	R^2	K_f (mg L^{-1})	1/n	R^2
TiO_2-CM	55.1±5.2	0.044±0.009	0.989±0.008	5.36±0.92	0.505±0.056	0.958±0.024

[a] Testing conditions: pH = 6.0, adsorption time = 60 min, and T = 298 K.

Thus, phosphate was predominantly adsorbed via monolayer coverage on surface sites that were relatively uniform; however, some degree of surface heterogeneity cannot be ruled out. The good fit of the Langmuir model and the moderately high K_a value underscore the potential of the TiO_2-CM as an effective and practical phosphate adsorbent under equilibrium conditions.

To further evaluate the applicability of TiO_2-CM for phosphorus recovery beyond inorganic phosphate ions, adsorption experiments were conducted using disodium 1-naphthyl phosphate, a representative organic phosphorus compound (**Fig. 3-9**). TiO_2-CM exhibited an adsorption capacity of 7.7 mg g^{-1} from its aqueous solution at an initial concentration of 100 mg L^{-1} under identical experimental conditions. Moreover, the adsorption capacity was 2.1 mg g^{-1} at an initial concentration of 20 mg L^{-1}. Notably, after adjusting the pH of the solution to 6.0 using HCl, the adsorption capacity at an initial concentration of 100 mg L^{-1} increased to 9.6 mg g^{-1}. These results demonstrate that TiO_2-CM is capable of adsorbing both inorganic and organic phosphorus compounds, and that adsorption efficiency can be enhanced by pH adjustment, indicating promising potential for broader phosphorus resource recovery applications.

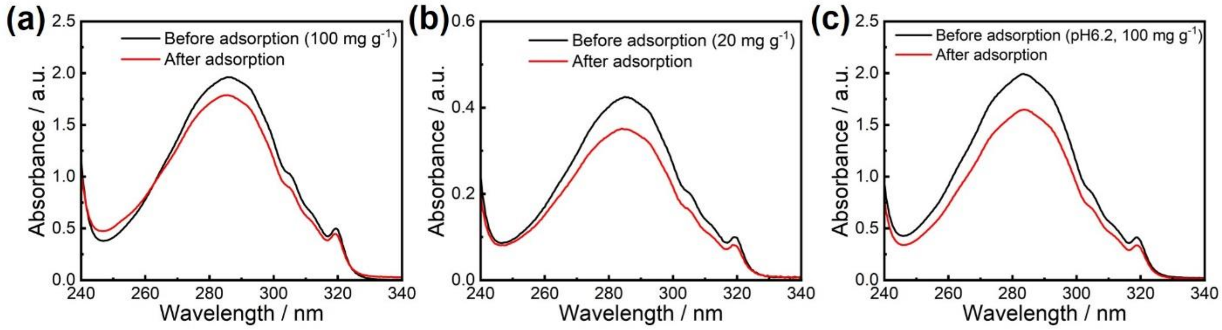

Fig. 3-9. Adsorption results of TiO_2-CM on Disodium 1-naphthyl phosphate at different concentrations, (a) 100 mg L^{-1}, (b) 20 mg L^{-1}, (c) pH 6.2, 100 mg L^{-1}.

3.3.4. Binding Specificity and Reusability

The presence of coexisting anions may interfere with phosphate adsorption by competing for active sites on the TiO_2-CM surface, thereby diminishing its removal efficiency. To evaluate this potential interference, four commonly encountered anions (Cl^-, SO_4^{2-}, HCO_3^-, and F^-) were systematically investigated.[50] As illustrated in **Fig. 3-10a**, Cl^- and SO_4^{2-} exhibited negligible influences on phosphate adsorption. Moreover, the adsorption capacity remained >30 mg g^{-1}

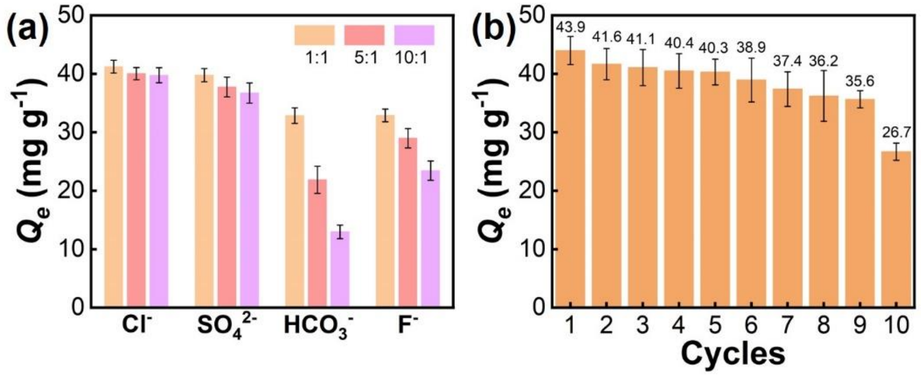

Fig. 3-10. (a) Phosphate adsorption capacity of the TiO_2-CM in the presence of competing anions, which were added as sodium salts. (b) Reusability of the TiO_2-CM over 10 consecutive adsorption–desorption cycles.

even at a 10:1 molar ratio relative to phosphate. Similarly, low concentrations of HCO_3^- and F^- had a limited impact; however, when their concentrations were increased to 7.3 mM (corresponding to a 10:1 molar ratio), phosphate adsorption decreased from 40.6 to 12.9 and 23.4 mg g^{-1} for HCO_3^- and F^-, respectively. The reduced adsorption in the presence of HCO_3^- was partially due to a pH increase to 8.9, which is unfavorable for phosphate uptake (**Fig. 3-8a**). At high pH values, the TiO_2 surface became more negatively charged, resulting in electrostatic repulsion with phosphate species. Moreover, the high electronegativity and strong affinity for the protonated TiO_2 surface by F^- likely resulted in competitive adsorption at the active sites.[51,52]

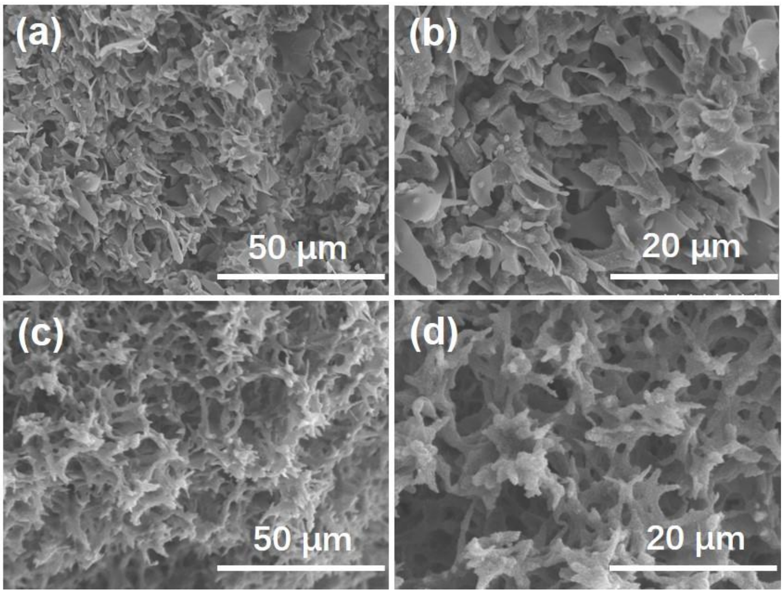

Fig. 3-11. SEM images of the TiO_2-CM (a, b) before adsorption and (c, d) after 10 adsorption-desorption cycles.

Overall, the TiO_2-CM exhibited excellent selectivity for phosphate in the presence of common anions such as Cl^- and SO_4^{2-}. However, high concentrations of HCO_3^- and F^- significantly impaired phosphate adsorption, primarily due to pH effects and strong competitive interactions. Nevertheless, the TiO_2-CM maintained robust phosphate removal performance under typical environmental conditions.

Beyond achieving high selectivity or specificity in adsorption, the reusability of composite adsorbents is a critical factor for their practical application. As demonstrated in our pH-dependent adsorption study, phosphate uptake by the TiO_2-CM adsorbent was suppressed under alkaline conditions,[53] suggesting that desorption can be effectively triggered at high pH levels ($pH > pH_{pzc}$, the point of zero charge). Therefore, phosphate desorption experiments were performed using TiO_2-CM preloaded with phosphate, with a $NaHCO_3$–NaOH buffer solution at pH 10.0 as the eluent. As shown in **Fig. 3-10b**, the adsorption capacity was relatively well maintained over ten consecutive adsorption–desorption cycles, although it gradually decreased from 43.9 mg g^{-1} in the first cycle to 26.7 mg g^{-1} in the tenth cycle. Despite this decline, over 60% of the initial capacity was retained, demonstrating the material's considerable reusability. SEM analysis revealed that the hierarchical porous structure remained largely intact after repeated use, with only slight compaction and surface smoothing observed (**Fig. 3-11**). The gradual reduction in performance may be attributed to the partial blockage or irreversible binding of active sites during repeated cycling. These results indicate that TiO_2-CM maintains its structural integrity and functional performance under prolonged operational conditions, making it a promising candidate for practical water treatment applications.

The detection sensitivities of different materials can be compared using the data in **Table 3-4**.[54–63] Most significantly, TiO_2-CM has higher adsorption capacity and better recovery efficiency compared to other materials.

Table 3-4. Comparison of the adsorption performances of different materials for Phosphoric acid.

Material	Adsorption capacity of phosphoric acid (mg g^{-1})	Reusability	ref.
TiO_2-CM	40.6	5	This work
ZnO/ZnFe-LDHs alginate hydrogels	17.1	5	54
soil mineral-BDOM complexes	29.7	/	55
M-IACBs	18.5	/	56
BBC	75.3	/	57
MBC	70.3	/	58
COF-MCE	10.5	50	59
OH/NH_2@MBC	43.3	5	60
La-MBC	27.5	/	61
Tb-BTC	111.3	/	62
MOF-808(Zr/Ce)	68.5	/	63

3.4. Conclusions

A hierarchically porous TiO_2-CM was fabricated using the sol–gel method, where TiO_2 was immobilized onto the surface of a CM. The pore structures were modified by adjusting key fabrication parameters, including the type of CM and TTIP content. The porous characteristics of the TiO_2-CM were thoroughly analyzed using SEM and N_2 adsorption–desorption experiments. Incorporating TiO_2 into the CM significantly enhanced its specific surface area owing to its well-developed hierarchically porous morphology. The TiO_2-CM displayed excellent phosphate sequestration efficiency, with phosphate primarily interacting with the TiO_2-CM surface through bidentate coordination. Furthermore, the adsorption isotherms and kinetics data were well-fitted using the Langmuir model and pseudo-second-order kinetics. Thus, phosphate adsorption proceeded via monolayer coverage on a relatively homogeneous surface and was likely driven by a combination of chemisorption and electrostatic interactions. In the presence of competing anions, the TiO_2-CM demonstrated strong selectivity for phosphate while maintaining high adsorption efficiency under environmentally relevant conditions. Moreover, its excellent reusability, with approximately 98% removal efficiency sustained over multiple cycles, underscores its practical applicability for sustainable phosphate recovery and water treatment. These findings highlight the promising potential of the TiO_2-CM for phosphate removal in applications such as environmental pollution control and industrial wastewater treatment.

3.5. References

(1) Karl, D.M. Phosphorus, the staff of life. *Nature* **2000**, *406* (6791), 31–33.

(2) Lambers, H. Phosphorus Acquisition and Utilization in Plants. *Annu. Rev. Plant Biol.* **2022**, *73* (1), 17–42.

(3) Ferrier‐Pagès, C.; Godinot, C.; D'Angelo, C.; Wiedenmann, J.; Grover, R. Phosphorus metabolism of reef organisms with algal symbionts. *Ecol. Monogr.* **2016**, *86* (3), 262–277.

(4) Shen, J.; Yuan, L.; Zhang, J.; Li, H.; Bai, Z.; Chen, X.; Zhang, W.; Zhang, F. Phosphorus Dynamics: From Soil to Plant. *Plant Physiol.* **2011**, *156* (3), 997–1005.

(5) Sattari, S. Z.; Bouwman, A. F.; Giller, K. E.; Van Ittersum, M. K. Residual soil phosphorus as the missing piece in the global phosphorus crisis puzzle. *Proc. Natl. Acad. Sci. U.S.A.* **2012**, *109* (16), 6348–6353.

(6) Jupp, A. R.; Beijer, S.; Narain, G. C.; Schipper, W.; Slootweg, J. C. Phosphorus recovery and recycling – closing the loop. *Chem. Soc. Rev.* **2021**, *50* (1), 87–101.

(7) Conley, D. J.; Paerl, H. W.; Howarth, R. W.; Boesch, D. F.; Seitzinger, S. P.; Havens, K. E.; Lancelot, C.; Likens, G. E. Controlling Eutrophication: Nitrogen and Phosphorus. *Science* **2009**, *323* (5917), 1014–1015.

(8) Schindler, D. W.; Carpenter, S. R.; Chapra, S. C.; Hecky, R. E.; Orihel, D. M. Reducing Phosphorus to Curb Lake Eutrophication is a Success. *Environ. Sci. Technol.* **2016**, *50* (17), 8923–8929.

(9) Ni, Z.; Wang, S.; Cai, J.; Li, H.; Jenkins, A.; Maberly, S. C.; May, L. The potential role of sediment organic phosphorus in algal growth in a low nutrient lake. *Environ. Pollut.* **2019**, *255*, 113235.

(10) Chen, M.; Ding, S.; Chen, X.; Sun, W.; Fan, X.; Lin, J.; Ren, M.; Yang, L.; Zhang, C. Mechanisms driving phosphorus release during algal blooms based on hourly changes in iron and phosphorus concentrations in sediments. *Water Res.* **2018**, *133*, 153–164.

(11) Kumar, P. S.; Korving, L.; Van Loosdrecht, M. C. M.; Witkamp, G.-J. Adsorption as a technology to achieve ultra-low concentrations of phosphate: Research gaps and economic analysis. *Water Res. X* **2019**, *4*, 100029.

(12) de-Bashan, L. E.; Bashan, Y. Recent advances in removing phosphorus from wastewater

and its future use as fertilizer (1997–2003) *Water Res.* **2004**, *38* (19), 4222–4246.

(13) Mañas, A.; Biscans, B.; Spérandio, M. Biologically induced phosphorus precipitation in aerobic granular sludge process. *Water Res.* **2011**, *45* (12), 3776–3786.

(14) Noyma, N. P.; De Magalhães, L.; Furtado, L. L.; Mucci, M.; Van Oosterhout, F.; Huszar, V. L. M.; Marinho, M. M.; Lürling, M. Controlling cyanobacterial blooms through effective flocculation and sedimentation with combined use of flocculants and phosphorus adsorbing natural soil and modified clay. *Water Res.* **2016**, 97, 26–38.

(15) Luo, D.; Wang, L.; Nan, H.; Cao, Y.; Wang, H.; Kumar, T. V.; Wang, C. Phosphorus adsorption by functionalized biochar: a review. *Environ. Chem. Lett.* **2023**, *21* (1), 497–524.

(16) Abegunde, S. M.; Idowu, K. S.; Adejuwon, O. M.; Adeyemi-Adejolu, T. A review on the influence of chemical modification on the performance of adsorbents. *Resour. Environ. Sust.* **2020**, *1*, 100001.

(17) Li, L.; Zhu, Z.; Shi, J.; Li, Z.; Zuo, X. Simultaneous phosphorus removal and adsorbents recovery with Ca-PAC assisted adsorption dynamic membrane system: Removal performance and influencing factors. *J. Clean. Prod.* **2023**, *384*, 135591.

(18) Xia, W.-J.; Guo, L.-X.; Yu, L.-Q.; Zhang, Q.; Xiong, J.-R.; Zhu, X.-Y.; Wang, X.-C.; Huang, B.-C.; Jin, R.-C. Phosphorus removal from diluted wastewaters using a La/C nanocomposite-doped membrane with adsorption-filtration dual functions. *Chem. Eng. J.* **2021**, *405*, 126924.

(19) Johir, M. A. H.; Nguyen, T. T.; Mahatheva, K.; Pradhan, M.; Ngo, H. H.; Guo, W.; Vigneswaran, S. Removal of phosphorus by a high rate membrane adsorption hybrid system. *Bioresour. Technol.* **2016**, *201*, 365–369.

(20) Wang, B.; Ma, Y.; Lee, X.; Wu, P.; Liu, F.; Zhang, X.; Li, L.; Chen, M. Environmental-friendly coal gangue-biochar composites reclaiming phosphate from water as a slow-release fertilizer. *Sci. Total Environ.* **2021**, *758*, 143664.

(21) Deng, Y.; Li, M.; Zhang, Z.; Liu, Q.; Jiang, K.; Tian, J.; Zhang, Y.; Ni, F. Comparative study on characteristics and mechanism of phosphate adsorption on Mg/Al modified biochar. *J. Environ. Chem. Eng.* **2021**, *9* (2), 105079.

(22) Rott, E.; Nouri, M.; Meyer, C.; Minke, R.; Schneider, M.; Mandel, K.; Drenkova-Tuhtan,

A. Removal of phosphonates from synthetic and industrial wastewater with reusable magnetic adsorbent particles. *Water Res.* **2018**, *145*, 608–617.

(23) Yang, H.; Zhang, H.; Lu, J.; Cui, Y.; Wang, Y.; Wang, X.; Xue, J.; Cao, H. Advanced magnetic adsorbents for enhanced phosphorus and fluoride removal from wastewater: Mechanistic insights and applications. *Sep. Purif. Technol.* **2025**, *353*, 128195.

(24) Gao, D.; Ji, H.; Li, R.; Tajammal Munir, M.; Wu, X.; Huang, Y.; Li, B. Advancing sustainable phosphorus removal and recovery with Metal-Organic frameworks (MOFs). *Chem. Eng. J.* **2023**, *475*, 145949.

(25) Bouanga Boudiombo, J. S.; Madden, D. G.; Cusack, B.; Cronin, P.; Ryan, A. State of the art and prospects of zeolites and metal organic frameworks (MOFs) for nitrogen and phosphorus removal in dairy wastewater. *Chemosphere* **2023**, *329*, 138531.

(26) Yang, C.-H.; Chang, J.-S.; Lee, D.-J. Covalent organic framework EB-COF:Br as adsorbent for phosphorus (V) or arsenic (V) removal from nearly neutral waters. *Chemosphere* **2020**, *253*, 126736.

(27) Du, M.; Zhang, Y.; Wang, Z.; Lv, M.; Tang, A.; Yu, Y.; Qu, X.; Chen, Z.; Wen, Q.; Li, A. Insight into the synthesis and adsorption mechanism of adsorbents for efficient phosphate removal: Exploration from synthesis to modification. *Chem. Eng. J.* **2022**, *442*, 136147.

(28) Bacelo, H.; Pintor, A. M. A.; Santos, S. C. R.; Boaventura, R. A. R.; Botelho, C. M. S. Performance and prospects of different adsorbents for phosphorus uptake and recovery from water. *Chem. Eng. J.* **2020**, *381*, 122566.

(29) Xin, Y.; Xiong, Q.; Bai, Q.; Miyamoto, M.; Li, C.; Shen, Y.; Uyama, H. A hierarchically porous cellulose monolith: A template-free fabricated, morphology-tunable, and easily functionalizable platform. *Carbohydr. Polym.* **2017**, *157*, 429–437.

(30) Zhang, L.; Wang, Y.; Pan, L.; Tang, R.; Asoh, T.-A.; Ou, J.; Uyama, H. Fabrication of a reusable bifunctional biomimetic Ti4+-phosphorylated cellulose monolith with a coral-like structure for enrichment of phosphorylated and glycosylated peptides. *Green Chem.* **2021**, *23* (19), 7674–7684.

(31) Kanno, T.; Uyama, H. Unique leafy morphology of poly(lactic acid) monoliths controlled via novel phase separation technology. *RSC Adv.* **2017**, *7* (54), 33726–33732.

(32) Wang, G.; Zhang, L.; Sugawara, A. Hsu, Y.-I.; Asoh, T.-A.; Uyama, H. Development of

Citric-Acid-Modified Cellulose Monolith for Enriching Glycopeptides. *Anal. Chem.* **2025**, *97* (2), 1125–1134.

(33) Svec, F.; Fréchet, J. M. J. New Designs of Macroporous Polymers and Supports: From Separation to Biocatalysis. *Science* **1996**, *273* (5272), 205–211.

(34) Béguin, P.; Aubert, J.-P. The biological degradation of cellulose. *FEMS Microbiol. Rev.* **1994**, *13* (1), 25–58.

(35) Haider, A. J.; Jameel, Z. N.; Al-Hussaini, I. H. M. Review on: Titanium Dioxide Applications. *Energy Procedia* **2019**, *157*, 17–29.

(36) Connor, P. A.; McQuillan, A. J. Phosphate Adsorption onto TiO_2 from Aqueous Solutions: An in Situ Internal Reflection Infrared Spectroscopic Study. *Langmuir* **1999**, *15* (8), 2916–2921.

(37) Kang, S. A.; Li, W.; Lee, H. E.; Phillips, B. L.; Lee, Y. J. Phosphate uptake by TiO_2: Batch studies and NMR spectroscopic evidence for multisite adsorption. *J. Colloid Interface Sci.* **2011**, *364* (2), 455–461.

(38) Ronson, T. K.; McQuillan, A. J. Infrared Spectroscopic Study of Calcium and Phosphate Ion Coadsorption and of Brushite Crystallization on TiO_2. *Langmuir* **2002**, *18* (12), 5019–5022.

(39) Wolf, S.; Sriram, K.; Camassa, L. M. A.; Pathak, D.; Bing, H. L.; Mohr, B.; Zienolddiny-Narui, S.; Samulin Erdem, J. Systematic review of mechanistic evidence for TiO2 nanoparticle-induced lung carcinogenicity. *Nanotoxicology* **2024**, *18* (5), 437–463.

(40) Lyu, Y.; Asoh, T.-A.; Uyama, H. Hierarchically porous TiO_2 monolith prepared using a cellulose monolith as a template. *Mater. Chem. Front.* **2021**, *5* (10), 3877–3885.

(41) Tsang, S.; Phu, F.; Baum, M. M.; Poskrebyshev, G. A. Determination of phosphate/arsenate by a modified molybdenum blue method and reduction of arsenate by $S_2O_4^{2-}$. *Talanta* **2007**, *71* (4), 1560–1568.

(42) Worsfold, P.; McKelvie, I.; Monbet, P. Determination of phosphorus in natural waters: A historical review. *Anal. Chim. Acta* **2016**, *918*, 8–20.

(43) Ibnul, N. K.; Tripp, C. P. A simple solution to the problem of selective detection of phosphate and arsenate by the molybdenum blue method. *Talanta* **2022**, *238*, 123043.

(44) Bérard, R.; Sassoye, C.; Terrisse, H.; Bertoncini, P.; Humbert, B.; Cassaignon, S.; Le Caër,

S. Effect of Crystalline Phase and Facet Nature on the Adsorption of Phosphate Species onto TiO_2 Nanoparticles. *Langmuir* **2024**, *40* (31), 16258–16271.

(45) Tielens, F.; Gervais, C.; Deroy, G.; Jaber, M.; Stievano, L.; Coelho Diogo, C.; Lambert, J.-F. Characterization of Phosphate Species on Hydrated Anatase TiO_2 Surfaces. *Langmuir* **2016**, *32* (4), 997–1008.

(46) Gong, W. A. A real time in situ ATR-FTIR spectroscopic study of linear phosphate adsorption on titania surfaces. *Int. J. Miner. Process.* **2001**, *63* (3), 147–165.

(47) Elzinga, E. J.; Sparks, D. L. Phosphate adsorption onto hematite: An in situ ATR-FTIR investigation of the effects of pH and loading level on the mode of phosphate surface complexation. *J. Colloid Interface Sci.* **2007**, *308* (1), 53–70.

(48) Fernández-Ibáñez, P.; De Las Nieves, F. J.; Malato, S. Titanium Dioxide/Electrolyte Solution Interface: Electron Transfer Phenomena. *J. Colloid Interface Sci.* **2000**, *227* (2), 510–516.

(49) Dutta, P. K.; Ray, A. K.; Sharma, V. K.; Millero, F. J. Adsorption of arsenate and arsenite on titanium dioxide suspensions. *J. Colloid Interface Sci.* **2004**, *278* (2), 270–275.

(50) Cui, Q.; Xu, J.; Wang, W.; Tan, L.; Cui, Y.; Wang, T.; Li, G.; She, D.; Zheng, J. Phosphorus recovery by core-shell γ-Al_2O_3/Fe_3O_4 biochar composite from aqueous phosphate solutions. *Sci. Total Environ.* **2020**, *729*, 138892.

(51) Kumar, E.; Bhatnagar, A.; Kumar, U.; Sillanpää, M. Defluoridation from aqueous solutions by nano-alumina: Characterization and sorption studies. *J. Hazard. Mater.* **2011**, *186* (2–3), 1042–1049.

(52) Hu, C. Y.; Lo, S. L.; Kuan, W. H. Effects of the molar ratio of hydroxide and fluoride to Al(III) on fluoride removal by coagulation and electrocoagulation. *J. Colloid Interface Sci.* **2005**, *283* (2), 472–476.

(53) Hadjiivanov, K.; Klissurski, D. G.; Davydov. A. A. Study of phosphate-modified TiO_2 (anatase). *J. Catal.* **1989**, *116* (2), 498–505.

(54) Cao, S.; Zhang, X.; Xie, S.; Wang, C.; Bai, J.; Li, X.; Zhang, R.; Xiao, X.; Hu, J.; Jiang, X. Mechanistic insights into efficient phosphorus adsorption and recovery from water using functional ZnO/ZnFe-LDHs alginate hydrogels. *J. Environ. Chem. Eng.* **2025**, *13*, 115091.

(55) Yan, J.; Zhou, X.; Zhang, W.; Cheng, F.; Wang, H.; Cui L.; Quan, G. Binding mechanisms and phosphorus adsorption performance of soil mineral-BDOM complexes. *J. Water Process Eng.* **2025**, *69*, 106747.

(56) Zeng, H.; Sun, S.; Xu, K.; Zhao, W.; Hao, R.; Zhang J.; Li, D. Iron-loaded magnetic alginate-chitosan double-gel interpenetrated porous beads for phosphate removal from water: Preparation, adsorption behavior and pH stability. *React. Funct. Polym.* **2022**, *177*, 105328.

(57) Pan, F.; Wei, H.; Huang, Y.; Song, J.; Gao, M.; Zhang, Z.; Teng R.; Jing, S. Phosphorus adsorption by calcium chloride-modified buckwheat hulls biochar and the potential application as a fertilizer. *J. Clean. Prod.* **2024**, *444*, 141233.

(58) Wang, C.; Li, R.; Xu, Y.; Ma, Z.; Qiu, Y.; Wang, C.; Ren L.-F.; Shao, J. Effective electrosorption and recovery of phosphorus by capacitive deionization with a covalent organic framework-membrane coating electrode. *Desalination* **2024**, *570*, 117088.

(59) Liu, Y.; Wang, S.; Huo, J.; Zhang, X.; Wen, H.; Zhang, D.; Zhao, Y.; Kang, D.; Guo W.; Ngo, H. H. Adsorption recovery of phosphorus in contaminated water by calcium modified biochar derived from spent coffee grounds. *Sci. Total Environ.* **2024**, *909*, 168426.

(60) Zhang, X.; Xiong, Y.; Wang, X.; Wen, Z.; Xu, X.; Cui, J.; Liu, Z.; Wei L.; An, X. MgO-modified biochar by modifying hydroxyl and amino groups for selective phosphate removal: Insight into phosphate selectivity adsorption mechanism through experimental and theoretical. *Sci. Total Environ.* **2024**, *918*, 170571.

(61) Yi, Y.; Fu, Y.; Wang, Y.; Xu Z.; Diao, Z. Lanthanum/iron co-modified biochar for highly efficient adsorption of low-concentration phosphate from aqueous solution. *J. Environ. Chem. Eng.* **2024**, *12*, 111876.

(62) Ding S.; Wang, X. Terbium-based metal organic framework and its immobilized nanofibrous membrane for selective detection and efficient removal of phosphate. *Chem. Eng. J.* **2023**, *464*, 142751.

(63) Zhai, Y.; Li, Y.; Hou, Q.; Zhang, Y.; Zhou, E.; Li H.; Ai, S. Highly sensitive colorimetric detection and effective adsorption of phosphate based on MOF-808(Zr/Ce). *New J. Chem.* **2022**, *46*, 15405–15413.

Concluding Remarks

In this thesis, cellulose-based monoliths were designed for the adsorption and separation of biologically relevant molecules. Through modifying citric acid, surface imprinting layer and TiO_2 on the surface of CM, these materials have good application potential in enrichment of glycopeptides, shikimic acid and phosphate adsorption.

In chapter 1, CCM was prepared through the simple surface functionalization with citric acid to promote the development of porous materials suitable for use as a HILIC stationary phase. The CCM featured a distinctive coral-like skeletal structure with continuous pores and a rough surface, facilitated high permeability of the mobile phase, and promoted efficient mass transfer. This work provides a simple, eco-friendly, and effective method for glycopeptide enrichment, and successfully achieved the selective purification and concentration of glycopeptides even under complex sample conditions, which is pivotal for advancing protein glycosylation research.

In chapter 2, MIPs-CM was developed as an effective adsorption material for selective SA separation. By constructing a SA-specific imprinted adsorption layer through the use of boronic acid monomers and a molecular imprinting technique, the monolith exhibited significantly enhanced selectivity toward SA. This study provides valuable insights into the development of highly selective and reusable imprinted monoliths, offering a promising approach for the efficient capture of natural SA and other drug molecules in practical applications.

In chapter 3, TiO_2-CM was fabricated and applied for phosphate ion removal. Incorporating TiO_2 into the CM significantly enhanced its specific surface area owing to its well-developed hierarchically porous morphology. The TiO_2-CM displayed excellent phosphate sequestration efficiency under continuous flow conditions. These findings highlight the promising potential of the TiO_2-CM for phosphate removal in applications such as environmental pollution control and industrial wastewater treatment.

In summary, this study demonstrates a versatile and sustainable strategy for tailoring cellulose-based monoliths through surface functionalization and structural engineering to meet diverse adsorption and separation needs. By integrating citric acid functional groups, molecularly imprinted layers, and TiO_2 nanoparticles, each monolith exhibits a distinct surface chemistry and hierarchical porosity, enabling high specificity, selectivity, and adsorption efficiency for target molecules. These results underscore the potential of cellulose monoliths as customizable platforms for bioanalytical, pharmaceutical, and environmental applications. Future research may further explore the tunability of these systems for broader analyte ranges and their scalability in industrial processes.

List of Publications

1. Development of Citric-Acid-Modified Cellulose Monolith for Enriching Glycopeptides

Guan Wang, Luwei Zhang*, Akihide Sugawara*, Yu-I Hsu, Taka-Aki Asoh, and Hiroshi Uyama*

Analytical Chemistry, **2025**, *97* (2), 1125–1134.

DOI: 10.1021/acs.analchem.4c03857

2. Development of Molecularly Imprinted Cellulose Monoliths for the Selective Separation of Shikimic Acid in Continuous Flow Systems

Guan Wang, Akihide Sugawara*, and Hiroshi Uyama*

ACS Applied Polymer Materials, **2025**, 7, 9098−9108.

DOI: 10.1021/acsapm.5c01354

3. Hierarchically Porous Titanium Dioxide-Cellulose Monolith for Removal of Phosphate Ions from Water

Guan Wang, Akihide Sugawara*, and Hiroshi Uyama*

Bulletin of the Chemical Society of Japan, **2025**, 98, 8.

DOI: 10.1093/bulcsj/uoaf068

Acknowledgments

Firstly, I would like to express my sincere gratitude to my advisor Prof. Hiroshi Uyama for the continuous support of my Ph.D. study, for his patience, motivation, and immense knowledge. His guidance helped me in all the time of research and writing of this thesis.

Besides my advisor, I would like to thank the rest of my thesis committee: Prof. Takahiro Kozawa and Prof. Hidehiro Sakurai, for their insightful comments and their donation of time.

I am profoundly grateful to Asst. Prof. Akihide Sugawara, for his suggestions and inspirations to improve the quality of my research. I also thank him for his efforts in knowledge sharing and manuscripts revising. Without his help, this thesis would not be possible.

My sincere thanks also go to Assoc. Prof. Yu-I Hsu and Dr. Luwei Zhang for their kind help and expert advice.

I would like to thank all staff of Uyama Laboratory, especially, Ms. Yoko Uenishi and Ms. Tomoko Shimizu. I want to thank the lovely and kind members in Uyama Lab: Dr. Yanting Lyu, Dr. Luwei Zhang, Dr. Yan Wang, Dr. Manjie He, Dr. Yuxiang Jia, Dr. Juan Wang, Dr. Peng Du, Ms. Zeying Cao, Ms. Linxuan Li, Ms. Xunran Guo, Ms. Alice, Ms. Ying Yao, Mr. Takeshi Hiraoka, Mr. Yuki Shioji, Dr. Nontarin Roopsung, Dr. Emil Hajili, Dr. Madhurangika Panchabashini Horathal Pedige, Ms. May Myat Noe, Ms. Hasinah Binti Mohamed Rafiq, Ms. Judit Rebeka Molnar, Mr. Ruiqi Zhang, Mr. Yihan Gao, Ms. Izzah Durrati Binti Haji Abdul Hamid, Ms. Sooyeon Noh, Mr. Jiahui Dong, Mr. Yazhou Su, Mr. Kai Cheng, Mrs. Qianying Li, Mr. Yihe Chen, Ms. Shafinee Yarnina Hj Md Shafri, Ms. Ziyu Meng, Mr. Zhengqi Liu, Ms. Masako Tatsuta, Ms. Bravo Da Costa Daniela Yacine Sebastião, Mr. Konosuke Yoshida, Ms. Siaw Thong Chua, Ms. Peixuan Shao, Mr. Chenxu Zhang, Mr. Naoaki Ishihara, Mr. Yuta Okuda, Ms. Kanako Sakai, Mr. Daiki Morimoto, Ms. Supritha Muppuri, Ms. Yoshiki Imazato, Mr. Naoki Ueda, Mr. Tomoya Ushiroda, Mr. Yuto Kirihata, Ms. Akiko Mano, Ms. Thuy Le Huynh An, Mr. Motoi Oda, Ms. Suzune Miki, Mr. Kaita Kikuchi, Mr. Koki Tsujita, Mr. Hajime Fujimori, Ms. Rika Onishi, Mr. Shotaro Yano, Ms. Rina Kugimiya, Ms. Kyoko Tanimura, Ms. Chikabo Abe, Ms. Erina Katsuragawa, Mr. Yasushi Takeuchi, and Mr. Atsuki Takagi, etc. for their kind hearted help in my lab and daily life.

Last but not the least, I would like to thank my parents for supporting me spiritually throughout writing this thesis. This thesis would not have been possible without their help, love, dedication, and encouragement.

June 2025

Wang Guan